UNIVERSITY OF CALABRIA

DOCTORAL THESIS

Across Scales Approach Based on Exciton-Plasmon Coupling for Low Loss Optical Metamaterials

Author:
RAKESH DHAMA

Supervisor:
Prof. Antonio De Luca

A thesis submitted in fulfilment of the requirements for the degree of Doctor of Philosophy in

Molecular Materials and Mesophases

Department of Physics

November 2015

Acknowledgements

First of all, I would like to express my sincerest gratitude to my supervisor Professor Antonio De Luca for his valuable guidance and friendly attitude during this PhD program. I felt so fortunate to work with him as he has always time for scientific discussions and open for new ideas. His experimental skills and hardworking spirit continuously motivated me. I am also thankful to him to review this thesis.

I am also very grateful to Professor Giuseppe Strangi to offer me this research opportunity here in Unical and also to invite me in Case Western Reserve university (USA). I always admire his scientific approach as well as his humble nature and follow his guidance as he is mentor to everyone in the group.

I must thank to Prof. Roberto Bartolino, Prof. Carlo Versace and Dr. Michele Giocondo for their helps. I also would like to thank my friends Vincenzo Caligiuri, Alireza, Luigia, Giovanna and my Indian friends Hari, Krishna and Dhanya who always helped me, when I was in need.

I would extend my thanks to my very old friends Vivek, Vinay, Harendra, Amit, Subodh, Chetan, Nirikshan and Sachin to be in touch with me, even I am too far. I am sorry if I miss someone, but hope not.

I am also thankful to my sisters Rekha, Ritu, Garima and my brother Gaurav for their everlasting love and support. Thank you to my wife Neha to make my life so beautiful and to bear my temper sometimes. I must say thanks to her parents for such a beautiful gift to me

I am always in debt to my PARENTS and my Mamaji and Mamiji for their efforts for my bright future. It was the biggest dream of my mother's life to elevate me as an educated person. I hope that I always made her proud.

Contents

List of Figures

List of Tables

Dedicated to my Nanaji Late. Ch. Brahm Singh
I wish you were with us today

Chapter 1

Introduction

1.1 Motivation

Strong absorptive losses affect the performance of all plasmonic devices and metamaterials in the optical range, making impossible to harness most of their fascinating properties for real life applications. It is mandatory to mitigate such losses in order to achieve further novel applications and extra ordinary electromagnetic properties. Several ways have been proposed in order to achieve low loss plasmonic devices. Electromagnetic induced transparency (EIT) and replacement of gold and silver by comparative less absorptive materials as Titanium Nitride (TiN) can also represent the two ways to tackle these losses. Furthermore, both the methods have their own limitations. EIT removes the effect of medium in a narrow wavelength range and offers very selective loss mitigation, while TiN can not compete with gold, if compared on applications basis. Incorporation of gain at the heart of plasmonic entities is still considered as the best available strategy to encounter optical losses. Bringing gain media in the close proximity of plasmonic structures triggers non-radiative energy transfer processes from active materials to plasmonic NPs, enabling strong exciton-plasmon coupling and mitigating the optical losses.

This thesis is aimed to study the mitigation of absorptive losses in gain incorporated plasmonic systems from nanoscale to macroscale level. Starting from the simple gain-plasmon systems such as gain functionalized nanostructures dispersed in ethanol, successful results were also obtained in the meso- and macroscaled plasmonic systems.

1.2 Outline of thesis

Below, you will find a short description of all the chapters that compose this Thesis.

Chapter 2 discusses the field of plasmonics and its development towards novel applications. Chapter provides literature studies of metal optical response and describes the significance of metal nanoparticles over bulk metals. Chapter continues with discussions on localized surface plasmon resonances (LSPR), its theoretical description and also on experimental parameters affecting plasmon band of nanoparticles (NPs). Last section of the chapter is devoted to theoretical background of surface plasmon polaritons (SPPs) and its coupling at metal-dielectric interfaces.

Chapter 3 is completely dedicated to metamaterials. It begins with basic introduction to metamaterials and an approach towards the realization of metastructures. Then, it describes optical metamaterials and concerns over absorptive losses due to low value of figure of merit. Chapter moves forward with discussions on gain induced optical metamaterials and fabrication methods by top down approach. It further proposes a strategy to envisage self assembled metamaterials, using plasmonic nanostructures as subunits. Chapter completes with fundamentals of hyperbolic metamaterials (HMMs) such as its classification, suitable materials for HMMs and origin of high k modes.

Chapter 4 presents the optical properties of gain materials and energy transfer processes, starting from the excitation of fluorophores and all the possible occurred phenomenon. Then, chapter describes Förster radiative energy transfer process (FRET) among two gain molecules occurring via exciton-exciton coupling and further explains Gain–Plasmon resonant energy transfer (GPRET), when a gain molecule is replaced with plasmonic NPs in order to understand gain-plasmon coupling mechanism. Thus, chapter proposes a strategy to mitigate these losses by incorporating gain media in the close proximity of plasmonic NPs, which enables non-radiative energy transfer processes from gain molecules to plasmonic NPs via gain-plasmon coupling.

Chapter 5 describes the results on gain functionalized plasmonic core–shell nanostructures disperesed in ethanol, where gain molecules are embedded in silica shells and interlocked by silica spacers, prepared by our French collaborators, in order to investigate the role played by the inter-distance between the two species. Such single core-shell nanostructures are considered as monomers, while the grouping of monomers represent multimers. Emission quenching by means of steady-state fluorescence spectroscopy combined with significant shortening of the corresponding fluorescence lifetime using TCSPC data and simultaneous enhancement of Rayleigh scattering and transmittance reveal more effective absorptive loss mitigation for multimeric systems.

Chapter 6 explores the effects of exciton-plasmon coupling in two mesoscaled plasmonic systems which are dispersed in ethanol, such as dye doped plasmonic nanoshells and gain assisted plasmonic mesocapsules. Plasmonic nanoshells, synthesized by our French chemistry collaborators, which are consisted of RhB dye doped silica core coated by a thin gold layer in order to investigate the exciton-plasmon coupling between chromophores and metallic shells. Performed experiments confirm strong gain-plasmon coupling and demonstrate transmittance enhancement as a function of gain in a wide range of optical wavelengths (about 100 nm) and an increase of the absorption cross section in the nearby spectral region showing the super-absorbing features in the specific wavelength range.

On the other hand, mesoporous silica capsules embedding gold nanoparticles, prepared by our Spanish chemistry collaborators, show a broad plasmon resonance band covering a large portion of the visible spectrum (500-700 nm). Gain-plasmon interplay is dominated by the location of the gain medium with respect to the spatial distribution of the local field. Several decisive experiments such as fluorescence quenching, decay time data and enhanced transmitted pump probe beam as a function of pump energy along with simulation support, demonstrate a substantial gain induced broadband loss mitigation.

Chapter 7 deals with three macroscaled plasmonic systems. The first section reports on exciton-plasmon coupling in nanocomposite polymeric films embedding core-shell quantum dots (CdSe@ZnS QDs) and gold nanoparticles (Au-NPs). We conceived such hybrid composite films in order to investigate the energy transfer process between excitons and plasmons in a bulk matrix, which were realized by our chemistry collaborators. Stable and freestanding films are obtained by simultaneous dispersion of both entities in a polymer matrix owing to modification of QDs surface chemistry.

Second section of chapter describes the near-field study of thue Morse patterned plasmonic nanocavities which are fabricated by Naples collaborators using electron beam lithography and evaporation of a 60 nm gold layer on designed structures.

Third last section of chapter discusses the experimental realization of metal-dielectric multilayered hyperbolic metamaterials, presenting an inversion point of coexisting anisotropies in the visible range. In this work, my contribution was the extraction of optical parameters by means of spectroscopic ellipsometry measurements.

It is worth to note that, in both last sections, gain materials are not yet included. The preliminary understanding of the macroscopic optical properties represents a key factor for the study of the possible exciton-plasmon coupling in such systems.we intended to incorporate gain in such particular structures in future.

Chapter 2

Overview on Plasmonics

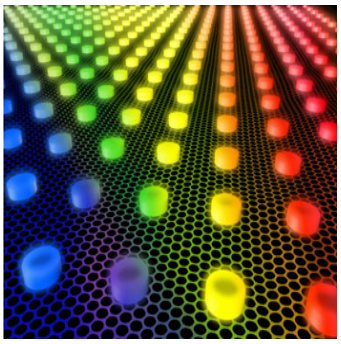

2.1 Plasmonics : From Lycurgus Cup to Optical Metamaterials

In 1959, Richard Feynman delivered his famous lecture entitled 'Plenty of Room at the Bottom' envisaging about the possibilities of fascinating properties at miniature scale which can not be observed at the macroscale. After the two decades, this new research field was named as *Nanotechnology*. There are several examples in the history when plasmonics was exploited for the coloration of glass, ceramics and as decorative pigments without any knowledge of real origin behind these surprising optical effects [1]. In $1000-1200$ BC, use of metal crystal by Romans to produce various colors is considered as the oldest example.

The famous Lycurgus cup (4^{th} century AD) still can be seen as an evident example at British Museum showing the unique feature of changing color depending upon the incident light in which it is seen. The cup looks green when it is viewed in reflected light,

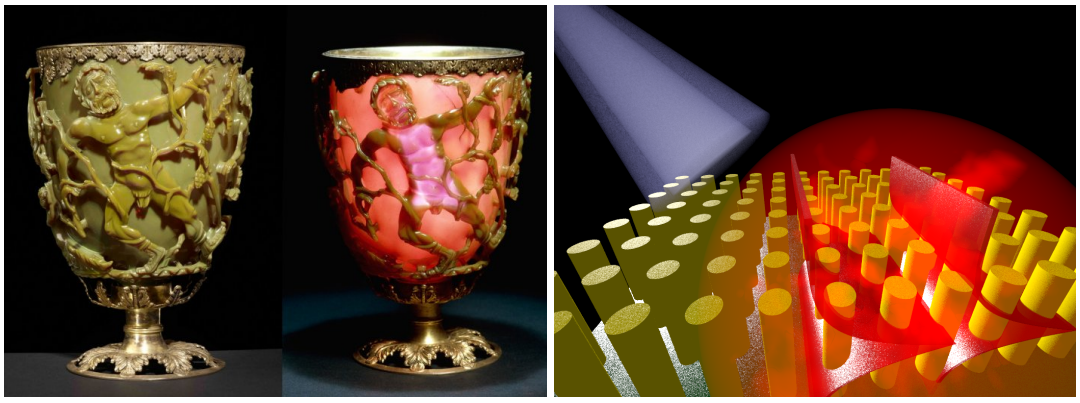

FIGURE 2.1: Here, the two examples demonstrate the development in the field of plasmonics. (a) The Lycurgus cup, the specimen of Roman Nanotechnology looks green in the reflected light and red in the transmitted light [2]. (b) Hyperbolic nanorods metamaterial designed in 2015, is applicable in biosensors and nanophotonic devices [3].

but turns out red color when the light is incident from inside and viewed in the transmitted light [2]. Change in color is attributed to the mixture of tiny gold and silver metal crystal in an approximate molar ratio of 14 : 1. Unfortunately, the further progress was limited due to lack of metallic synthesis methods. However, significant development in the fabrication and novel manipulation methods of nanometer-sized objects in the last decades allowed us to enter into the fascinating world at the length scale of molecules. Plasmonics enables various interdisciplinary applications such as biosensing [4], ability to make the things invisible named as cloaking [5], inventing novel methods for cancer treatment and predictions of superfast computer chips [6] and the realization of metamaterials in the visible range [7].

The secret of all these amazing optical properties is the ability to confine light on subwavelength scale. Plasmonics makes a connection between two different length scales. The empire of plasmonics is at the basis of metallic nanostructures and thin metal films. Under the irradiation of light, nanostructures confine the light enhancing absorption while the electron density waves propagate along the interface of a metal films and a dielectric like the ripples that spread across a water surface after throwing a stone into the water [6].

2.2 Optical response of metals

The optical properties of noble metals are assumed to be determined mainly by two aspects: (i) the conduction electrons can move freely within the bulk of material (ii) the

inter-band excitations can take place if the energy of the incoming photons exceeds the band gap energy of the respective metal. In the early of 20^{th} century a German physicist, called Paul Drude, devised a very simple model to understand the response of metallic particles. Drude successfully applied the kinetic theory of gases to explain the electrical and optical properties of metals with three assumptions [8] :
(1) Interactions of an electron with another electrons and with ions are neglected between collisions.
(2) Electron-electron scattering is neglected.
(3) Electrons experience a collision probability per unit time of $1/\tau$, where τ is the interval time between two adjacent collisions.
Drude model considers the motion of a whole electron cloud as the summation of the motion of the individual electrons. All the free electrons in a metal oscillate in coherent phase under a time dependent electrical field, exhibiting bulk plasmon resonance [9]. Maxwell's equations represent the interaction of an electromagnetic wave with metal and show a relation between the electric field **E**, the electric polarization **P** to the electric displacement **D**, magnetization **M**, the magnetic field **H** to magnetic induction **B**;

$$\mathbf{D} = \varepsilon_0 \mathbf{E} + \mathbf{P} = \varepsilon_0 \varepsilon_\infty \mathbf{E} \tag{2.1}$$

$$\mathbf{B} = \mu_0 (\mathbf{H} + \mathbf{M}) \tag{2.2}$$

Where ε_0, μ_0 and ε_∞ are the permittivity of free space, vacuum permeability and dielectric constant of the bulk medium.

On the application of Drude model for the free-electron gas, the displacement **x** of an electron in the presence of an electric field and the macroscopic polarization **P** can be obtained by solving the motion equation of the electrons under the influence of an external field

$$m\frac{\partial^2 x}{\partial t^2} + m\gamma\frac{\partial x}{\partial t} = -eE_0 e^{-i\omega t} \tag{2.3}$$

The second term of left hand side of above differential equation is a viscous friction due to various factors such as free electron inelastic collisions, electron phonon coupling, defects and impurities. γ is the corresponding collision frequency which is also the bulk metal damping constant. The right hand side of the motion equation is the force due to the electric field. Time dependent electric field has the plane wave form $\mathbf{E}(t) = \mathbf{E}_0 e^{-i\omega t}$. A solution of above differential equation is given by $\mathbf{x}(t) = \mathbf{x}_0 e^{-i\omega t}$. Permittivity as the function of frequency $\varepsilon(\omega)$ can be calculated, initiating from expression of time dependent electrons displacement, which is obtained from equation 1.3.

$$\mathbf{x}(t) = \frac{e}{m(\omega^2 + i\gamma\omega)}\mathbf{E}(t). \tag{2.4}$$

Since the electric displacement **D** and the macroscopic polarization **P** are given by:

$$\mathbf{D} = \varepsilon_0\mathbf{E} + \mathbf{P} = \varepsilon_0\varepsilon\mathbf{E} \tag{2.5}$$

$$\mathbf{P} = -Ne\mathbf{x} \tag{2.6}$$

N refers to the number of electrons per unit volume. Thus,

$$\mathbf{D} = \varepsilon_0\mathbf{E} - \frac{Ne^2}{m(\omega^2 + i\gamma\omega)}\mathbf{E} \tag{2.7}$$

and

$$\varepsilon(\omega) = 1 - \frac{\omega_p^2}{\omega^2 + i\gamma\omega} \tag{2.8}$$

The above relation represents the dielectric function in the Drude model, where ω_p is the plasma frequency of the free electron gas, defined as:

$$\omega_p = \left(\frac{Ne^2}{\varepsilon_0 m}\right)^{1/2} \tag{2.9}$$

Separating real and imaginary parts, equation (1.8) can be simplified such as $\varepsilon(\omega) = \varepsilon_1(\omega) + i\varepsilon_2(\omega)$ are given by:

$$\varepsilon_1(\omega) = 1 - \frac{\omega_p^2\tau^2}{1 + \omega^2\tau^2} \tag{2.10}$$

$$\varepsilon_2(\omega) = \frac{\omega_p^2\tau}{\omega(1 + \omega^2\tau^2)} \tag{2.11}$$

The real component ($\varepsilon_1(\omega)$) describes group velocity dispersion, while imaginary part ($\varepsilon_2(\omega)$) shows the dissipation of electrons energy in metal. Drude model partially satisfies the experimental data for optical constants of noble metals obtained by Johnson and Christy using reflection and transmission measurements [10]. Experimental model of optical constants of noble metals (copper, silver and gold) obtained by P. B. Johnson and R. W. Christy through reflection and transmission measurements is an acceptable reference for evaluating the accuracy of Drude model. In Figure 1.2, the real and the imaginary parts of dielectric function of gold simulated by Drude model are compared with Johnson Chrisity data.

Figure 2.2(a) clearly shows that Drude model agrees with experimental data along with

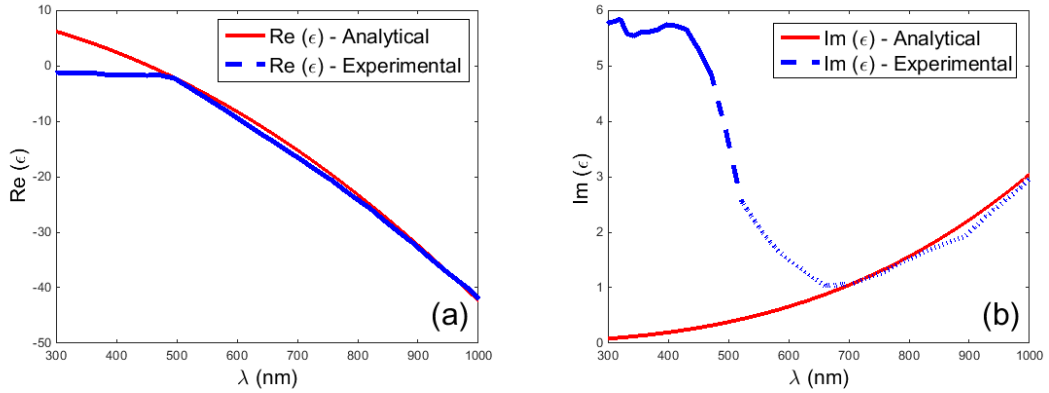

FIGURE 2.2: (a) Real and (b) imaginary components of the dielectric constant for gold calculated by Drude free electron model (red line) and Johnson & Christy experimental data (blue solid line).

the negative real part of permitivity of gold in wavelength higher than 450nm, but does not follow the experimental imaginary part in visible range as shown in figure 2.2(b). Deviation of Drude model from experimental data causes due to the exclusion of the effect of bound electrons as this model is based on existence of only free electrons in the metal.

2.2.1 Bound electrons contribution to Drude model in metal nanostructures

Drude model deviation from experimental data can be improved by considering bound electrons in the metals. The induced dipolar charge separation imposes force on the electron cloud. The electrons undergo a restoring force in the opposite direction to the external electric field. Such system is considered equivalent to classical mechanical oscillators, the position **x** of an electron placed in the oscillating cloud of a nanoparticles is then governed by following equation, where K is the spring constant of the potential that keeps the electron in place and symbolizes the damping constant describing mainly radiative damping in the case of bound electrons with effective mass m [11].

$$m\frac{\partial^2 x}{\partial t^2} + m\gamma\frac{\partial x}{\partial t} + Kx = -eE_0 e^{-i\omega t} \tag{2.12}$$

The above equation shows the movement of a forced and damped harmonic oscillator. The contribution of bound electrons to the dielectric function can be written in a

standard Lorentz form as

$$\varepsilon_b(\omega) = 1 + \frac{\omega_p^2}{\omega_0^2 - \omega^2 - i\gamma\omega} \tag{2.13}$$

Where ω_p and ω_0 stand for the plasma frequency in Drude model and oscillation frequency of bound electrons under applied electric potential, respectively [9]. The conclusive dielectric constant, considering free electrons as well as bound electrons can be expressed such as

$$\varepsilon(\omega) = \varepsilon_b(\omega) + \varepsilon_\infty - \frac{\omega_p^2}{\omega^2 + i\gamma\omega} \tag{2.14}$$

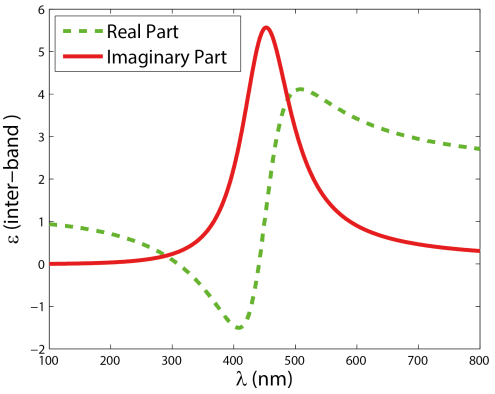

FIGURE 2.3: Real components (green dashed curve) and imaginary components (red solid line) of dielectric constant of gold due to bound electrons. The used parameters are $\omega_p = 46 \times 10^{14}$, γ= 0.6 eV, λ_0= 450 nm.

The effect of bound electrons contribution to the dielectric constant of gold has been shown in figure 2.3. The observed negative real permittivity in visible range of frequency allows to imagine towards plasmonic metamaterials, involving the optical losses due to increase in the positive imaginary permittivity of gold.

2.3 Importance of metal nanoparticles over metals

A material can exhibit the different properties at different scales. Metals become size and shape dependent at nanoscale with respect to that in bulk. Metal nanostructures have become centre of attraction both for both fundamental and technological reasons

because of their unique physical and chemical properties and functionalities compared to their bulk counterparts. One of the most fascinating property is constituted by their optical response. At nanoscale, metals such as silver and gold, exhibit strong absorption in the visible range along with different colors such as yellowish for silver and violet for gold spherical particles. The origin of this absorption is attributed to collective oscillations of conduction band electrons in response to the electrical field of the electromagnetic radiation of light [12]. This optical absorption is referred to surface plasmons as net charges are displaced transiently on the particle surface during electron oscillation. Thus, the surface plasmon band (SPB) is a strong and broad band observed in the absorption for metallic nanoparticles (NPs) for bigger than 2 nm. For smaller particles, quantum effects are predominant and no SPB is observed [1]. The color and surface plasmon absorption bands of nanostructures are size and shape dependent. Metals such as silver or gold are so important because almost any color or absorption in any part of the visible spectrum can be produced by controlling the shape or structure of the nanomaterials. Examples of various nonspherical metal nanostructures reported in the literature include nanorods, nanoshells, nanowires, nanocages, nanoprisms, and nanoplates [12]. These days, the applications of metal nanostructures have been extended in various interdisciplinary fields such as biomedicine, energy environment, sensing and therapy.

2.4 Localized surface plasmon resonances

When NPs have diameters much lower than incident light wavelength and the penetration depth of the field (diameter around $20\,nm$), the electron cloud of the particle is entirely probed by the electric field. The whole assembly of electrons is polarized, accumulating surface charges alternately on opposite ends of the particle and their collective oscillations are termed as surface plasmon resonance (SPR). Plasmon resonances of NPs under such subwavelength condition confine the electromagnetic field of the light in a nanoscale volume. Such plasmon oscillations are called Localized Surface Plasmon Resonances (LSPRs) as shown in figure 2.4.

The main properties of LSPRs can be understood within the dipolar model and can be summarized as follows:

- Plasmon resonance appears in the UV-Visible (UV-VIS) or Near-Infrared (NR) range for gold or silver nanoparticles. A light beam passing through an assembly

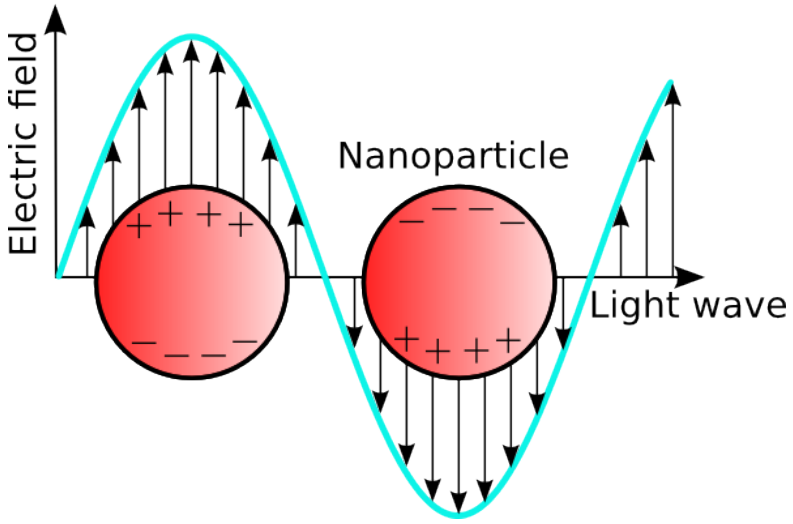

FIGURE 2.4: Sketch of the mechanism of the Surface Plasmon Resonance in a spherical gold nanoparticle.

of homogeneous nanoparticles is partially absorbed at the plasmon resonance frequency so that the emerging beam displays a spectrum with a sharp absorption at $\omega_{plasmon}$. At the same time the nanoparticles exhibit light scattering with a cross section much larger than conventional dye [13].

- LSPRs strongly depend on the environment close to the particle surface.
- When excited at the resonance, the dipole radiates a near-field electromagnetic wave, whose amplitude can be enhanced by a factor up to 10. This plasmon amplification is widely used for enhancing the sensitivity of biosensors.

2.4.1 Theoretical Description of the Localized Plasmon Resonance

When light beam is incident on a nanoparticle, the optical electric field induces oscillations of electrical charges of matter (conduction electrons and protons). As a consequence, one fraction of the impinging beam is absorbed and other is scattered. In order to describe both effects, it is necessary to write down the expressions of electromagnetic fields $\mathbf{E}, \mathbf{H}$ starting from Maxwell's equations. The most famous exact solution of Maxwell's equations for the case of small particles with arbitrary radius and refractive index, has been obtained in the framework of Mie theory [14, 15], developed by Gustav Mie in order to explain observed different colors in absorption and scattering processes

in small colloidal gold nanoparticles dispersed in water. In a linear, isotropic, homogeneous and non-radiative medium, a plane wave, constituted by electric and magnetic fields $(\mathbf{E}, \mathbf{H})$, is incident on small particles and satisfy the following waves equation:

$$\nabla^2\mathbf{E} + r^2k^2\mathbf{E} = 0 \tag{2.15}$$

$$\nabla^2\mathbf{H} + r^2k^2\mathbf{H} = 0 \tag{2.16}$$

where k is the wave vector and r is the refractive index.

The basic idea of Mie theory is to rewrite the incident plane wave as a superposition of spherical waves (through a series expansion) inside and outside the sphere and to impose boundary conditions on the surface to obtain the coefficients of the development. In particular, we can write that inside the sphere:

$$u = e^{i\omega t}cos\phi \sum_{n=1}^{\infty} -a_n(-i)^n \frac{2n+1}{n(n+1)} P_n^l(cos\theta) j_n(kr) \tag{2.17}$$

$$v = e^{i\omega t}sin\phi \sum_{n=1}^{\infty} -b_n(-i)^n \frac{2n+1}{n(n+1)} P_n^l(cos\theta) j_n(kr) \tag{2.18}$$

where P_n^l are the associated Legendre functions and j_n are the spherical Bessel functions of the first kind. In spherical coordinates the wave equation is factored and has solutions of the type:

$$\psi_{n,l} = cosl\phi P_n^l(cos\theta) z_n(mkr) \tag{2.19}$$

$$\psi_{n,l} = sinl\phi P_n^l(cos\theta) z_n(mkr) \tag{2.20}$$

where n and l are integer numbers, z_n are the spherical Bessel function.

By imposing the boundary conditions on the surface of the sphere and introducing the parameter $x = \frac{2\pi a}{\lambda}$ we obtain scattering coefficients:

$$a_n = \frac{\psi_n'(mx)\psi_n(x) - m\psi_n(mx)\psi_n'(x)}{\psi_n'(mx)\varsigma_n(x) - m\psi_n(mx)\varsigma_n'(x)} \tag{2.21}$$

$$b_n = \frac{m\psi_n'(mx)\psi_n(x) - m\psi_n(mx)\psi_n'(x)}{m\psi_n'(mx)\varsigma_n(x) - m\psi_n(mx)\varsigma_n'(x)} \tag{2.22}$$

where ψ and ς are the Riccati-Bessel functions. The scattering cross section is related to a_n and b_n by the relation:

$$\sigma = \frac{2\pi}{k^2} \sum_{n=1}^{\infty} (\mid a_n \mid^2 + \mid b_n \mid^2) \tag{2.23}$$

For small particles ($< 60nm$), it is sufficient to restrain the multipole expansion to its first term (n=1) which correspond to a dipolar case. This approximation is indicated with the dipolar approximation, also called the quasistatic or Rayleigh limit [16]. Mie-coefficient are directly involved in the expression of scattering cross section and polarizability of the sphere. In fact, the scattering cross section C_{sca} is the area associated to the sphere that takes into account the amount of scattered energy. C_{sca} is the ratio of total scattered energy per second to the incident energy per square meter per second. Since $\mathbf{E}_s$ and $\mathbf{H}_s$ are known quantities, by exploiting the Poynting vector, we can evaluate the scattered energy and scattering cross section:

$$C_{sca} = \frac{W_s}{I_i} = \frac{2\pi}{k^2} \sum_{n=1}^{\infty} (2n+1) \left(|a_n|^2 + |b_n|^2 \right) \tag{2.24}$$

Using the simple quasi-static approximation $a \ll \lambda$ in the framework of an electrostatic approach, a solution of the Laplace equation for the potential, $\nabla^2 \Phi = 0$, which will enable calculation of the electric field $\mathbf{E} = -\nabla\Phi$. Due to the azimuthal symmetry of the problem, a general solution can be written such as [17].

$$\Phi(r,\theta) = \sum_{l=0}^{\infty} \left[A_l r^l + B_l r^{-(l+1)} \right] P_l(\cos\theta) \tag{2.25}$$

By solving and using above solution,

$$\mathbf{E} = -\nabla\Phi = -\frac{\partial\Phi}{\partial r}\hat{\mathbf{e}}_\mathbf{r} - \frac{1}{r}\frac{\partial\Phi}{\partial\theta}\hat{\mathbf{e}}_\theta - \frac{1}{r\sin\theta}\frac{\partial\Phi}{\partial\varphi}\hat{\mathbf{e}}_\varphi \tag{2.26}$$

Above expression leads to the calculation of internal field and dipolar field of nanoparticle

$$\mathbf{E}_{in} = \frac{3\varepsilon}{\varepsilon + 2\varepsilon_m}\mathbf{E}_0 \tag{2.27}$$

$$\mathbf{E}_{out} = \mathbf{E}_0 + \frac{3\mathbf{n}(\mathbf{n}\cdot\mathbf{p}) - \mathbf{p}}{4\pi\varepsilon_0\varepsilon_m}\frac{1}{r^3} \tag{2.28}$$

Estimation of the scattered electric field from an ideal dipole, with dipole moment $\mathbf{p}(t) = \varepsilon_0 \varepsilon_m \alpha \mathbf{E}_0 e^{-i\omega t}$ allows to calculate the cross sections:

$$C_{sca} = \frac{k^4}{6\pi}|\alpha|^2 = \frac{8\pi}{3}k^4 a^6 \left|\frac{\varepsilon - \varepsilon_m}{\varepsilon + 2\varepsilon_m}\right|^2 \tag{2.29a}$$

$$C_{abs} = k\Im[\alpha] = 4\pi k a^3 Im\left[\frac{\varepsilon - \varepsilon_m}{\varepsilon + 2\varepsilon_m}\right] \tag{2.29b}$$

For small particles whose radius $a \ll \lambda$, absorption is propotional to a^3 and dominates over the scattering which is propotinal to a^6. For metal nanoparticles both absorption and scattering are resonantly enhanced when the Fröhlich condition ($\Re[\varepsilon(\omega)] = -2\varepsilon_m$) is fulfilled. For a sphere of volume V and dielectric function $\varepsilon = \varepsilon_1 + i\varepsilon_2$ in the quasi-static limit and ε_m is the dielectric constant of medium , the explicit expression for the extinction cross section $C_{ext} = C_{abs} + C_{sca}$ is

$$C_{ext} = 9\frac{\omega}{c}\varepsilon_m^{3/2} V \frac{\varepsilon_2}{[\varepsilon_1 + 2\varepsilon_m]^2 + \varepsilon_2^2} \tag{2.30}$$

Furthermore, if the metallic nanoparticles are immersed in a surrounding medium with gain, another interesting theory is introduced. Such case can be treated by analyzing the case of a sub-wavelength metal nanosphere embedded in a homogeneous medium exhibiting optical gain. The quasi-static approach can be followed, and the presence of gain can be incorporated by replacing the real dielectric constant ε_m of the insulator surrounding the sphere with a complex dielectric function $\varepsilon_2(\omega)$. Using this straightforward analytical model, Lawandy has shown that the presence of gain leads to a significant strength of the plasmon resonance, tackling the optical losses [18]. Incorporation of gain medium to plasmonic structures will be discussed in detail in another chapter of the thesis.

2.5 Experimental parameters influencing plasmon band of NPs

The plasmon band of NPs strictly depends on various parameters such as their size, shape, geometry, metal composition, nature of dielectric environment and the electronic interactions between the stabilizing ligands with NPs [1]. By changing these parameters, plasmon band can be tuned as a function of wavelength as well as its intensity. In

this section, the effects of such parameters on NPs plasmon band have been discussed in brief.

2.5.1 *Size Effects*

In order to understand the impact of NPs size in a clear way, the general approach must be distinguished in two regimes such as small NPs having size smaller than incident light wavelength and large NPs with the size comparable to the light wavelength. Smaller NPs whose radius is up to 50nm, can be properly described by a dielectric dipole. In such case, NPs size only affects the width and the intensity of the plasmon band, while the shift in the resonance wavelength is almost negligible as shown in figure 2.5 [19].

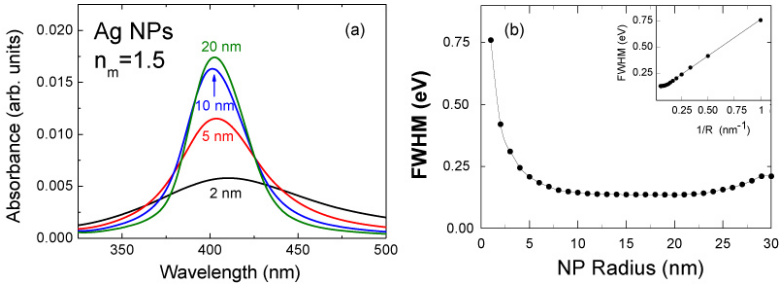

FIGURE 2.5: Plasmon bands of Ag NPs with different sizes calculated according to the Mie theory. (b) FWHM as a function of the particle radius. Inset shows the linear relationship between FWHM and the inverse of the radius [19].

On the other hand, the nanoparticles having radii more than 50 nm are not enough smaller than incident light wavelength and can not be described by a dipole. Multipolar terms are further required which leads splitting in the plasmon bands into several peaks such as two peaks for quadrupole and three peaks for an octopole [20]. Figure 2.6 shows the contribution of the various terms to the extinction cross section of Au NPs. For Au NPs with radius below 60 nm, the quadrupolar term (L = 2) can be neglected. But, multipolar effects must be taken into account, if NP size is further increased. NPs cannot be considered anymore as multipoles and SPs become propagating waves with well-defined modes or dispersion relations [19].

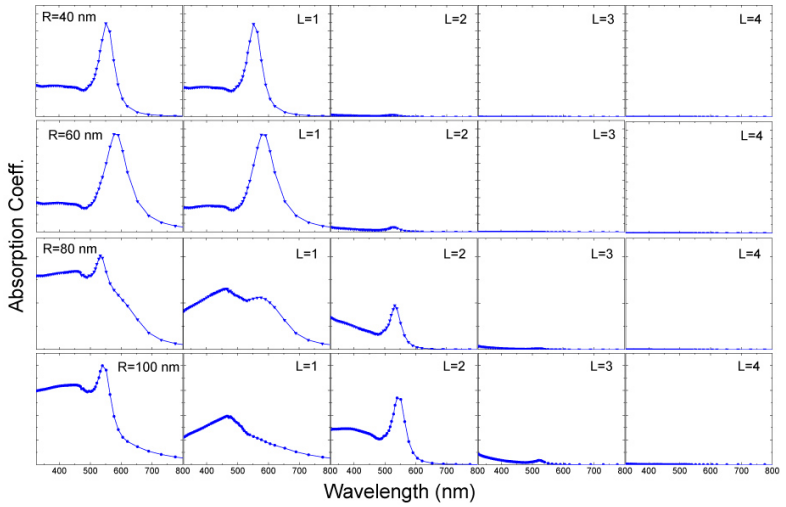

FIGURE 2.6: Plasmon band for Au NP with different sizes calculated according to the Mie theory, and the contribution of the different multipolar terms as a function of wavelength [19].

2.5.2 *Shape Effects*

The plasmon band is strongly affected by the particle shape. Since, the restoring force for SPs is related to the charge accumulated at the particle surface, it will be definitely influenced by the particle geometry. In order to explain shape effects, nanorods are the best example [21]. As figure 2.7(a) explains in the case of nanorod, the charge accumulation at the NP surface will be different for electron oscillations along the rod axis (longitudinal plasmons) and along a perpendicular direction (transversal plasmons). It is evident that the charge accumulation will be maximum for transversal plasmons and minimum for electron displacement along the rod axis (longitudinal plasmons). Thus, the restoring force directly depends on the charge accumulation.

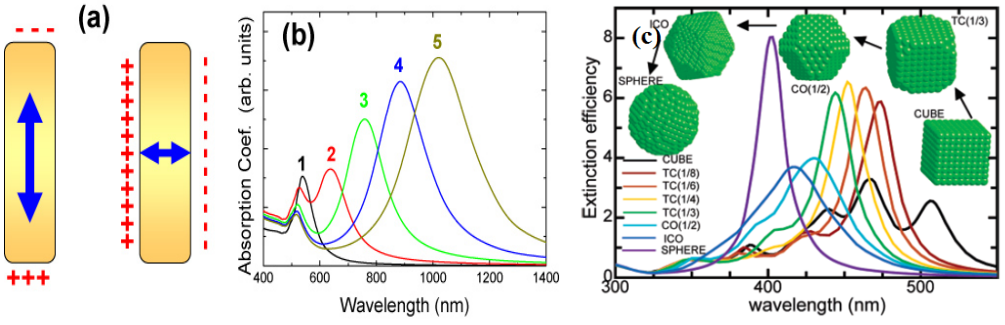

FIGURE 2.7: (a) charge accumulation for longitudinal and transversal SPs in nanorod. (b) Calculated plasmon band for gold nanorods with different aspect ratios indicated as shown in figure [19]. (c) Extinction efficiencies as a function of incident light wavelength of a silver cube, different truncated cubes and a spherical nanoparticle [22].

Smaller forces are expected for electrons oscillating along the rod axis and eventually, which refers to smaller resonance frequencies (larger resonant wavelengths). When the nanorod aspect ratio increases, resonant frequency of transversal plasmons occurs on the same position as for spherical NPs (actually, at wavelengths slightly smaller) the resonance of longitudinal plasmons shifts towards longer wavelengths as shown in figure 2.7(b). This behaviour provides a way to tune the resonance of the SP at the desired wavelength by controlling the aspect ratio. Tuning of plasmon resonances is especially useful for biomedical purposes [19]. Figure 2.7 (c) demonstrates the changes in the extinction efficiency and plasmon resonances as a function of wavelength, when nanocube is truncated to the sphere, approaching through various truncated cubes. Same numbers of polariser entities in all the nanostructures allows the influence of only shape on the plasmon band [22].

2.5.3 *Dielectric Environment Effect*

Extinction cross-section for small NP calculated by Mie explains the significant role of surrounding medium in order to determine plasmon peak position and intensity. Dielectric function of the surrounding medium affects the light wavelength at the vicinity of the NPs and changes the geometry of electric field at the surface of NPs. Charge accumulation creates an electric field closed to the vicinity of NPs. Nature of dielectric function of medium affects charge accumulation, larger value of ε_m enhances the polarization charge at the interface between metal NPs and dielectric medium. This effect reduces the net charge at NP surface causing a reduction in the restoring force. it is obvious that reducing the restoring force leads to smaller resonant frequency. Enhancement in dielectric constant of the surrounding media shifts the SP resonant band towards larger wavelengths as shown in figure 2.8(a) [19]. Figure 2.8(b) exhibits the change in color of gold sole dispersed in water from pale red to violet with respect to the change in refractive indices of surrounding media. This means that dispersion of similar NPs in different dielectric media such as water, ethanol and other transparent oxide matrices leads to a remarkable shift in the plasmon band of NPs.

2.5.4 *Metal Composition and Aggregation Effects*

Noble metals like any other material shows its unique electromagnetic characteristic. Ag, Au and Cu show the plasmon bands at different wavelengths resulting red shift,

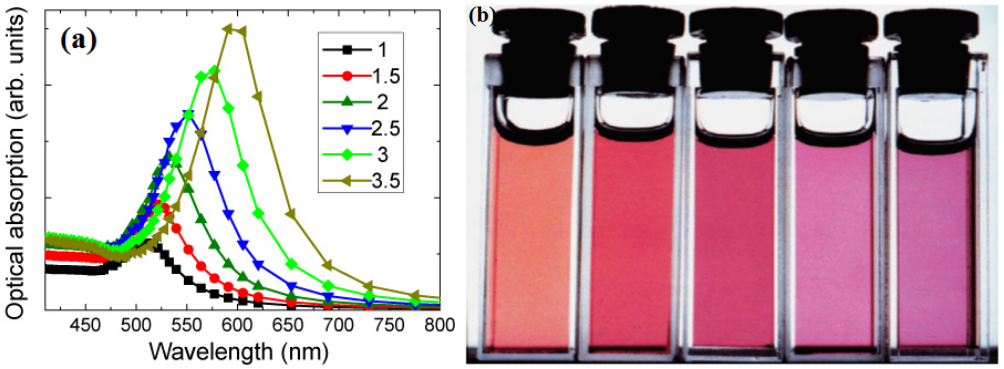

FIGURE 2.8: (a) Plasmon bands for 10nm Au in a dielectric medium with different dielectric functions calculated according to Mie theory [19].(b) Color variation of gold sols from pale red to violet, induced by changing the solvent refractive index. Refractive indices of the solutions at the absorption band maximum are 1.336, 1.407, 1.481, 1.525 and 1.583, respectively [23].

respectively. On the other hand, aggregation in nanoparticles completely changes its plasmonic properties, exhibiting a shift in plasmon band position and change in the band intensity as well as absorption broadening. For an example, the plasmon band of $12-14$ nm gold NPs dispersed in water was observed at 527 nm. Whereas, due to aggregation effect, broad plasmon band along with lower intensity appears around 575nm. Shift in the plasmon band position due to aggregation also changes the color of solutions.

2.6 Surface Plasmon Polaritons

Surface plasmon polaritons (SPPs) are electromagnetic excitations existing at interface of a metal and a dielectric material. The resonant interaction between SPPs and the electromagnetic radiation at metallic interfaces results in a remarkably enhanced optical near-field. SPPs were first observed by Wood in 1902 when he found unexplained features in optical reflection measurements on metallic gratings [24]. Fundamental research and development of SPP-based structures and devices have received centre of attraction due to its peculiar properties and unique applications in optics, surface-enhanced Raman spectroscopy (SERS), data storage, solar cells and sensors [25].
One of the most attractive aspects of SPPs is the way in which they are able to concentrate and channel light using subwavelength structures. This could lead to miniaturized photonic circuits with length scales much smaller than achieved in past. Such circuits would first convert light into SPPs, which would then propagate and be processed by logic elements, before being converted back into light. To build such a circuit one would

require a variety of components: waveguides, switches, couplers and so on. Recently, lot of efforts are being devoted to develop such SPPs devices [26].

2.6.1 Coupling to surface plasmons at metal dielectric interface

When electromagnetic wave is incident on metal dielectric interface, interaction between the surface charge density and the electromagnetic field results in the momentum of the SP mode $\hbar\kappa_{SP}$, which is greater than the momentum of em wave in free space $\hbar\kappa_{inc}$. Momentum mismatch between incident light and SPs modes can be understood by this expression.

$$\kappa_{SP} = \kappa_{inc}\sqrt{\frac{\varepsilon(\omega)\varepsilon_{diel}}{\varepsilon(\omega)+\varepsilon_{diel}}} \tag{2.31}$$

Here, frequency dependent permitivity of the metal ($\varepsilon(\omega)$) and dielectric constant of dielectric medium (ε_{diel}), must have opposite signs for the possibilty of SPs propagation at such an interface. For such condition, metal is suitable candidate as $\varepsilon(\omega)$ is both negative and complex [26, 27]. Figure 2.9 also demonstrates the momentum-mismatch

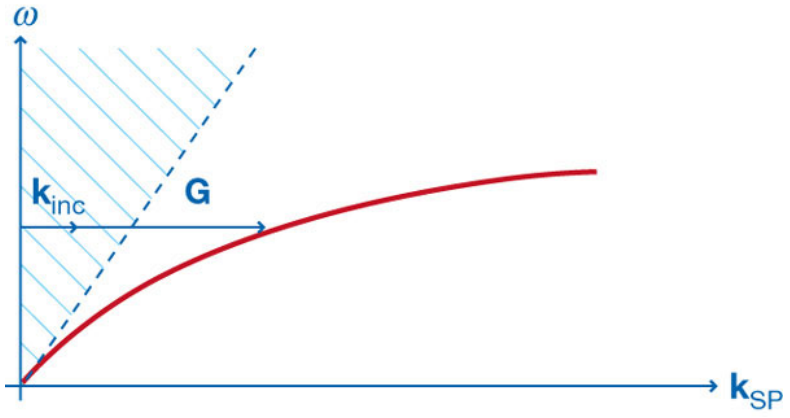

FIGURE 2.9: Red line shows the SP dispersion relation. The dotted line refers to light line. Electromagnetic wave requires an additional G momentum in order to couple with SP mode [28].

between wave vector of incident (blue dotted line) and SPPs modes (red solid line), which can be provided by many techniques. American scientist R. W. Wood proposed a way to provide missing momentum using periodic corrugation in the metal surface which can diffract incident light into the plane of the metal-dielectric interface and results resonant coupling of light with SPs [24]. Figure 2.10 shows two methods to form SPPs on metal dielectric interface such as grating coupling and prism coupling. Mismatch of momenta can be overcome by patterning the metal surface with a periodic

grating of grooves. Moreover, Prism coupling which is also known as attenuated total internal reflection involves two configurations such as Kretschmann configuration and Otto configuration. In the Kretschmann configuration, the prism is in contact with a metal film as shown in figure 2.10(b), while there is an air gap between prism and metal in the Otto configuration (figure 2.10(c)) [27]. Furthermore, periodic and aperiodic hole arrays on metal films also form surface plasmon polaritons and demonstrate exciting new opportunities in applications ranging from subwavelength optics and optoelectronics to chemical sensing and biophysics [28].

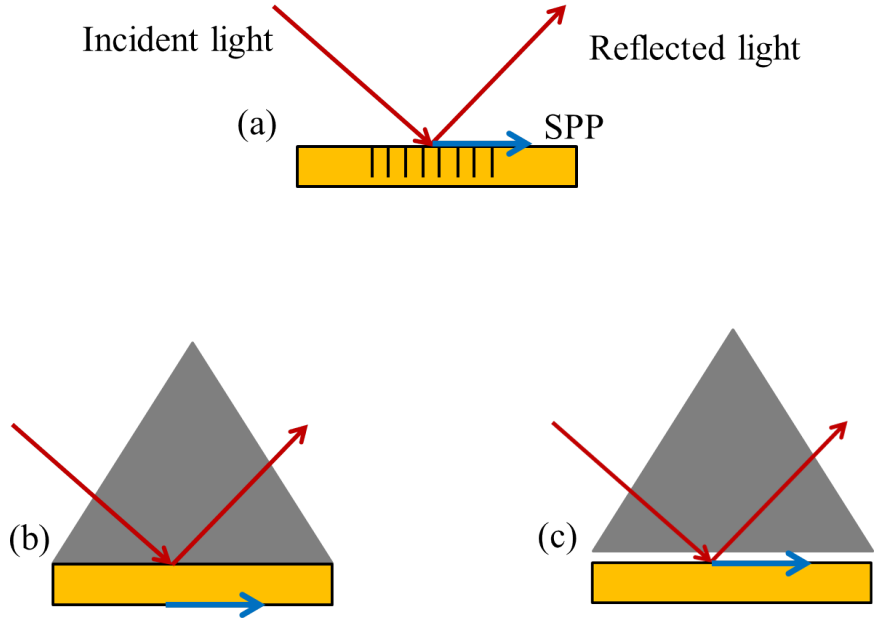

FIGURE 2.10: (a) Phase-matching of light to SPPs using a grating. Blue arrow shows the direction of SPPs . (b) Prism coupling to SPPs using attenuated total internal reflection in the Kretschmann configuration. (c) Prism coupling to SPPs in Otto configuration.

2.6.2 Theory of Surface Plasmon Polaritons

Propagation of surface plasmon polaritons (SPPs) can be explained by using classical approach. As it is described in the above section, SPPs represent an electromagnetic excitation propagating at metal dielectric interface, confined evanescently in the perpendicular direction. In order to investigate the physical properties of SPPs, it is convenient to start from the *Helmholtz equation* [29].

$$\nabla^2 \mathbf{E} + k_0^2 \varepsilon \mathbf{E} = 0 \tag{2.32}$$

where $k_0 = \omega/c$ is the wave vector of the electromagnetic wave propagating in vacuum. This equation is obtained from Maxwell's equations under some assumptions and conditions such as absence of external charge $\nabla \cdot \mathbf{D} = 0$ and harmonic time dependendent electromagnetic field $\mathbf{E}(\mathbf{r},t) = \mathbf{E}_0(\mathbf{r})e^{-i\omega t}$ is incident at single interface. Figure 1.5 shows the assumption of one dimensional problem as ε depends on one spatial coordinate only: $\varepsilon = \varepsilon(z)$; e. m. waves propagate along the x-direction of the cartesian coordinate system and do not show spatial variation along the y-direction. Plane $z = 0$ coincides with the interface. solution under the given conditions can be written as $\mathbf{E}(x,y,z) = \mathbf{E}(z)e^{i\beta x}$; thus, equation (2.32) assumes the form

$$\frac{\partial^2 \mathbf{E}(z)}{\partial z^2} + (k_0^2\varepsilon - \beta^2)\mathbf{E}(z) = 0 \tag{2.33}$$

Equation (2.33) can be used to determine the spatial field profile and the dispersion of propagating waves. Explicit expressions for the different field components of $\mathbf{E}$ and $\mathbf{H}$ should be drived. This can be achieved by using the curl of Maxwell's equation in the absence of external charge along with specific case of harmonic time dependence ($\frac{\partial}{\partial t} = -i\omega$), propagation along the x-direction ($\frac{\partial}{\partial x} = i\beta$) and homogeneity in the y-direction ($\frac{\partial}{\partial y} = 0$). The obtained system of equations is

$$\frac{\partial E_y}{\partial z} = -i\omega\mu_0 H_x \tag{2.34a}$$

$$\frac{\partial E_x}{\partial z} - i\beta E_z = i\omega\mu_0 H_y \tag{2.34b}$$

$$i\beta E_y = i\omega\mu_0 H_z \tag{2.34c}$$

$$\frac{\partial H_y}{\partial z} = i\omega\varepsilon_0\varepsilon E_x \tag{2.34d}$$

$$\frac{\partial H_x}{\partial z} - i\beta H_z = -i\omega\varepsilon_0\varepsilon E_y \tag{2.34e}$$

$$i\beta H_y = -i\omega\varepsilon_0\varepsilon E_z \tag{2.34f}$$

The above equations provide two sets of self-consistent solutions with different polarization characteristics of the propagating waves as the Transverse Magnetic mode (TM), which contains nonzero field components E_x , E_z and H_y and the Transverse Electric mode (TE), having nonzero H_x , H_z and E_y. For TM modes, by starting from (2.34d)

and (2.34f) we obtain the expression of E_x and E_z as functions of H_y:

$$E_x = -i\frac{1}{\omega\varepsilon_0\varepsilon}\frac{\partial H_y}{\partial z} \tag{2.35a}$$

$$E_z = -\frac{\beta}{\omega\varepsilon_0\varepsilon}H_y \tag{2.35b}$$

Here, H_y has to be obtained from the solution of the TM wave equation

$$\frac{\partial^2 H_y}{\partial z^2} + (k_0^2\varepsilon - \beta^2)H_y = 0 \tag{2.35c}$$

For TE modes, the analogous set is

$$H_x = i\frac{1}{\omega\mu_0}\frac{\partial E_y}{\partial z} \tag{2.36a}$$

$$H_z = -\frac{\beta}{\omega\mu_0}E_y \tag{2.36b}$$

where E_y has to be obtained from the TE wave equation

$$\frac{\partial^2 E_y}{\partial z^2} + (k_0^2\varepsilon - \beta^2)E_y = 0 \tag{2.36c}$$

Using above equations, SPPs can be described at a single, flat interface (Figure1.5) between a dielectric, non-absorbing half space ($z > 0$) characterized by a positive real dielectric constant ε_{diel}, and a conducting half space ($z < 0$) characterized by a dielectric function $\varepsilon(\omega)$. Propagating waves can be observed at the interface, i.e. with evanescent decay in the perpendicular z-direction. Propagation of SPPs can be understood on the basis of two cases TM and TE.

For TM case. Using the equation set (2.35) in both half spaces, and searching for solutions of (2.35c) that are propagating in the x-direction and exponentially decreasing along the z-direction, solutions are obtained

$$H_y(z) = A_2 e^{i\beta x} e^{-k_2 z} \tag{2.37a}$$

$$E_x(z) = iA_2\frac{1}{\omega\varepsilon_0\varepsilon_2}k_2 e^{i\beta x} e^{-k_2 z} \tag{2.37b}$$

$$E_z(z) = -iA_2\frac{\beta}{\omega\varepsilon_0\varepsilon_2}e^{i\beta x} e^{-k_2 z} \tag{2.37c}$$

for $z > 0$ and

$$H_y(z) = A_1 e^{i\beta x} e^{k_1 z} \tag{2.38a}$$

$$E_x(z) = -iA_1 \frac{1}{\omega \varepsilon_0 \varepsilon_1} k_1 e^{i\beta x} e^{k_1 z} \tag{2.38b}$$

$$E_z(z) = -A_1 \frac{\beta}{\omega \varepsilon_0 \varepsilon_1} e^{i\beta x} e^{k_1 z} \tag{2.38c}$$

for $z < 0$.

Here A_1, A_2 are magnetic field amplitudes, $k_{z,i}$ $(i = 1,2)$ is the component of the wave vector perpendicular to the interface in the two media; its reciprocal value, $\hat{z} = \frac{1}{|k_z|}$, defines the ***evanescent decay length*** of fields perpendicular to the interface, which quantifies the confinement of the wave. Continuity of H_y, E_x and $\varepsilon_i E_z$ at the interface ($z = 0$) requires that $A_1 = A_2$ and

$$\frac{k_2}{k_1} = -\frac{\varepsilon_{diel}}{\varepsilon(\omega)}. \tag{2.39}$$

According to the convention assumed for signs in the exponents in (2.37, 2.38), confinement to the surface demands that $\Re[\varepsilon(\omega)] < 0$ if $\varepsilon_{diel} > 0$, thus surface waves can exist only at interfaces between materials with opposite signs of the real part of their dielectric permittivity, i.e. between a conductor and an insulator. In addition, the expression for H_y has to fulfill the wave equation (2.35c), yielding

$$k_1^2 = \beta^2 - k_0^2 \varepsilon(\omega) \tag{2.40a}$$

$$k_2^2 = \beta^2 - k_0^2 \varepsilon_{diel} \tag{2.40b}$$

By combining equations (2.39) and (2.40) we obtain the main result concerning the argument of this section, that is the dispersion relation of SPPs propagating at the interface between a conductor half space and an insulator one:

$$\beta = k_0 \sqrt{\frac{\varepsilon(\omega)\varepsilon_{diel}}{\varepsilon(\omega) + \varepsilon_{diel}}} \tag{2.41}$$

This expression is valid both for real and complex ε, i.e. for conductors without and with attenuation.

For TE case, expressions for the field components can be obtained by using equation (2.36),

$$E_y(z) = A_2 e^{i\beta x} e^{-k_2 z} \tag{2.42a}$$

$$H_x(z) = -iA_2 \frac{1}{\omega\mu_0} k_2 e^{i\beta x} e^{-k_2 z} \tag{2.42b}$$

$$H_z(z) = A_2 \frac{\beta}{\omega\mu_0} e^{i\beta x} e^{-k_2 z} \tag{2.42c}$$

for $z > 0$, and

$$E_y(z) = A_1 e^{i\beta x} e^{k_1 z} \tag{2.43a}$$

$$H_x(z) = iA_1 \frac{1}{\omega\mu_0} k_1 e^{i\beta x} e^{k_1 z} \tag{2.43b}$$

$$H_z(z) = A_1 \frac{\beta}{\omega\mu_0} e^{i\beta x} e^{k_1 z} \tag{2.43c}$$

for $z < 0$.
Here, A_1, A_2 are now electric field amplitudes. Continuity of E_y and H_x at the interface leads to the condition $A_1 = A_2$ and

$$A_1(k_1 + k_2) = 0. \tag{2.44}$$

Condition (2.44) cab be only fulfilled if $A_1 = 0$, which also means means $A_2 = 0$. It concludes that no surface modes can exist with TE polarization. In the case of multilayers, consisting alternate conducting and dielectric thin films, each single interface supports bound SPPs. When the separation between adjacent interfaces is comparable or smaller than the decay length $\hat{z}$ of the interface mode. Interactions between SPPs give rise to coupled modes [27].

Chapter 3

Introduction to Metamaterials

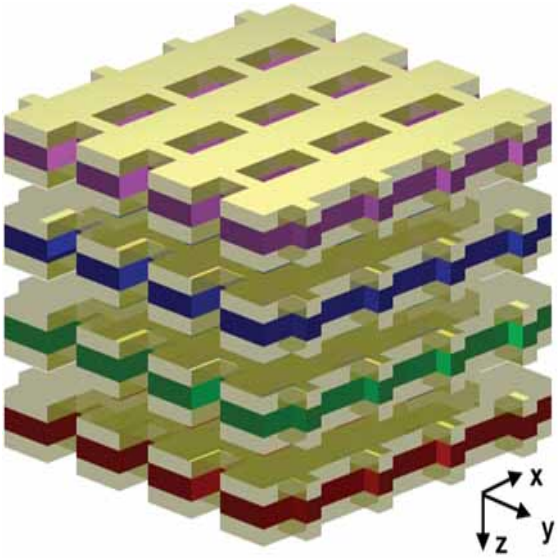

3.1 What are Metamaterials ?

Refractive index is one of the most essential parameters of light propagation in materials. Dexterous control of refractive index in materials and devices leads towards innumerable and innovative real life applications. The refractive index is a complex number

$$n = n_1 + in_2 \tag{3.1}$$

Where the real part of the refractive index n_1 reports how phase velocity of light decreases in materials with respect to vacuum. The imaginary part n_2 belongs to light extinction (losses) in the systems [30]. Moreover, refractive index is obtained on the basis

of electric permitivity ε and magnetic permeability μ of materials, which represent the coupling of material to the electric and magnetic field components of light, respectively. Basically, permitivity and permeability describe how electric and magnetic fields affect and get affected by a medium, respectively depending on the ability of a material to polarize in response to the electric and magnetic fields. Material parameter space has been formed and divided into four quadrants based on the classification of sign of ε and μ. The first quadrant ($\varepsilon > 0$ and $\mu > 0$) covers right-handed materials (RHM) as

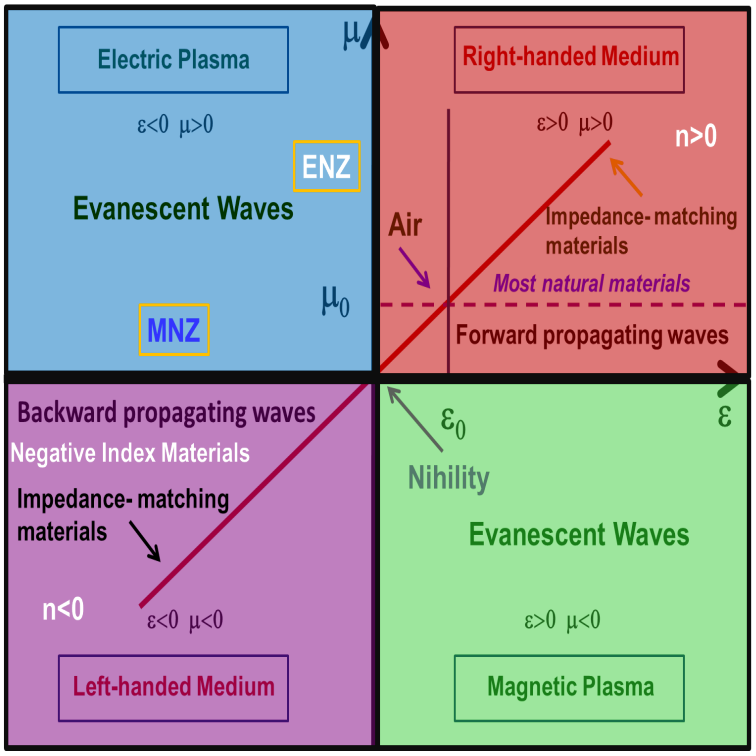

FIGURE 3.1: Material parameter space characterized by electric permittivity (ε) and magnetic permeability (μ).

shown in figure 3.1. According to Maxwell's equations for the positive ε and μ, electric field E, magnetic field H, and wave vector k form a right-handed system, supporting the forward propagating waves. Transparent dielectric materials and almost all natural materials lie in this quadrant [31]. Second and fourth quadrants represent the materials with one of two parameters ε or μ with negative sign, resulting purely imaginary refractive index. In such media, a negative sign of ε or μ means that the direction of the electric (magnetic) field induced inside the material is in the opposite direction to the incident field, and consequently, propagation of waves cannot be supported. In the case of negative ε and positive μ, second quadrant includes metals, ferroelectric materials and doped semiconductors demonstrating negative permittivity at certain frequencies (below the plasma frequency). While, the fourth quadrant ($\varepsilon > 0$ and $\mu < 0$) refers to

magnetic plasma in which negative permeability can be found in ferromagnetic media closed to resonance frequency.

The third quadrant ($\varepsilon < 0$ and $\mu < 0$) embraces the presence of negative phase velocity of electromagnetic waves due to the presence of negative refractive index. Under this condition, **E**, **H** and **K** form left handed system, resulting the wave vector **K** and Poynting vector S oriented in opposite directions. Such systems were proposed by Veselago and also known as *Veselago materials* [32] or *Negative Index Materials* (NIMs). However, no natural materials exhibit negative refractive indices. Veselago's fabulous theoretical work on NIMs was hibernated until 2000. Sir John Pendry, who first proposed to use artificial materials as a perfect lens in order to exploit an extra ordinary electromagnetic properties [33] and a opened up completely new research area called *Metamaterials*. The word '*meta*' means 'beyond' in Greek, metamaterials refer to the materials whose properties go beyond conventional materials.
Thus, *Metamaterials are defined as artificially engineered structures, consisted of subwavelength subunits which demonstrate unprecedented electromagnetic properties that cannot be obtained in natural materials.*

3.2 Journey towards the realisation of metamaterials

Before fabricating a metastructure which consists of periodically or random distributed subwavelength elements, it is noteworthy that electromagnetic wave can not be incident on a single structured element. An overall permittivity ε and permeability μ of the system must be taken in account in terms of effective permitivity ε_{eff} and effective permeability μ_{eff} in order to understand the negative refraction behaviour of the system. By designing the subwavelength elements, ε_{eff} and μ_{eff} can be controlled to have negative values, a necessary condition for metamaterials.

In 1996, Pendry proposed dilute metals with extremely low plasma frequency. Thin metallic wires in three dimension configuration exhibit reduced effective electron density and an increase in effective electron mass due to self inductance of the wire structure as shown in figure 3.2(a). The effective permittivity of the metallic wire arrays is plotted in figure 3.2(b) showing the negative real permittivity [34]. Furthermore, Pendry also showed the observation of negative permeability in nonmagnetic artificial split ring resonators (SRRs) which are composed of two concentric split rings with the openings at the opposite directions as shown in figures 3.2(c) and (d) [31]. Following this approach,

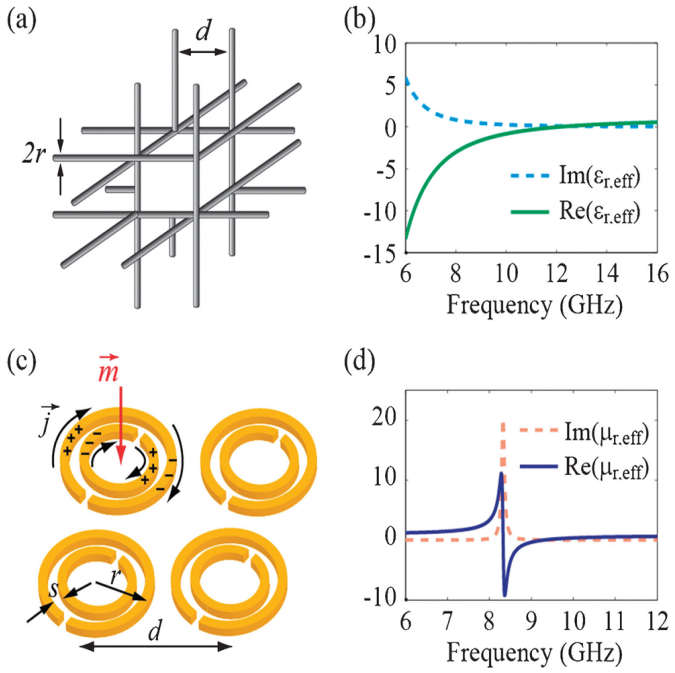

FIGURE 3.2: Demonstration of metastructutre along with artificial electric and magnetic responses. (a) Schematic of periodic wires (with radius r) arranged in a simple cubic lattice (with lattice constant d). (b) Effective permittivity of wire media, acting as dilute metals with an extremely low plasma frequency. (c) Schematic of split ring resonators, with outer radius r and separation s between the two rings. A magnetic field penetrating the resonator induces a current (j), and thus a magnetic moment (m). (d) Effective permeability of split ring resonators around the resonance frequency[31].

theoretically shown by Pendry, Smith and his colleagues successfully demonstrated the first negative index metamaterial in the microwave region [35, 36]. But, such structures have difficulty in the observation of negative ε and μ at single point. The most exciting metamaterial so called double fishnet cosisted of two layers of metal meshes separated by a dielectric spacer layer was devised in 2005 and being improved in next years [37]. Invisible cloak in the microwave region, magnetic resonance imaging, novel microwave circuits and antennas at microwave region and the prefect lens beating the diffraction limit are some of the few successful examples which are driven by growing metamaterials research [31, 33, 38].

3.3 Optical metamaterials

Optical metamaterials received center of attraction among scientific community due to the possibilities of novel applications such as invisible cloaking, waveguiding and imaging beyond the diffraction limit in the optical range. In order to experimentally realize

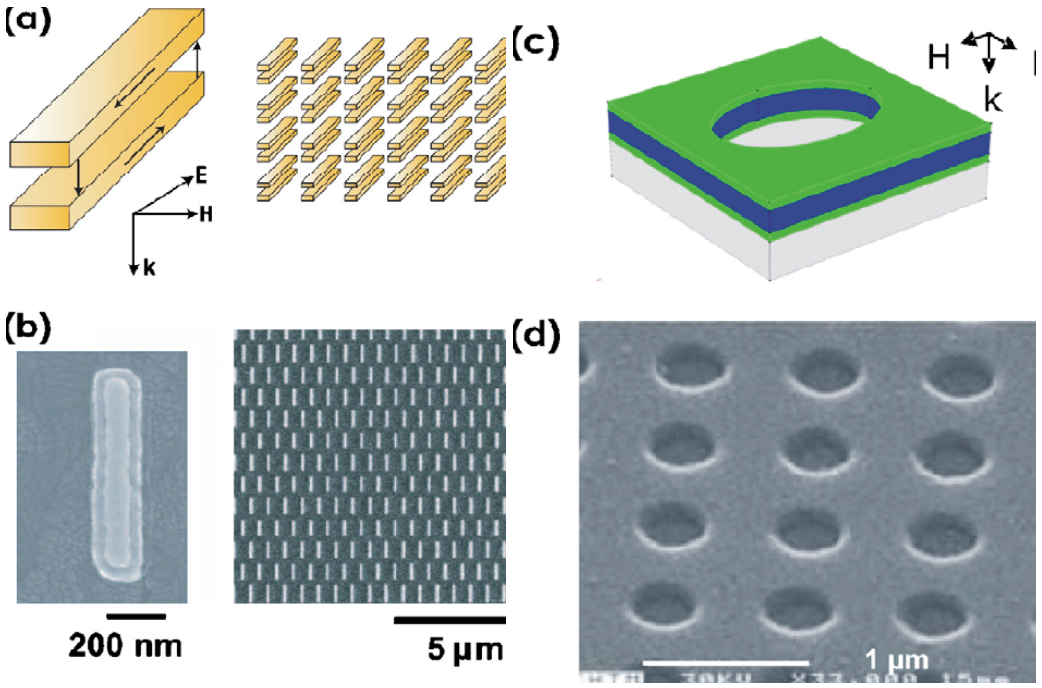

FIGURE 3.3: Figure shows first optical negative index metamaterials (a) Sketch of an array of paired Au nanorods separated by a SiO_2layer (b) field-emission scanning electron microscope images of the fabricated array (Au(50 nm)–SiO_2(50 nm)–Au(50 nm) stacks)[39].(c) Sketch of a multilayer structure consisting of a dielectric layer between two metal films perforated with a hole on a glass substrate (d) scanning electron microscope image of the fabricated structure (Au(30 nm) Al_2O_3(60 nm)–Au(30 nm) stack, 838 nm pitch, 360 nm hole diameter), exhibiting negative index at about $\lambda \sim 2\mu m$ [37].

optical metamaterials, the size of metamaterial subunits has to be much smaller than incident wavelength and the gap between SRRs should be less than 10 nanometer to observe magnetic resonance at optical frequencies. The fabrication of optical metamaterials becomes challenging issue because of high quality of precision, high-throughput and low-cost manufacturing processes. Despite tremendous advances in nanofabrication methods, metastructures can not be designed to that extent where the subunits size is orders of magnitude smaller than the incident wavelength. Negative refractive index in the optical range was successfully demonstrated almost at the same time for two different metal–dielectric geometries with the pairs of metal rods seperated by dielectric layer [39] and the inverted system of pair of dielectric voids in a metal–dielectric–metal multilayer [37].

Shalev and coworkers fabricated an array of pairs of parallel 50 nm thick gold rods separated by 50 nm of SiO_2 spacer using electron-beam lithography. Such coupled rods-based metastucture demostrated a negative refractive index of n = -0.3 at 1.5 μm [39] as shown in figure 3.3 (a) and (b). At the same time, another research group proposed that two dimensional array of holes in a multilayer structure, designed by 60 nm thick Al_2O_3

dielectric layer between two 30 nm thick Au layers exhibit a negative refractive index of -2 around 2μm [37]. Such structures occur negative real permeability along large positive peak in imaginary permeability, inducing the optical looses in the system. Figure of merit evaluates the performance of the metastructures. These first experimentally realised metamaterials have a high loss coefficient, which exhibit improved efficiency by designing the ellipsoidal voids instead of circular voids as shown in figure 3.3(c) and (d) and using fishnet structure rather than metal rods [40]. Despite such improvements, the optical losses still remains a big problem, limiting the performance of metamaterials and shadowing novel applications.

3.3.1 Figure of Merit

Figure of Merit (FOM) represents the efficiency of a designed metamaterial and is defined as the ratio of the real part to the imaginary part of the effective refractive index.

$$FOM = -\frac{Re[n_{eff}(\omega)]}{Im[n_{eff}(\omega)]} \tag{3.2}$$

As the above equation suggests itself, in order to have high FOM, one should design the metastructure, exhibiting low value of imaginary effective refractive index. Fabrication of a device with lower imaginary refractive index leads towards the efficient and low loss devices. Noteworthy noble metal nanoparticles (NPs), exploited as subwavelength structural elements for plasmonic metamaterials also exhibit large values of imaginary part in visible range, which make optical metamaterials obstructive for most optical applications. Many strategies are still being implemented to tackle absorptive losses including incorporation of gain media, electromagnetic induced transparency and search of alternative materials instead of metals.

3.4 Gain Induced Metamaterials

Now, it is well known that the optical losses limit the numerous potential applications for metamaterials. For example, optical losses must decrease exponentially to observe a linear enhancement in the spatial resolution to enable subwavelength resolution in

superlens [41]. Stem from surface roughness, quantum size and chemical interface effects, the resonant nature of their magnetic response and fundamental loss properties of their constitutive components like metals are the main sources of optical losses in the metastuctures. The first approach was the use of alternative negative and positive index layers to tackle the losses in metamaterials [42]. Such stack system reduces the loss experienced by an electromagnetic wave with respect to the loss in bulk negative-phase medium. Incorporation of gain media with sufficient level is a fascinating possibility to compensate the optical losses. Very soon, the positive index layers were replaced by gain-dielectric layers. The quest to design gain asssited metamaterial en-

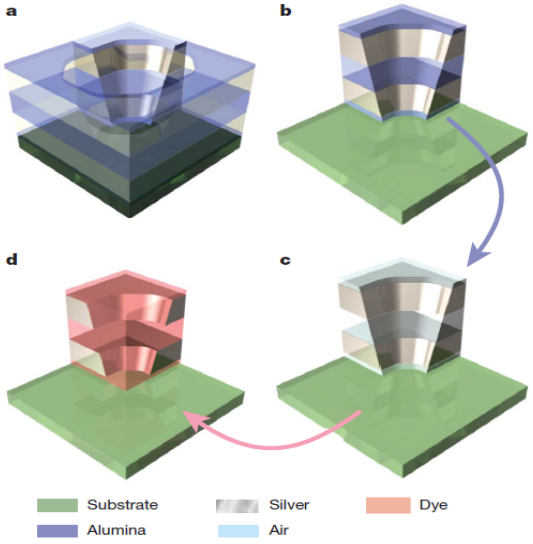

FIGURE 3.4: Scheme of the fabrication method of fishnet subunit. (a) Unit cell of the fishnet structure with alumina as the spacer material between two silver layers. (b) One-quarter of the fishnet structure with an alumina spacer. (c) After etching the alumina, the fishnet structure has air or solvent as the spacer with alumina pillars as support. (d) After coating with Rh800–epoxy, the fishnet structure has the dye–epoxy material in the spacer region and above the fishnet structure[43]

.

couraged towards the development of photonic metamaterials based on metal–dielectric engineered structures. Gain medium in the form of dye molecules (Rhodamine 6G) or semiconductor quantum dots (CdSe) have been applied to the top of the negative phase medium (NIM). Negative index double silver layer seperated by Al_2O_3 layer immersed in gain media demonstrates an enhancement in transparency as a function of gain [44]. Furthtermore, gain functionalised fishnet structure led towards an extremely low-loss, improved figure of merit and active optical negative index metamaterials as shown in figure 3.4. Such structures have been called active metamaterials as the sum of the light intensities in transmission and reflection exceed the intensity of the incident beam. Inclusion of gain layer between the metal layers of near-field superlens improved the

resolution of superlens[45].
However, design and fabrication of metamaterials along with an optimal amount of gain medium still remains a challenge for scientific community. In the context of plasmonic NPs assembled metamaterials, metal NPs are efficient quenchers of fluorescence emission from gain which limits the use of gain materials with NPs. Effective use of gain in plasmonic systems will be described in the next chapters of this thesis.

3.5 Fabrication Methods of Optical Metamaterials

Optical metamaterials can be realised by using the both techniques, top down and bottom up approaches. Most of the fabricated optical metamaterials have been fabricated using lithography-based approaches. Nanofabrication paves a path towards advanced metamaterials using focused ion beam milling, interference lithography for large scale fabrication, nanoimprint lithography for high resolution and large fabrication and the design of 3D metasructure using multilayer approach [46]. These all methods are called as top down fabricatiopn approach, crafting bulk metal layers to metastructures. Metamaterials described in figures 3.3and 3.4 demonstrate the examples of top down approach. On the other hand, Bottom-up fabrication techniques based on nanochemistry provide new methods and promise novel application which can not be achieved using top down approaches. metamaterials. Recent advances in nanochemistry route enabled the synthesis of core-shell NPs, nanorods, nanorice, nanoeggs, nanocups, nanostars and many more plasmonic systems[47–50]. Such plasmonic nanostructures find applicatiopns from biomedicine, sensing to devices.
However, optical metamaterials fabrication at optical wavelength, using e-beam lithography or focused ion beam approach involves the use of very delicate and costly instruments and produces extremely small sample volumes size on square micrometer scale. Furthermore, top down approach is only applicable for nano-patterning on hard substrates, not on flexible substrates, limiting many novel applications. The above discussed drawbacks create restrictions in the fabrication of optical metamaterials. In such scenario, bottom up fabrication of optical metamaterials has attracted much attention due to very simple, low cost and large area sample production using self assembly techniques. Self assembly involves the spontaneous organization of nano elements under the effect of complex pair interactions and leads to rise of two-dimensional or three-dimensional metastructures [51, 52].

3.6 Self Assembled Metamaterials

Theoretical studies suggest that organisation of metal NPs in a particular way, attain negative magnetic permeability and negative index of refraction at infrared and optical frequencies. Figure 3.5(a) represents the sketch of arrangement of N nanoparticles which are displaced by distance r from the origin of Cartesian reference system. Such arrangement of metal NPs called ring inclusion, demonstrates resonant magnetic dipole collective response in the visible range and obtain negative effective permeability , when such nano-inclusions are placed in a host medium. Each NPs induces a circulating current in the ring inclusion due to plasmonic resonant feature of the system [53].

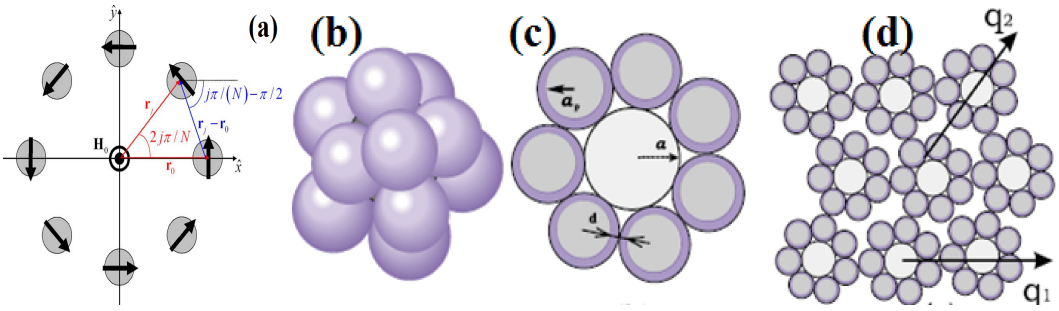

FIGURE 3.5: All magnetic nanoclusters show negative permitivity as well as negative permeability at optical frequencies. (a) Ring inclusion fabricated of N nanoparticles symmetrically displaced by distance r from the origin of a Cartesian reference system [53]. (b) Schematic of optical magnetic nanocluster plasmonic core shell NPs located on a dielectric core. Cross section of a magnetic nanoclusters. (c) two dimensional sketch of a bcc lattice of magneric nanoclusters [52].

Moreover, Simovski group further studied such structures and reported that it is difficult to realise the body centered and face centered lattices using the ring inclusions and purposed a new plasmonic stucture made of the cluster of core-shell nanoparticles (silica-core and metal-shell) centered by a silica core as shown in figure 3.5(b), (c) and (d) [52]. Such clusters attain negative permitivity and negative permeability at optical frequencies, but at the cost of high absorptive losses.

3.7 Hyperbolic Metamaterials

Hyperbolic metamaterials (HMMs) can be entitled as one of the most unusual class of electromagnetic metamaterials. HMMs demostrate hyperbolic dispersion, originating from one of the principal components of their electric or magnetic effective tensor, exhibiting the opposite sign to other two principal components. Such anisotropic

metamaterials receive a lot of attention in this decade due to ease of nanofabrication, broadband nonresonant response, optical wavelength tunability and high figure of merit with respect to other realised metamaterials and are the promising nanostructures for the enhanced spontaneous emission, effective superlensing, fluorescence engineering and nanosensing.

3.7.1 Anisotropic medium

Inspired from Veselago's theory of left handed materials and Pendry's perfect lens, research on metamaterials was revolved around realisation of artificial magnetic response from nonmagnetic materials at optical frequencies in 20^{th} century. But, Landau et al changed the whole scenario by purposing that permeability (μ) must be equal to unity in the optical regime. In an isotopic medium, permeability is defined as

$$\mu = 1 + 4\pi\left(\frac{M}{H}\right) \tag{3.3}$$

Here M and H refer magnetic dipole moment per unit volume and applied magnetic field, respectively. At optical frequencies, M can be ignored due to negligible values [54]. Moreover, It was also pointed out that propagation of wave in linear as well as nonlinear media can be fully described by electrical permittivity, excluding the magnetic permeability and H field component. Systems can be defined by using this relation.

$$D = \tilde{\varepsilon}(\omega, \kappa)E \tag{3.4}$$

Dielectric tensor $\tilde{\varepsilon}(\omega, \kappa)$ itself includes the effect of magnetic response indirectly. Such systems are allowed to be anisotropic and spatial dispersive due to dielectric tensor [55]. Furthermore, Agranovich successfully applied $\tilde{\varepsilon}(\omega, \kappa)$ to describe a system with $\varepsilon < 0$ and $\mu < 0$, confirming the absence of magnetic dipole type resonance in the left handed medium.

This approach led towards the development of special class of metamaterials called *Hyperbolic Metamaterials* (HMMs).

3.7.2 Fundamentals of hyperbolic metamaterials

The electric displacement vector D and field E are do not always remain always parallel in electrically anisotropic media. They are connected by the constitutive equation D = $\tilde{\varepsilon}(\omega,\kappa)$. Hyperbolic behavior originates from uniaxial media, where where $\varepsilon_x = \varepsilon_y = \varepsilon$ and $\varepsilon \neq \varepsilon_z$. It is is defined from the isofrequency curve of the medium which is hyperbolic as opposed to circular as in conventional dielectrics.

In Such media, the constitutive relations connecting the electric displacement D and the magnetic induction B to the electric and magnetic fields E and H can be written as

$$\mathbf{D} = \varepsilon_0 \tilde{\varepsilon} \mathbf{E} \tag{3.5}$$

$$\mathbf{B} = \mu_0 \tilde{\mu} \mathbf{H} \tag{3.6}$$

where ε_0 andμ_0 are vacuum permeability and permittivity, respectively,while and $\tilde{\varepsilon}$ and $\tilde{\mu}$ stand for relative permeability and permittivity tensors. As discussed in the above subsection, μ simply reduces to the unit tensor and electric permitivity tensor $\tilde{\varepsilon}$ can be written in in a Cartesian frame of reference oriented along the so-called principal axes of the crystal.

$$\tilde{\varepsilon} = \begin{bmatrix} \varepsilon_{xx} & 0 & 0 \\ 0 & \varepsilon_{yy} & 0 \\ 0 & 0 & \varepsilon_{zz} \end{bmatrix}$$

All three diagonal components of above matrix are positive and depend on the angular frequency ω. Such media are called biaxial when $\varepsilon_{xx} \neq \varepsilon_{yy} \neq \varepsilon_{zz}$, transform to uniaxial media when , $\varepsilon_x = \varepsilon_y = \varepsilon$ and $\varepsilon \neq \varepsilon_z$ and become isotropic when $\varepsilon_x = \varepsilon_y = \varepsilon_{zz}$. In order to understand the dispersion relation of electromagnetic wave in medium, consider the following two Maxwell's equations in the absence of sources.

$$\nabla \times \mathbf{E} = -\frac{\partial \mathbf{B}}{\partial t} \tag{3.7}$$

$$\nabla \times \mathbf{H} = \frac{\partial \mathbf{D}}{\partial t} \tag{3.8}$$

Solving the above equations using electric and magnetic field components $E = E_0 e^{(\omega t - k.r)}$ and $H = H_0 e^{(\omega t - k.r)}$, we get

$$\begin{aligned} \mathbf{k} \times \mathbf{E} &= \omega \mu \mathbf{H} \\ \mathbf{k} \times \mathbf{H} &= -\omega \varepsilon \mathbf{E}. \end{aligned} \tag{3.9}$$

These two above equations can also be expressed for isotropic as well as anisotropic medium.

For istropic medium, the linear dispersion and isotropic behavior of propagating waves shows a spherical isofrequency surface given by the equation

$$(k_x^2 + k_y^2 + k_z^2) = \frac{\omega^2}{c^2} \tag{3.10}$$

ω is the frequency of radiation and c is the velocity of light in free space. On the other hand, an extraordinary waves (transverse mode polarised) propagate in an uniaxial medium, this isofrequency relation converts to

$$\left(\frac{k_x^2 + k_y^2}{\varepsilon_{zz}} + \frac{k_z^2}{\varepsilon_{\parallel}} \right) = \frac{\omega^2}{c^2} \tag{3.11}$$

Dielectric response of uniaxial medium has been shown by a ε tensor where the in-plane isotropic components are $\varepsilon_{xx} = \varepsilon_{yy} = \varepsilon_{\parallel}$ and out of plane component is $\varepsilon_{zz} = \varepsilon_{\perp}$. Spherical isofrequency surface of vacuum converts to an ellipsoid for the anisotropic case. when we have extreme anisotropy which means that$\varepsilon_{\parallel} \cdot \varepsilon_{\perp} < 0$, the isofrequency surface opens into an open hyperboloid. Such phenomenon requires the material to behave like a metal in one direction and a dielectric (insulator) in the other direction [56].

3.7.3 Classification of hyperbolic metamaterials

Hyperbolic metamaterials can be classified based on the sign of components of dielectric tensor.

Dielectric and Metals : If all the three components of dielectric tensor $(\varepsilon_{xx}, \varepsilon_{yy}, \varepsilon_{zz})$ are negative, such medium behave like an effective metal and propagating wave are not allowed through this medium. On the other hand, if all the components are positive, we

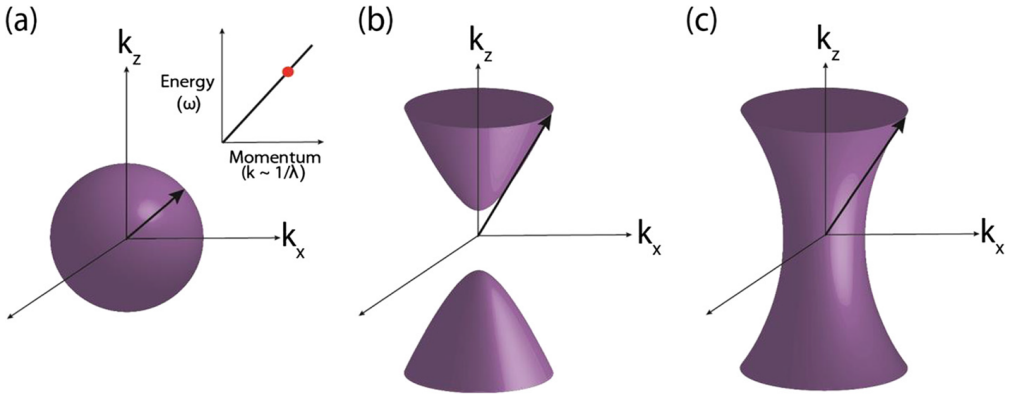

FIGURE 3.6: (a) Spherical isofrequency surface for an isotropic dielectric. Inset shows energy versus momentum relationship with the red dot indicating the operating frequency for the derived isofrequency surface. (b) Hyperboloid isofrequency surface for a uniaxial medium with an extremely anistropic dielectric response for Type I HMM (ε_{xx}, $\varepsilon_{yy} > 0$ and $\varepsilon_{zz} < 0$). (c) Hyperboloid isofrequency surface for an extremely anistropic uniaxial medium with two negative components of the dielectric tensor for Type II HMM (ε_{xx}, $\varepsilon_{yy} < 0$ and $\varepsilon_{zz} > 0$) [56].

will have a dielectric medium as shown in figure 3.6 (a) .

Type I HMMs : If there is only one negative component in tensor and other two are positive such as $\varepsilon_{zz} < 0$ and ε_{xx}, $\varepsilon_{yy} > 0$. Such metamaterials are called Type I HMMs as shown in figure 3.6(b) and have low losses because of dominated dielectric nature, but are difficult to realise experimentally due to nanofabrication limitation.

Type II HMMs : In reverse case with respect to Type I HMMs, Type II HMMs have two components are positive and one negative such as ε_{xx}, $\varepsilon_{yy} < 0$ and $\varepsilon_{zz} > 0$ as shown in figure 3.6 (c). Such mematerials have higher losses and high impedance mismatach with vacuum due to metallic behavior of Type II HMM [57].

Type I and Type II metamaterials can support waves with infinitely large wavevectors in the effective medium limit. Such waves are evanescent and decay away exponentially in vacuum.

3.7.4 Realization and materials for HMMs

Metals exhibit negative real part of the dielectric function below the plasma frequency due to opposite directional polarization response of free moving electrons with respect to the electric field. In hyperbolic media, the components of the dielectric tensor are negative in only one or two spatial directions, which can be achieved by restricting free electron motion to these directions [57]. Most common way to realize hyperbolic

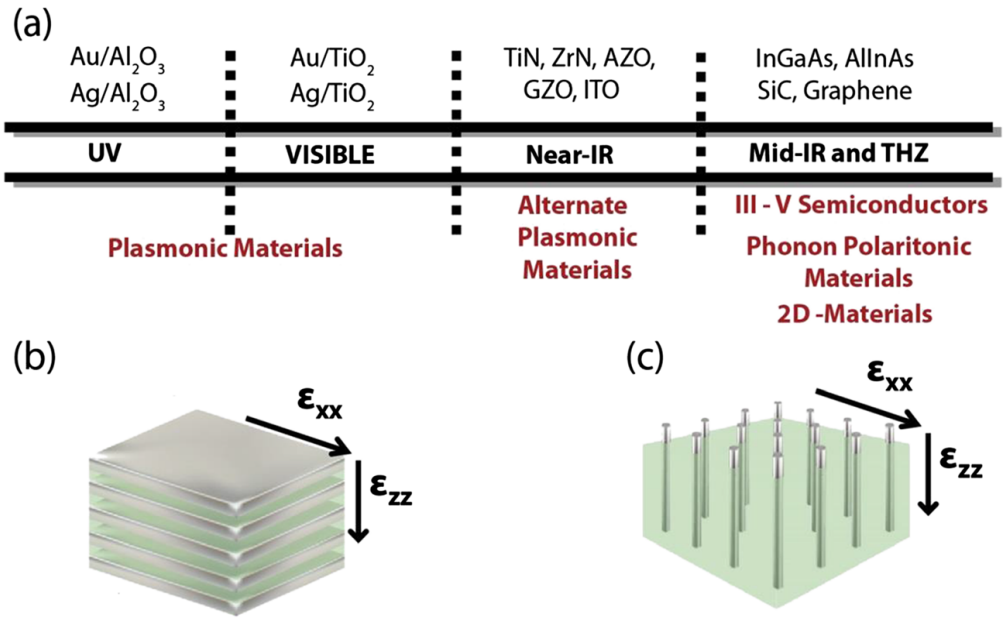

FIGURE 3.7: Fabrication of hyperbolic metamaterials: (a) Materials used to create HMM depending on region of operation in the electromagnetic spectrum (UV to mid-IR and THZ frequencies). (b) Multilayer structure consisting of alternating metallic and dielectric layers forming a metal-dielectric superlattice. (c) Nanowire structure consisting of metallic nanorods embedded in a dielectric host [56].

metamaterials is layered metal–dielectric structures. There is also another approach to fabricate hyperbolic metamaterials using metallic nanowires in a dielectric host. However, the problem of silver overfilling or discontinious islands with the pores makes nanowire HMM fabrication quite challenging.

Figure 3.7(a) describes about a wide available plasmonic metals and high index dielectrics in order to fabricate hyperbolic metamaterials. Either gold or silver as alternating multilayers with alumina form HMMs in the ultraviolet regime. To observe hyrperbolic behavior in the visible range, high index dielectric such as TiO_2 or SiN is required [58]. While, alternate plasmonic materials based on transition metal nitrides or transparent conducting oxides for hyperbolic media are the promising candidates for near-infrared (IR) wavelengths [59]. For mid infrared region, III-V degenerately doped semiconductors have been used in place of metallic components in HMMs. Noteworthy, SiC function as metallic building block due to narrow reststrahlen band for hyperbolic media [60]. Multilayer graphene super-lattices are also capable to show hyperbolic metamaterial response in the THz (far-IR) region. Figures 3.7(b) and (c) demonstrates the sketch of fabricated Type II and Type I HMMs, using ultra subwavelength thin metal-dielectric metal layers and nanorods embedded in dielectric host.

3.7.5 Origin of the high-k modes in HMMs

In designed HMMs, due to the metallic building block required to achieve a negative dielectric constant in one direction, HMMs support bulk plasmon-polaritonic or phonon-polaritonic modes. Thus high-k modes of HMM can be considered as engineered bulk polaritonic modes which owe their large momentum to light-matter coupling. When evanescent wave is incident on a conventional dielectric as opposed to hyperbolic metamaterial. The evanescent wave decays in a simple dielectric but couples to a high-k propagating wave in the hyperbolic metamaterial [61]. The high-k mode is seen to arise due to the coupling between the surface-plasmon-polaritons on each of the interfaces. Thus the high-k modes are in fact the bloch modes due to the coupled surface plasmon polaritons on the metal-dielectric multilayer superlattice [62].

Chapter 4

Gain-Plasmon Coupling: Energy Transfer Processes Towards Absorptive Loss Mitigation

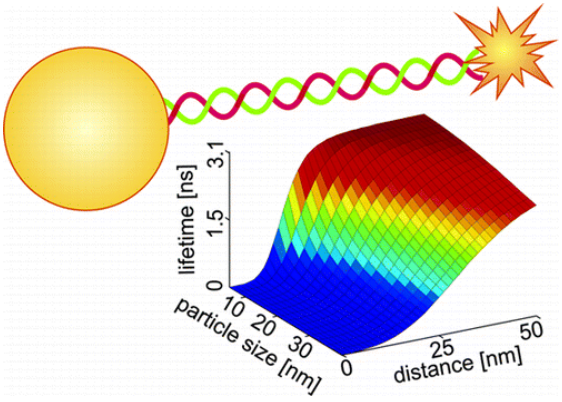

4.1 Gain Materials

Gain materials, which can also be named chromophores, absorb the photons of incident excitation electromagnetic wave and emit photons at longer wavelength in the visible spectrum. Such materials have been found applicable in the field of biosensors, solar cells, LEDs and diode lasers. Gain materials can be categorized into two classes such as fluorophores and semiconductor quantum dots. Before discussing the optical properties of fluorophores and QDs, it is necessary to review the occurred processes on the excitation of chromophores.

4.1.1 Jablonski Diagrams

A Polish professor named Alexander Jablonski devoted his life to the study of molecular absorbance and emission of light. He explained and sketched all the processes in the schematics, which are known as *Jablonski Diagrams* [63]. An excited chromophore molecule can be relaxed to the ground state following two types of transitions. Fluorescence and phosphorescence take place if transition to ground state is spin allowed and spin forbidden, respectively. Energy levels of chromophore and its relaxation process via radiative and nonradiative channels have been illustrated by the Jablonski diagrams [64]. In figure 4.1, singlet states are referred by S and triplet by T. Radiative processes

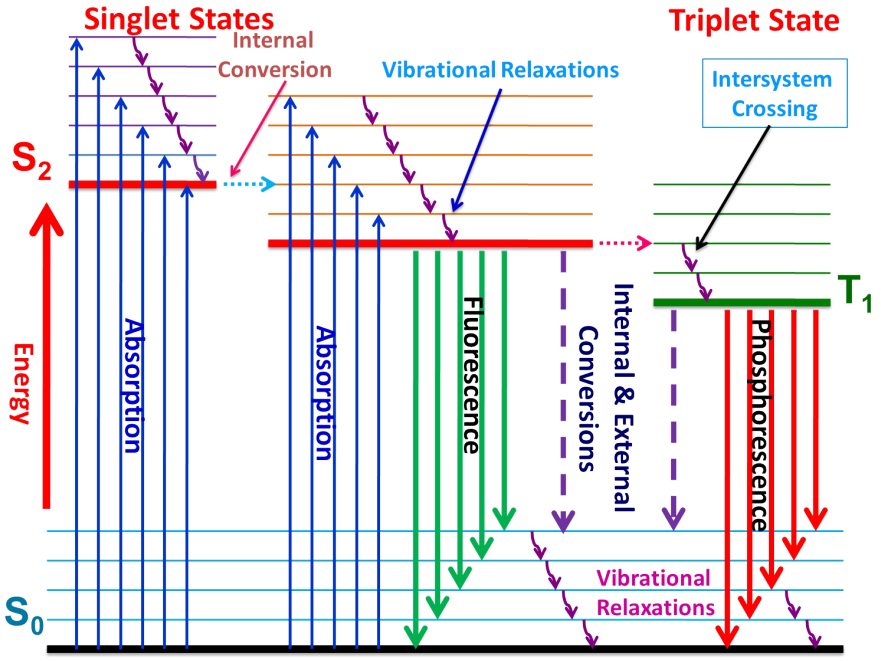

FIGURE 4.1: Jablonski diagram representing various radiative and non-radiative relaxations of a chromophore molecule along with fluorescence and phosphorescence.

like fluorescence and phosphorescence have been indicated by sinusoidal arrows.

Absorption takes place when fluorophore molecule absorbs a photon with energy equal or greater than the energy difference between the ground and excited state as shown in figure 4.1. Molecules approach to excited states when exposed to light of a wavelength (energy level) equal to the energy gap between the ground state and excited state. This process is called molecular absorbance of light. The amount of light absorbed is proportional to the concentration of the absorbing molecule. Lambert-Beers law calculates

absorbance A such as

$$A = \log_{10}\left(\frac{I_0}{I}\right) = \varepsilon_{abs} cl \tag{4.1}$$

where A is the absorbance and I_0 and I refer to the intensity of incident and transmitted light, ε_{abs} and c are the molar absorptivity and the concentration of fluorophores, respectively, while l is the effective thickness of used cuvette in cm. On the other hand , photons with lower energies are not allowed to higher energy states and will be transmitted [65].

Fluorescence process occurs as an outcome of light absorption by fluorophore. Incident light energy promotes the electrons from occupied orbitals to unoccupied ones, leaving the molecules into excited states. Excited electrons release their energy to the lowest level of singlet by vibrational relaxations and internal conversion in the case of populating higher excited singlets (S_2). Relaxation through emission of light in principle always occur from the lowest energy excited electronic state of a molecule (S_1). In this case, electron spends 10^{-8}s in the S_1 excited state and de-excites to the ground state S_0 within 10^{-15}s. The mechanism of the radiative relaxation named as fluorescence (green lines transition) can be understood from the figure 4.1. Moreover, there is a loss of energy through light emission due to another present radiative channels like vibrational relaxations and internal conversion. Fluorescence emission is always red shifted (towards longer wavelengths) relative to the excitation wavelength of light. The difference between excitation and emission wavelength is known as Stokes shift, demonstrating energy losses.

Internal and external Conversion are non radiative processes which take place during the transition from excited state to ground state and lead towards the conversion of all the excitation energy into heat. Internal conversion occurs due to direct vibrational coupling and quantum mechanical tunneling between the ground and excited electronic states. On the other hand, external conversion occurs due to collisions of excited molecules in higher energy states [63].

Phosphorescence involves a radiative transition from triplet state to the singlet ground state. Triplet states have longer life time and are located at lower energy levels with respect to excited singlet states which results in the appearance of phosphorescence as a very slow process in the time range from 10^{-3}s to few seconds (even sometime to few minutes too) at higher wavelength with respect to fluorescence emission. Such types of transitions are classically forbidden [66].

4.1.2 Parameters affecting fluorescence emission

Local environment effects

Fluorescence emission strictly depends on the surrounding local environment of a fluorophore. Parameters like pH value, temperature, concentration and polarity affect the emission of gain materials. The polarity of the solvent causes a shift in the emission. When the molecule is excited, the dipole moment is higher than in the ground state. In a highly polar environment a "solvent" relaxation will occur, making the dipole moment between ground state and excited state smaller, and thus a lower energy difference between the two states. This will lead to a shorter emission wavelength (a blue shift) compared to the same molecule in a non polar environment. This is relevant when measuring a fluorophore in different solvents, but also when measuring macro molecules such as proteins that can contain several fluorescing groups functionalized at different groups [67].

Concentration effect

fluorescence intensity also depends on the concentration of the fluorophore, but also from other absorbing substances in the sample. At low concentrations, the relation between concentration and intensity known from Lambert-Beers law is also valid for fluorescence emission, while it can be affected by concentration quenching at high concentrations. Fraction of the excitation and/or emitted light is reabsorbed by the sample and the measured intensity of the fluorescence is thus decreased (quenched). In high concentration samples, the linear relation between concentration and fluorescence intensity is no longer valid which means Lambert-Beers law is not followed any more. Concentration quenching can be lowered by reducing the absorbance in the sample by either diluting the sample or by reducing the pathway (decreasing the thickness of the cuvette) [68].

4.1.3 Gain media : Organic dyes and Quantum dots

As it is already described, gain media can be classified into organic dyes and quantum dots (QDs) and are capable to emit light in visible range. Organic dyes are the most used chemical compounds for energy transfer processes due to large stock shift, higher quantum yield and the invention of easy chemical methods to functionalize dye molecules with plasmonic structures. However organic dyes also exhibit few shortcomings like low chemical, photo bleaching and optical stability.

On the other hand, QDs efficiently fulfills all the drawbacks of organic dyes. Basically, QDs are fluorescent semiconductors with extra-ordinary optical properties. They have unique photo-physical properties like size-tunable light emission, improved signal brightness, resistance against photobleaching, and simultaneous excitation of multiple fluorescence colors. Furthermore, QDs are useful in a variety of in vitro and in vivo applications. QDs can be used to target cell biomarkers because of high luminescence and stability. Thus, QDs have the ability to become a novel class of fluorescent probes [69]. The following example displays the superiority of QDs over Organic dyes. Figure

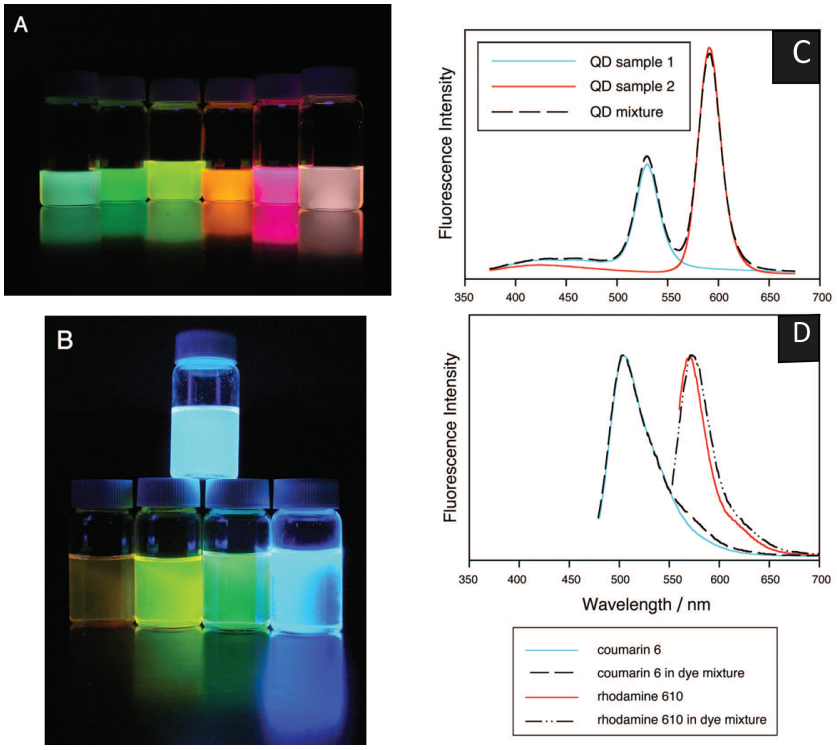

FIGURE 4.2: (A) Series of CdSe QDs prepared in this experiment (5vials on left) and a mixture of these components illuminated with a black light, (B) a series of dyes (rhodamine 610, rhodamine 590, coumarin 6, and coumarin 460) and a mixture of the dyes (top) illuminated with the same black light, (C) Fluorescence emission spectra of two different mixtures: QDs mixture containing two sizes of QD, excited at 350 nm and (D) a mixture of coumarin 6 and rhodamine 610 which were excited at 469 nm and 543 nm, respectively [70].

4.2(A) shows the emission of solution of QDs at different sizes and mixture of these QDs. Solutions of mixtures of emit colors are the sum of the fluorescence wavelengths of the individual QD components. When mixed in the appropriate relative quantities some QD mixtures emit nearly white light. On the other hand, when organic dyes are mixed, the black light excites only a single species and only one emission color is observed as shown in figure 4.2(B). In order to understand this phenomenon, the fluorescence emission of the mixture samples of QDs and organic dyes have been acquired with

respect to their individual ones as shown in figure 4.2(C) and (D), respectively. These results and observations demonstrate that mixtures of QDs uniquely possess emission colors that are the sum the individual QD components so that even white light can be produced from simple mixtures. While, the fluorescence emission spectrum of a binary mixture of organic dyes (rhodamine 610 and coumarin 6), as shown in shown in figure 4.2 (D) contains only one dominant peak which depends on wavelength rather than the components in solution [70].

4.2 Förster Resonance Energy Transfer : Exciton-Exciton Coupling

Electromagnetic induced electronic excitation of gain materials in the close proximity of an emissive or non emissive quenchers leads to energy transfer from excited active molecules to another entity either followed by a photon emission (Radiative reabsorption), non-radiative channels (Förster type), or electron-exchange (Dexter type). In order to understand the energy transfer processes, it is convenient to initiate with *FRET*, which is the most basic transfer process between a pair of gain molecules (dyes, QDs or combination of both). This can be considered as the principle near field interaction process and another energy transfer mechanisms among the more complex entities can also be explained on the basis of FRET process. Theoretical results confirm the

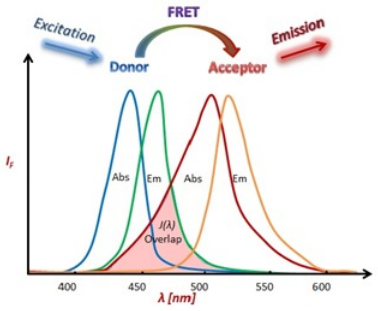

FIGURE 4.3: Absorption and fluorescence spectra of an ideal donor-acceptor pair. Light pink colored region is the spectral overlap between the fluorescence spectrum of donor and absorption spectrum of acceptor.

presence of a near field communication between the two excited gain molecules, if such molecules are located in few nanometer range with respect to each other and considered as an oscillating dipoles [63]. Close proximity enables an exciton-exciton coupling and the mechanism of such coupling has been explained by German scientist Theodor

Förster, so, this phenomenon was named as Förster Resonance Energy Transfer in his honor.

FRET is a radiationless dipole-dipole interaction between two excited gain molecules which takes place when an initially excited gain molecule relaxes to the ground state by transferring its energy to a nearby molecule in a nonradiative way [71]. FRET can occur between a pair of gain molecules such as QD-QD, QD-dye and dye-dye pairs. Such pairs can also be seen as donor-acceptor pair.

Figure 4.3 shows the spectral overlapping (defined by $J(\lambda)$) between the emission of donor and absorption of acceptor, which is a necessary condition for any energy transfer processes. Noteworthy, FRET only requires the donor to be fluorescent, not to the acceptor. FRET process has been explained by modified Jablonski diagram as shown in

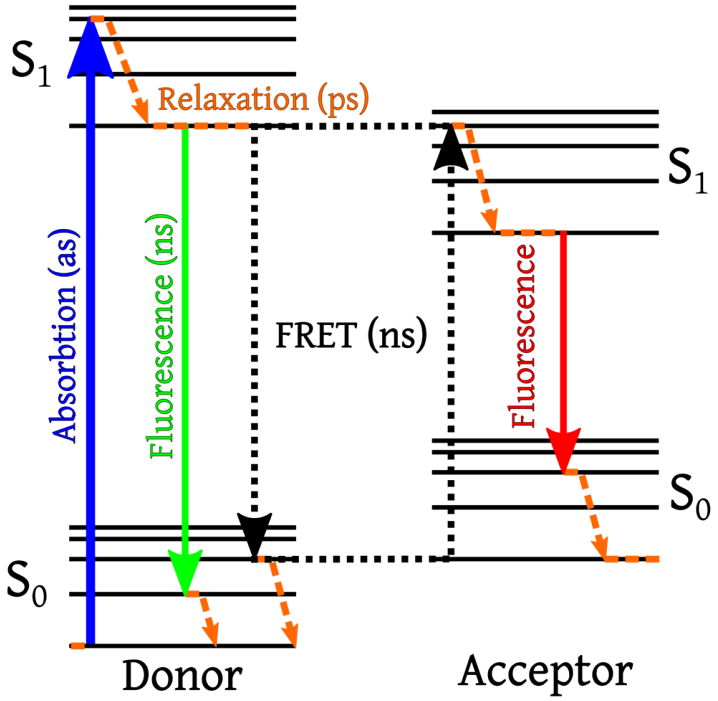

FIGURE 4.4: Jablonski diagramdemonstrates fluorescence resonance energy transfer (FRET) among donor and acceptor molecules. S_1 and S_0 are the excited and ground singlet states, respectively.

figure 4.4 demonstrating an additional relaxation channel for excited donor molecules. Donor molecules approach to the higher energy states, when excited by external source. The mechanism of FRET involves a donor fluorophore in an excited electronic state, which may transfer its excitation energy to a nearby acceptor chromophore in a non-radiative fashion through long-range dipole-dipole interactions. The theory supporting energy transfer is based on the concept of treating an excited fluorophore as an oscillating dipole that can undergo an energy exchange with a second dipole having a

similar resonance frequency. In this regard, resonance energy transfer is analogous to the behavior of coupled oscillators, such as a pair of tuning forks vibrating at the same frequency. Such non-radiative energy transfer can be confirmed experimentally by observing decrease in the donors fluorescence intensity and shortening in its excited lifetime.

When donor as well as acceptor molecules are fluoroscent, energy transfer processes are named as fluorescence resonance energy transfer. FRET typically takes place among donor and acceptor molecules within the seperation distance of 0.5 nm to 10 nm.

4.2.1 Factors affecting FRET

Rate of FRET depends upon the extent of spectral overlap ($J(\lambda)$) between the donor and acceptor pair as shown in figure 4.3, the quantum yield of the donor, the relative orientation of the donor-acceptor transition dipole moments and the distance separating the donor-acceptor molecules. Any event or process that affects the distance between the donor-acceptor pair will affect the FRET rate.

Moreover, Förster calculated that the efficiency of the FRET process (E_{FRET}) depends on the inverse sixth power of the distance between the donor and acceptor pair (r) and is formulated by

$$E_{FRET} = \frac{R_0^6}{R_0^6 + r^6} \tag{4.2}$$

Where R_0 is the Förster radius at which half of the excitation energy of donor is transferred to the acceptor chromophore. Therefore Förster radius R_0 is referred to as the distance at which the efficiency of energy transfer is 50%. The Förster radius (R_0) depends on the fluorescence quantum yield (*defined as the ratio of the number of luminescent molecules to the total number of excited molecules*) of the donor in the absence of acceptor, the refractive index of the solution, the dipole angular orientation of each molecule and the spectral overlap integral of the donor-acceptor pair [71].

4.2.2 Application of Fluorescence Resonance Energy Transfer (FRET)

Due to strong distance-dependence nature, FRET efficiency has been widely utilized in studying the structure and dynamics of proteins and nucleic acids, in the detection

and visualization of intermolecular association and in the development of intermolecular binding assays [72, 73]. Thus, such energy transfer rates have found applications as *spectroscopic ruler*. The distance over which energy can be transferred is dependent on the spectral characteristics of the fluorophores, which is generally in the range of 0.5 nm to 10 nm. Thus, if fluorophores can be attached to known sites within molecules, measurement of the efficiency of energy transfer provides an ideal probe of inter- or intramolecular distances over macromolecular length scales. Indeed, fluorophores used for this purpose are often called *Probes*. FRET has been used for measuring the structure, conformational changes and interactions between molecules and as a powerful indicator of biochemical events [74]. Although the challenges of labeling molecules with fluorophores and making accurate measurements of the fluorescence emitted by them are being overcome, but, a number of difficulties still remain when examining real-life systems.

4.3 Gain-Plasmon Energy Transfer process : Exciton-Plasmon Coupling

Successful implementation of FRET towards various innovative applications, as described in above section sparks curiosity to study the interaction of a gain molecule and a plasmonic nanostructures, when placed in close proximity. Such interaction leads to the coupling of electric dipoles of gain materials and plasmon modes of metallic nanostructures. Theoretical and experimental studies confirm that cross talk between resonant dipoles of active molecules and plasmon modes of NPs triggers non-radiative energy transfer process from gain material to absorptive NPs, following certain conditions [75–78]. Before going in detail on gain-plasmon energy transfer process (GPET), it is important to discuss such conditions, which play very important role in the transfer processes.

4.3.1 Necessary conditions for exciton-plasmon coupling

(A) Spectral overlapping between donor and acceptor

An appropriate spectral overlapping between donor molecule emission and acceptor absorption spectrum is one of the most important condition in order to achieve efficient RET process. Figure 4.5 represents an example of proper spectral overlap between the

emission spectra of donor coumarin 520 molecules (red line) with plasmon band of 45 nm gold core- silica shell ($Au@SiO_2$) NPs (black line). Spectral overlapping al-

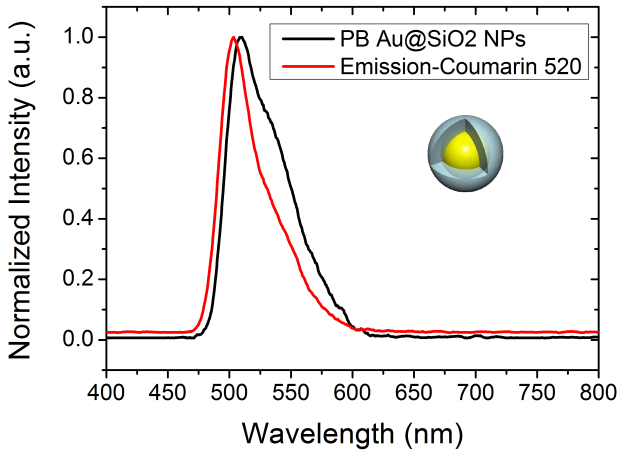

FIGURE 4.5: An example of perfect overlaping between the emission spectrum of coumarin and plasmon band of core-shell NPs.

lows us the inter-band transitions via dipole-dipole interactions of donor and acceptor in FRET. On the other hand GPET opens up an extra channel of energy transfer process due to strong coupling between plasmon modes NPs and dipoles of the excited donor molecule, resulting in a significant donor emission quenching.

(B) Gain to plasmon seperation dependence

It is well known that plasmonic NPs are considered efficient quencher of emission in comparison to acceptor fluorophore in FRET. Thus, GPET can take place in the long range within 1 to 40 nm with respect to donor-acceptor seperation distance (1 to 10 nm) in FRET [79]. Energy transfer rate from a chromophore to a small NP via *Nanoparticle surface energy transfer* process follows R^{-4} distance dependence, while for dipole-dipole interactions, such dependence varies to R^{-6} [71]. Therefore, energy transfer rate from gain molecule towards a NP must lie in the middle between these two extreme cases, following R^{-n} distance dependence, where n is between 4 and 6 [80].

(C) Geometry and shape influence

Geometry and shape of the plasmonic system affects the spectral overlapping plasmon band with emission spectrum of gain materials simply and eventually, GPET process. For example, it has already been discussed that spherical NPs having size less than 2 nm, cannot support the surface plasmons and attain broader and weak absorption band. Such plasmonic NPs are not suitable for energy transfer processes due to less effective spectral overlaping.

(D) Dipole orientation dependence on gain-plasmon coupling

Dipole orientation of a chromophore molecule with respect to the induced dipole of NP controls the energy transfer rate whether is increased or decreased [81]. Due to symmetry of the spherical NPs, the orientation dependence in gain molecules-Au NPs is different with respect to a pair of dye-dye or dye-QD. If dipoles of two chromophores are oriented perpendicular to each other, which means θ=0° for one gain molecule and θ =90° foe second one leads no energy transfer between the two actors. On the other hand, when the chromophores dipoles are parallel to each other, the rate of energy transfer is either maximum for both dipoles at θ=0° or a quarter of maximum value of energy transfer rate, when both are mutually situated at 90° [80]. However, the energy transfer process in GPET takes place when gain molecule is rotated along the NP surface from the perpendicular to the parallel orientation which is a completely different way as compared to FRET mechanism. the ratio of the maximum energy transfer rate to minimum one approaches 4 at large separation distances and there is no orientation that forbids energy transfer like FRET. Interestingly, the orientation dependence becomes weaker at smaller distances [80, 82]. The relative dipole moment orientation of a chro-

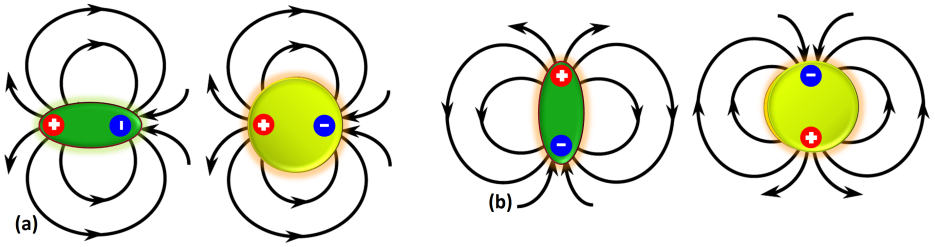

FIGURE 4.6: An example of perfect overlaping between the emission spectrum of coumarin and plasmon band of core-shell NPs.

mophore with respect to the induced dipole of NP determines whether the radiative rate is increased or decreased. Figure 4.6 represents schemes of the relative orientation of interacting dipole moments, resulting in modification of the radiative and non-radiative decay rates. Parallel orientation of chromophore dipole moment to the surface of the NP as shown in figure 4.6 (a) motivates dipoles of donor and plasmonic NPs to radiate out of phase, decreasing the net dipole moment of the system. Thus, destructive interference takes place which reduces radiative decay rate and enhances non-radiative rate [81]. Presence of enhanced non-radiative decay rate can be confirmed by observing fluorescence quenching, shortening of life time and decrease in quantum efficiency of donor.

While, if the chromophore transition dipole is orientated in perpendicular way toward NP surface as shown in figure 4.6 (b), total dipole moment is enhanced due to the constructive fields interferences of the chromophore dipole with plasmonic dipole [83].

This leads to the improvement of absorption rate, resulting in the enhancement of radiative rate. Noteworthy, non-radiative rate is even enhanced due to the energy transfer for radial polarization, But, radiative decay rate dominates leading towards enhanced fluorescence [84].

(D) Quantum Yield of donor molecules

Quantum efficiency of donor can influence the interparticle distance for obtaining an effective RET in a gain-plasmon composite. In fact, higher values of the quantum yield can improve the efficiency of GPET process even for longer gain-plasmon separation distances. If gain medium exhibiting low values of quantum yield has been selected for the energy transfer process, such material cannot exhibit an intensive fluorescence signal. Non-radiative relaxation pathways even in the absence of any quencher already dominate in such systems. In order to differentiate the opening of non-radiative channel due to gain-plasmon coupling, higher values of donor quantum yield must be preferred, whereas, gain medium with lower quantum yield must be used for metal enhanced fluorscence processes.

4.3.2 Mitigation of optical losses : description of energy transfer process via Jablonski diagram

In the frame work of all the above discussed conditions, Jablonski diagram has been used in order to explain the resonant energy transfer process from a fluorescent molecule towards a proximal plasmonic NP as shown in figure 4.7. Excitation energy sources promote chromophores molecules to excited state, which yields in population of fluorophore meta-stable state. Meanwhile, the plasmonic NP absorbs the incoming light, resulting in the enhancement of their plasmonic local fields and excitation of bipolar modes of NP.

It is well known that de-excitation process of fluorophores could be performed either by radiative channels so called spontaneous emission or by nonradiative channels. However, for a fluorophore placed in close vicinity of a metallic NP, nonradiative relaxing channels significantly enhance through RET process from chromophores to absorptive NPs. As a result of this process, intrinsic emission of fluorescent materials either QDs or organic dyes strongly can be quenched. Obviously, both parameters of fluorescence lifetime and quantum yield of donor molecules will be modified, as well. The new

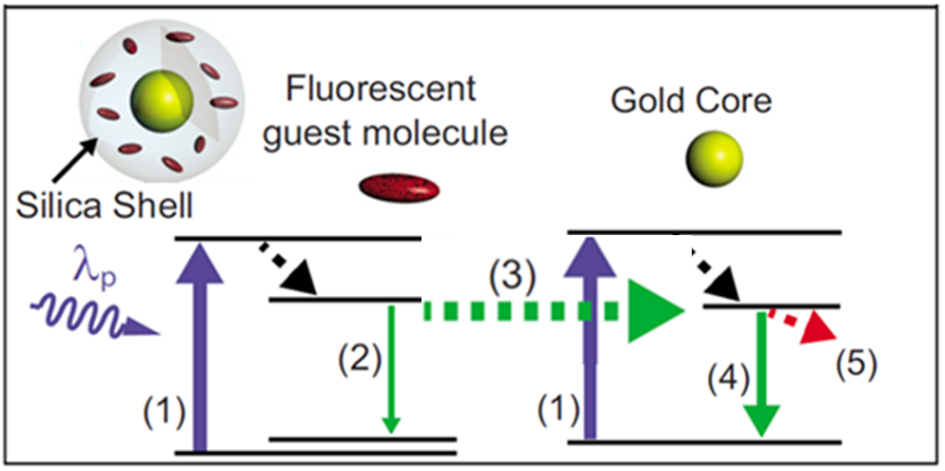

FIGURE 4.7: Jablonski diagram, sketching gain-plasmon energy trasnfer processes in gain functionalized core-shell NPs.

lifetime of donor molecule is expressed by

$$\tau_{DA} = \frac{1}{k_r + k_{nr0} + k_{GPET}} \tag{4.3}$$

where $k_r$is the quenched donor emission. Also, the term k_{GPET} represents the presence of nonradiative energy transfer from donors to plasmonic acceptors. The sum of energy transfer rate with k_{nr_0} denotes total non-rative decay rate of a single fluorescent molecule (k_{nr}) in the presence of metal acceptor. Take it into account that the enhancement of non-radiative rate is outweighed respect to dropping of radiative rate. Hence, radiative lifetime of the donor is shortened. Respect to the relation of quantum yield with lifetime and radiative rate, we can write,

$$\phi_{DA} = \frac{k_r}{k_r + k_{nr_0} + k_{GPET}} = \tau_{DA} \times k_r \tag{4.4}$$

Since, both terms of k_r and ϕ_{DA} have been decreased, the reduction of gain material quantum yield is expected. Briefly, the non-radiative relaxations term (represented by green dashed arrow) has been demonstrated in figure 4.7 which includes thermal energy dissipation (electron-phonon coupling) and plasmonic state relaxation of excited electrons. One can confirm the significant presence of non radiative channel by observing the simulateneous reduction of donor quantum yield, radiative rate and lifetime of domor molecules.

Noteworthy, nonradiative energy transfer from gain molecules to plasmonic NPs is not only as an additional pathway for releasing the energy of excited gain molecules, but involves collective excitation (plasmons) of compressible electron gas in the nanoparticle.

This interesting process has been exploited to mitigate the absorptive loss of plasmonic systems. In fact, the absorptive losses could be compensated with inclusion of sufficient active gain media, able to transfer energy on propagating SPPs and localized SPRs in metal nanostructures using stimulated emission. In this respect, several theoretical and experimental studies have demonstrated how nonradiative RET process from gain materials to plasmonic nanostructures can mitigate NPs absorptive losses [85–90]. Thus, the transferred energy from donor on absorptive NPs does not dissipate completely thermally through electron-phonon coupling, but also it can be relevant for decreasing the radiation damping of NPs in terms of reduction of the imaginary part of the dielectric permittivity.

As it has already been described in previous chapter, negative permittivity of plasmonic NPs in visible range which makes them as a promising alternative for constructing the subunits of optical metamaterials, originates from absorptive nature of metallic NPs. Hence the intention of introducing gain to plasmonic NPs is not completely eliminating the absorptive behavior of NP. However, it should be moderated sufficiently to make NPs enough appropriate for optical applications. Indeed, transferring the energy is the cost that we must pay to reduce the optical loss of NPs, but also keep alive their plasmonic resonances.

Chapter 5

Exciton-Plasmon Coupling in Nanoscaled Systems

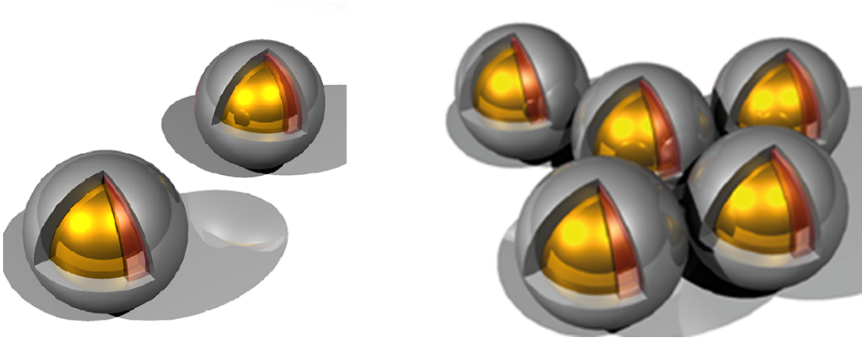

5.1 Introduction

In the past decade, plasmonic nanostructures have attracted great interest because of their extraordinary and promising physical properties, assuming an important role in emerging science and technological applications. In particular, the wide cross-disciplinary features of plasmonics are being recognized in new research fields, leading to interesting fundamental insights and promising applications in materials science, biology and medicine. It is also well known from the section 2.4 that the particular optical properties of noble metal nanoparticles (NPs) are attributed to the localized surface plasmon resonance (LSPR), which is the collective coherent oscillation of free electrons

(with respect to the positive ionic background) on the metal surface in resonance with the electric component of an incident electromagnetic wave. LSPR contributes to the strong confinement of optical radiation and a large enhancement of the electromagnetic field in their proximity. Current research efforts in nanoplasmonics have led to various photonics, opto-electronic and biomedical applications such as single-particle detection and biomolecular recognition, optical probes for high resolution imaging, photo-thermal therapies, photovoltaics, Raman biosensing, colorimetric sensing, hyper-lenses, and optical metamaterials [6, 19, 25, 91, 92]. Negative values of the real part and low values of the imaginary part of the dielectric permittivity are key factors for plasmonic applications. However, plasmonic NPs are not ideal resonators and exhibit considerable optical losses at visible wavelengths that are undesirable for most of their potential applications.

In this respect, some theoretical and experimental studies have demonstrated how non-radiative resonant energy transfer (RET) processes may play a role in modifying the imaginary part of the effective dielectric function of the hybrid systems [85, 88, 90, 93, 94]. As it is already explained in previous chapter, non-radiative energy transfer efficiency in hybrid (plasmon–exciton) systems strongly depends on physical parameters such as geometry and size of the metal nanostructures, inter-particle distance, relative spectral position between the excitonic band and surface plasmon band (SPB) of metal NPs, relative orientation of the chromophore's transition dipole moment with respect to the NP's plasmon modes, strength of the transition dipole moment and ntration and molar extinction coefficient of the plasmonic and excitonic particles.

Moreover, Bo Peng et al. have reported that the incorporation of gain material at a controlled distance from gold NPs allows for control and optimization of RET mechanisms [18, 88]. In our former studies, we have investigated the influence of incorporating excitonic material (chromophores) in the high-local-field areas of plasmon nanostructures to induce coherent RET processes from chromophores (donors) to plasmon nanoentities (acceptors), both in gain assisted (NP– dye dispersions) and gain-functionalized (dye encapsulated into the silica shell) systems [90, 95, 96]. The present work in this chapter represents a nanoscale approach to ethanol based multimers dispersed (mixture of monomers, dimers, trimers, quadrimers, etc.) nanostructures consisting of gold-core/silica spacer/silica shell, in which chromophores (Rhodamine B) have been grafted at the interface between the silica spacer and the protective external shell. By varying the intermediate silica shell thickness from 10 to 30 nm, two series of multimeric nanostructures have been synthesized and dissolved in ethanol solutions: passive (without chromophores) and active ones (functionalized with chromophores). In addition,

corresponding passive and active single NPs (monomers) have been synthesized and used as control samples. Steady-state fluorescence spectroscopy accompanied by ultrafast time resolved spectroscopy shows a stronger coherent coupling between the plasmonic cores and embedded excitonic molecules in multimers as compared to the similar monomers. Moreover, Rayleigh scattering measurements and transient absorption spectroscopy, performed on these two sets of samples, show a stronger plasmon–exciton coupling in multimeric nanostructures with respect to single nanoparticles (monomers), revealing a stronger optical loss mitigation in the case of multimeric nanostructures. Simulation results demonstrate the occurrence of an enhanced local field in multimers with respect to the corresponding monomers which can be understood within the context of plasmon hybridization theory in multimeric nanostructures [48, 97, 98]. In addition, it was investigated that a shorter separation distance between NPs and dye molecules lead to more efficient non-radiative RET processes, which results in further absorptive losses mitigation. Eventually, these results confirm that GPRET process occurs at separation distances longer than those occurring for Förster resonant energy transfer process (FRET) [71, 99].

5.2 Synthesis of monomers and multimers

Gold NPs with a diameter of (60$\pm$ 5) nm were synthesized through the reduction of hydrogen tetrachloroaurate(III) ($HAuCl_4$) in the presence of sodium citrate ($Na_3C_6H_5O_7 \cdot 2H_2O$) and sodium borohydride ($NaBH_4$) according to the procedure published by Brown et al. [100]. Firstly, passive gold nanoparticles (without dye) were coated with a silica shell (monomer) according to the procedure published by Graf et al. [101] . The thickness of the shell was controlled by changing the amount of silica precursor (tetraethyl orthosilicate, TEOS). Active nanoparticles (with dye) have been obtained from the passive ones by firstly grafting a Rhodamine B derivative with ethoxy-silano group, which was previously prepared by reacting Rhodamine B isothiocyanate (RhB) with aminopropyltriethoxysilane in absolute ethanol on the silica shell. To do so, an amount corresponding to 15 RhB molecules per nm of silica surface was added into an ammonia (6 % v/v)/ethanol suspension of passive particles. The reactive medium was heated at 70°C during one hour. The monomers were collected by centrifugation and washed three times with absolute ethanol. A second protective silica shell of 10 nm thickness was then grown by drop wise addition of an ethanolic solution of TEOS. The increase of the concentration of passive and active monomers during the addition of

the TEOS solution leads to the formation of multimers which are a mixture of dimers, trimers, quadrimers, heptamers, etc. These multimers are formed as a result of collisions between monomer particles and are permanently fixed via the hydrolysis and condensation of TEOS molecules on their surface. Synthesized multimers were filtered via ultra- filtration membranes to separate monomers from multimers. However, filtrating all monomers is not experimentally achievable.

5.3 Structural characterisation of plasmonic monomers and multimers

Following the above synthetic procedure, two categories of multi-silica shell NPs have been investigated such as active and passive multimeric and monomeric nanostructures (control samples). Passive NPs consist of ethanol solutions of gold-cores (60 nm in diameter), coated with silica shells 10 and 30 nm thick, labeled as Mo10 and Mo30, respectively. Correspondingly active NPs, namely Mo+10 and Mo+30, have been synthesized by starting from the Mo10 and Mo30 samples, then grafting Rhodamine B isothiocyanate (RhB) dye molecules onto the spacer silica shell via click chemistry. Finally, a second 10 nm protective silica shell has been used to cover all the samples and protect the RhB molecules on the Mo+10 and Mo+30 samples.

At the same time, multimeric samples have also been produced by selecting monomers, dimers, trimers, quadrimers, heptamers, etc., of both passive and active monomers with 10 and 30 nm plasmon–chromophore separation distances. Active multimers (main samples) and the corresponding passive ones (control samples) have been labeled as Mu+10, Mu+30 and Mu10, Mu30, respectively. A sketch of the multimeric system is presented in figure 5.1(a). Average size uniformity is obtained by statistical analysis of the core diameter, as shown in figure 5.1(b). The monodispersity of the active monomeric samples (Mo+10) and the uniformity in size and shape of both systems have been investigated by means of transmission electron microscopy (TEM) as shown in figure 5.1(c). While the formation of multimers (Mu+10) can be clearly seen in figure 5.1(d).

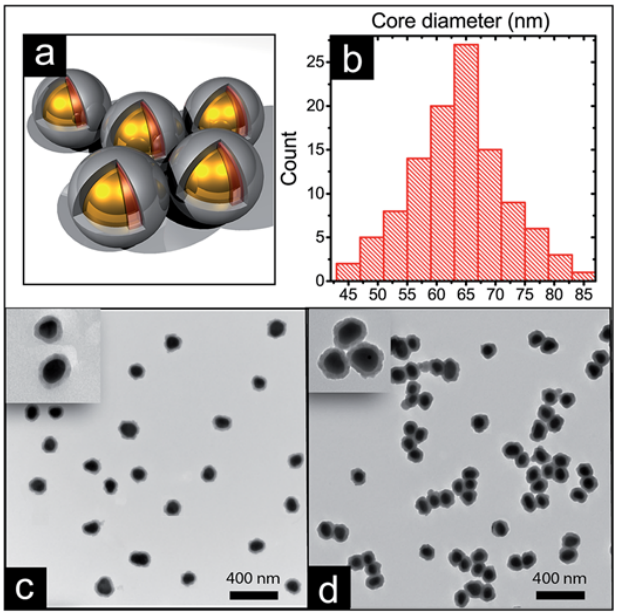

FIGURE 5.1: (a) Sketch of the active multimers, (b) statistical analysis of core diameters performed on the Mu+10 system. TEM images of the (c) Mo+10 monomers and (d) Mu+10 multimers with core diameter of 60 nm, silica spacer of 10 nm and silica protective shell of 10 nm.

5.4 Red shift in extinction curves of multimers

The extinction cross-section spectra of both systems have been measured by means of an UV-visible spectrophotometer (Cary500 by Varian). Figure 5.2 (a) and (b) show the normalized extinction cross-section profiles of both passive and active monomers and multimers, respectively. It is well known that the plasmon response of the nanostructures can be influenced by the thickness of the silica shell, refractive index of the surrounding environment and configuration of the nanostructures [102]. In figure 5.2(a) and (b), SPBs show a slight red-shift for multimeric systems with respect to monomeric ones. The increase of the local field intensity due to coherent plasmon–plasmon interactions leading to hybridization processes can result in a more efficient scattering cross-section of multimers accompanied by a significant red-shift with respect to the absorption efficiency spectrum [48, 97]. Noteworthy is the increase of the red-shift in extinction curves for multimers with respect to monomers for a shorter gold core–fluorophores separation (10 nm) as compared to thicker separation layered samples.

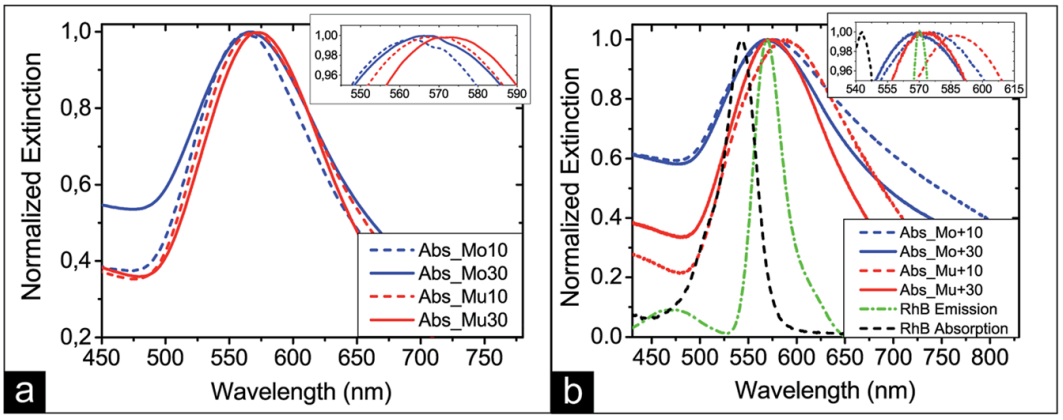

FIGURE 5.2: Normalized extinction spectra of (a) passive and (b) active monomers and multimers, including absorption ($\lambda_{abs,max}$ = 543 nm) and emission ($\lambda_{abs,max}$ = 570 nm) spectra of RhB dye molecules all dispersed in ethanol. The insets of (a) and (b) precisely show the red-shift of the multimers' plasmon bands with respect to that of the corresponding monomers.

5.5 Fluorescence quenching in multimers

Steady-state fluorescence measurements have been performed on the investigated systems. As evidenced in figure 5.3, the emission spectral position of encapsulated RhB in NPs shows a significant change with respect to the same molecules dispersed in solution (green dashed dotted line figure 5.2 (b). In fact, the surrounding environment and probable formation of dye aggregates during the grafting process can modify the absorption and emission curves [103]. Moreover, excited dye molecules exposed to intense plasmonic fields may undergo radiative decay from energy levels triggered by plasmon modes. Steady-state photoluminescence (PL) studies show that the fluorescence peak corresponding to multimers is red-shifted with respect to the monomers as shown in figure 5.3 (a) and (b).

This effect appears more significant in the Mu+10 sample (thinner silica spacer) as compared to Mu+30, corroborating our hypothesis that strong plasmon fields can trigger radiative resonance with the plasmon modes, that are expected to be at longer wavelength for Mu+10. Fluorescence quenching effects can be observed because of resonant non-radiative energy transfer processes between excited fluorophores and plasmon nanostructures. Fluorescence quenching of RhB dye molecules in both multimeric systems have been observed. Emission spectra of gain molecules grafted in the Mu+10 sample show a 2.8 fold intensity reduction compared with Mo+10 as shown in figure 5.3 (a) whereas, figure 5.3 (b) only shows 1.5 fold quenching in the case of Mu+30 system with respect to Mo+30 one. The obtained results demonstrate that the fluorescence quenching process is more efficient in multimers with a thinner spacer, because

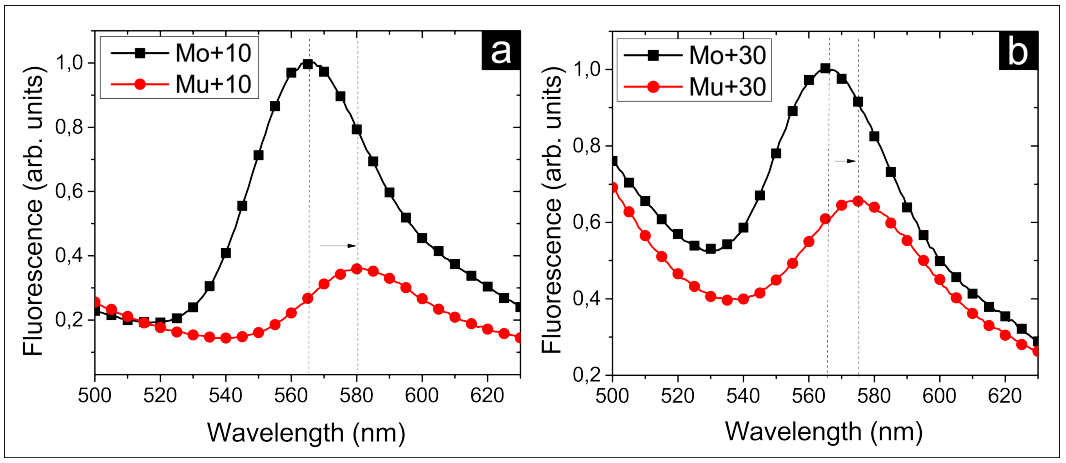

FIGURE 5.3: Fluorescence quenching observed in multimers as compared to monomers under the same pump energy value. (a) Fluorescence emission maxima of the Mo+10 sample (black squares) with respect to the Mu+10 sample (red circles). (b) Fluorescence emission maxima of the Mo+30 sample (black squares) with respect to the Mu+30 sample (red circles.

of the more effective GPRET process in cases when the excitonic molecules are placed in close proximity to plasmonic NPs.

5.5.1 Steady-state fluorescence set-up

Steady-state emission spectra were recorded on a HORIBA Jobin-Yvon Fluorolog-3 FL3-211 spectrometer equipped with a 450 W Xenon arc lamp, double grating excitation and single-grating emission monochromators (2.1 nm mm^{-1} dispersion, 1200 grooves per mm), and a Hamamatsu R928 photomultiplier tube. Emission and excitation spectra were corrected for source intensity (lamp and grating) and emission spectral response (detector and grating) by standard correction curves.

5.6 Time resolved spectroscopy on multimers and monomers

In order to understand the gain-plasmon coupling in gain functionalized monomers and multimers, time resolved spectroscopy have been performed on the all set of the samples. First, the used experimental set-up for time resolved spectroscopy has been described and then the obtained results have been discussed.

5.6.1 Ultrafast time-resolved fluorescence spectroscopy set-up

Fluorescence time decay of the samples have been acquired by means of an advanced spectro-fluorometer (Edinburgh, FLS 980 Series) using the TCSPC data option. The used system, an ultrafast time-resolved fluorescence spectroscopic instrument is equipped by Ti:Sapphire pulsed laser as a tunable excitation source in the 680–1080 nm range (repetition rate = 80 MHz, pulse width = 140 fs, by Coherent Inc.), and represents the core of a customized set-up that presents a pulse picker used to decrease the repetition rate in the range between 1 to 5 MHz, in order to be synchronized with a multi pronged spectrofluorometer able to perform both steady state measurements and TCSPC investigations as shown in figure 5.4. The excitation laser source can be tuned in order to excite the gain meolecules at particular wavelength and to perform time-resolved measurements on the samples. A Second Harmonic Generation (SHG) module is used to

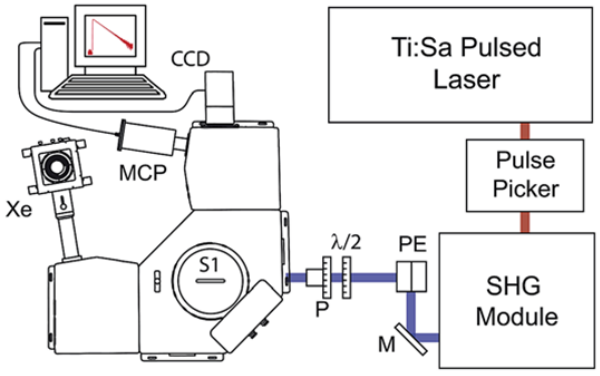

FIGURE 5.4: Scheme of the spectrofluorometer set up to perform ultrafast time-resolved fluorescence spectroscopy.

decrease the excitation wavelength in the range of 340–540 nm (blue beam). All the above mentioned investigations are performed inside the spectrofluorometer chamber (sample position S1). A multi channel plate, synchronized with incoming pulses is used to acquire the fluorescence decay lifetime in the proper temporal range. A broadband half wave plate ($\lambda/2$) and high damage threshold polarizer (P) are used to control the power of excitation pulses. The mounted periscope (PE) has been used to have an in-plane beam at a different heights. The photons collected at the detector are correlated by a time-to-amplitude converter (TAC) to the excitation pulse. Signals were collected by using a photon counting module, and data analysis was performed using the commercially available F900 software. The fit of data has been acquired by instrument software and quality of fit was assessed by minimizing the reduced χ^2 function and visual inspection of the weighted residuals.

5.6.2 Different life times observed in monomers and multimers

The fluorescence lifetime of all samples of monomers and multimers have been measured and compared with pure dye solution, using the above discussed set-up (see 5.4). Samples have been excited at excitation wavelength $\lambda_{exc} = 375nm$. The fluorescence time decay of dissolved RhB molecules was fitted by a single exponential function, while for both monomeric and multimeric systems, the time decay curves were fitted by using tri-exponential decay functions (green dots and blue line fit in figure 5.6). The fitting procedure of the emission intensity decays I(t) uses a tri-exponential model according to the following expression:

$$I(t) = \sum_{i=1}^{3} (\alpha_i exp(-t/\tau_i) \tag{5.1}$$

where τ_i are the decay times and α_i represent the amplitudes of components at t=0. The

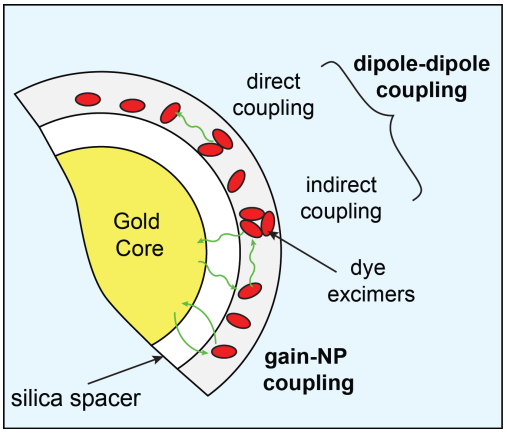

FIGURE 5.5: Sketch of different coupling configurations between grafted dye molecules and gold cores.

presence of a very fast decay time τ_1 is attributed to a significant enhancement of the nonradiative decay rate due to a strong GPRET process as sketched in figure 5.5. The intermediate decay time τ_2 is related to FRET interactions, which may occur via two main coupling channels such as direct coupling (i.e. the excitonic coupling) and indirect coupling (i.e. the excitonic coupling assisted by the plasmons) [104, 105]. Finally, the long-lived emission decay kinetics τ_3 is attributed to a small percentage of unbound dye molecules that may have persisted throughout purification of samples for those dye molecules which have not participated in energy transfer processes.

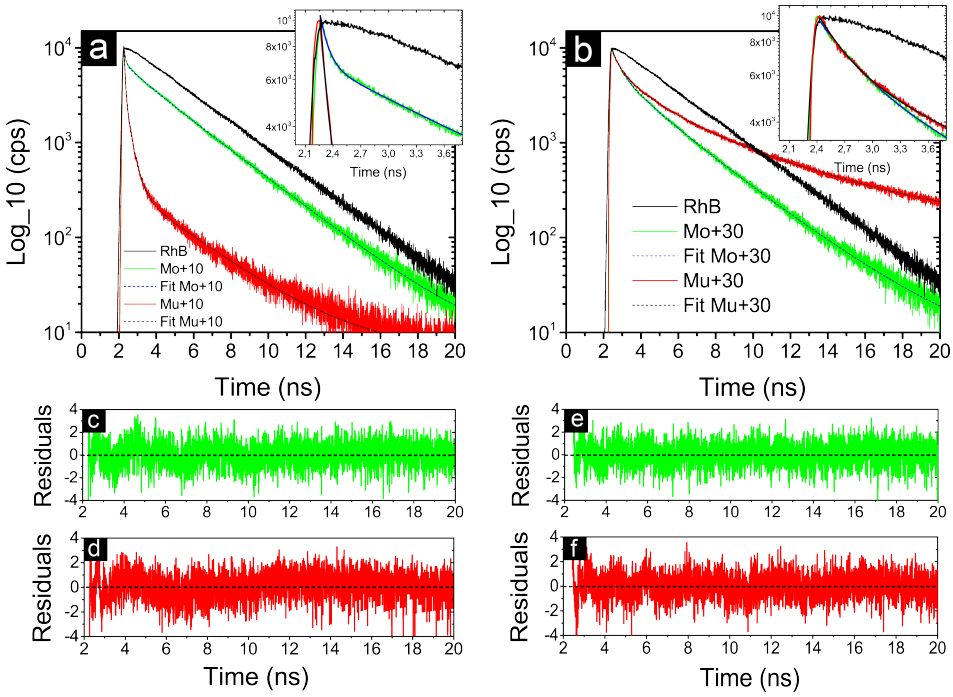

FIGURE 5.6: Time-resolved fluorescence decays and relative fitting plots of (a) monomer (Mo + 10) and multimer (Mu + 10) systems, (b) monomer (Mo + 30) and multimer (Mu + 30) systems. Panels (c–f) show residuals decay fits of Mo + 10 and Mu + 10 systems and of Mo + 30 and Mu + 30 systems, respectively.

Figure 5.6 shows the TCSPC data from active samples in order to understand the various possible gain-plasmon coupling in monomers and multimers systems with different spacer shell thicknesses, as sketched in figure 5.5. For an ethanolic solution of RhB molecules, the time resolved fluorescence decay curve can be fitted with a single-exponential function resulting in a lifetime of about $\tau_D \sim 3$ ns ($\chi^2 = 1.192$) as shown in figure 5.6(a) and (b) [106]. The observed results are consistent with previous studies which have been performed in RhB doped silica beads. Figure 5.6 compares the TCSPC data obtained at emission wavelength 572 nm, for dye molecules functionalized in monomeric (green lines) and multimeric (red lines) systems when irradiated with a 375 nm ultrafast pulsed laser. The results of the TCSPC data fit of these samples are labeled such as blue dots for monomers and black dots for multimers are presented in Table 5.1 from figure 5.6. From TCSPC data of Mo+10 system (green dots and blue line fit), a fast decay ($\tau_1 = 88$ ps, $\chi^2 = 1.14$) is accompanied by an intermediate decay time ($\tau_2 = 971$ ps) and a long-living emission where the decay kinetics can be assimilated to the fluorescence decay of pure RhB dye molecules ($\tau_3 = 2.9$ ns). Comparative analysis has been performed on decay curve of Mu+10 nanostructures (red dots and black line fit), and three decay times of $\tau_1 = 70$ ps, $\tau_2 = 332$ ps and $\tau_3 = 3$ ns have been

extracted for this system (χ^2 = 1.27). The experimental data show a significant reduction of the lifetime of exciton states in multimeric systems with respect to a single NP (monomer), reflecting a stronger plexcitonic coupling in multimers. The obtained re-

Sample	λ_{ex} (nm)	λ_{em} (nm)	τ_1 (ps)	τ_2 (ps)	$\tau_3(ps)$	χ^2
Mu+10	375	572	70 ± 1	323± 3	3.00 ±0.01	1.27
Mo+10	375	572	88 ± 2	971± 56	2.90 ±0.01	1.14
Mu+10	375	572	325 ±7	1582 ± 40	5.32 ±0.01	1.18
Mo+30	375	572	452 ± 10	1860 ± 20	3.2 ± 0.1	1.07

TABLE 5.1: Time resolved fluorescence decay results for monomeric and multimeric systems with 10 nm and 30 nm fluorophore–NP separation distances. λ_{ex} and λ_{em} stand for excitation and emission wavelengths, respectively. τ_1, τ_2 and τ_3 are the components of the tri-exponential function used to fit the TCSPC data correlated to each one of active samples. χ^2 is the chi-square function which shows the goodness of the applied fit.

sults are also in agreement with the steady-state fluorescence spectroscopy data, where multimers show a higher fluorescence quenching efficiency with respect to the corresponding monomers. Besides the direct coupling between fluorophores embedded in a single NP, the nanospheres constituting a multimeric structure enhance the indirect coupling between dye molecules via the plasmonic gold core, which results in a shortening of intermediate decay time τ_2 for the case of Mu+10 as compared to Mo+10. The long-living emission decay times τ_3 of both samples are almost the same, being associated with the fluorescence decay time of non-interacting supernatant dye molecules.

Furthermore, a comparative set of lifetime measurements has been performed on Mo+30 and Mu+30 nanostructures, where the chromophores are located 30 nm apart from the gold cores (see Table 5.1). The acquired lifetimes of Mo+30 and Mu+30 systems reveal that Mu+30 samples show a reduction in both short- and intermediate lifetimes with respect to Mo+30 monomers, indicating the occurrence of more effective dye–NP and dye–dye couplings in the Mu + 30 system.

Hence, these data indicate these important points.

(1) Non-radiative RET processes occur between chromophores and metal cores leading to very short lifetimes τ_1

(2) Plasmon–exciton RET is drastically affected by their separation distance.

(3) As a result of the plasmon hybridization process, multimeric systems generally create more intense plasmonic hot-spots (high local fields), providing stronger plasmon–exciton coupling with respect to monomeric systems.

(4) Intermediate decay times (τ_2) infer that the decrease of silica shell thickness as well as enhanced local fields, further promotes indirect couplings, irrespective of monomeric

or multimeric systems.

(5) These results show that energy transfer processes between exciton and plasmon states occur over 30 nm separation distances.

The presence of RET for such inter-distances proves that in contrast to FRET (max inter-distance 10 nm), plexcitonic RET can occur even for longer interparticle distances up to 30–40 nm.

5.7 Pump-Probe Rayleigh Experiments

In order to confirm optical loss mitigation phenomenon in designed gain-plasmon systems, two main experiments of optical transmission and Rayleigh scattering must be performed based on a pump-probe setup.

5.7.1 Pump-probe Rayleigh Experimental set-up

Scheme of pump-probe Rayleigh setup has been demonstrated in figure 5.7. In this setup, the sample S is optically lamp-pumped with 4 ns pulses of the third harmonic of a Nd:YAG laser, Brio manufactured by Quantel. This laser can generate the funda-

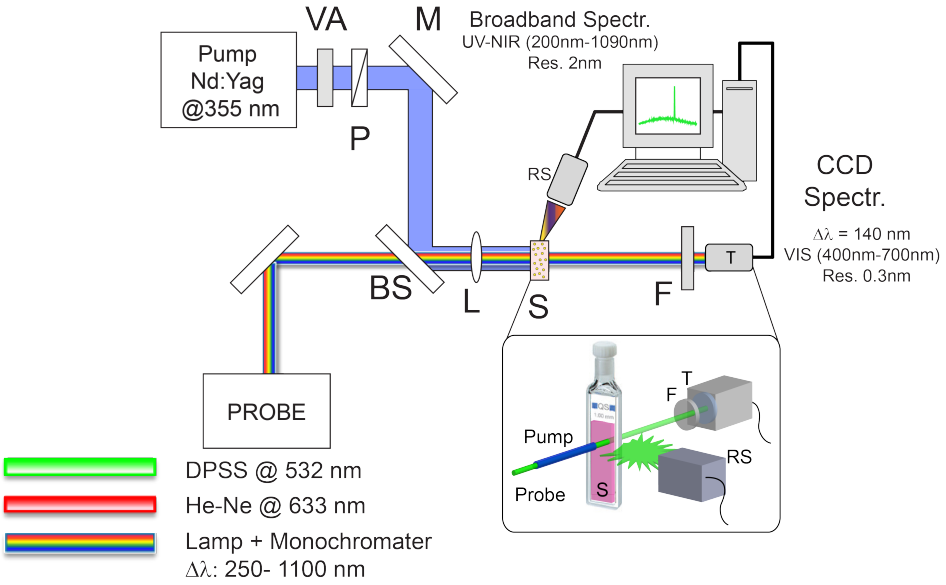

FIGURE 5.7: Normalized Rayleigh scattering (a and c) and transmission (b and d) signals of the probe beam (532 nm) as a function of the pump energy (355 nm) for multimeric systems: (a and b) Mu+10 and (c and d) Mu+30. Lower threshold values of transmittance and scattering are observed for the Mu+10 system compared to Mu+30.

mental wavelength of Nd:YAG at 1064 nm or its harmonics (532 nm, 355 nm, 266 nm). This is achieved by specific modules (2ω, 3ω , 4ω) easily plugged onto the optical head with no alignment required. The harmonic generator is made with different kinds of the crystals, depending of the oscillator type and requested wavelength. However, in this research work, the third harmonic (λ= 355nm) of this laser is applied and the second generated harmonic (λ = 532nm) is eliminated by a proper filter, placed in laser beam path. Pulses are produced with repetition rate of the laser is 20 HZ. The energy of the output laser beam can be controlled by a half wave plate, indicate by symbol of VA in figure 5.7.

According to the properties of the synthesized hybrid systems, different types of probe beam are applied. In fact, the probe wavelength was chosen in the proximity of the overlapping region between dye fluorescence and plasmon band maxima, where localized surface plasmon modes are expected. In particular, the continuous wave diode-pumped solid-state laser at 532nm manufactured by Laser Quantum is used as a probe beam. This laser provides the possibility to adjust the intensity of the output beam. However, during the experiment it operates with a fixed low power which is focused within the excitation region of the sample. In addition, a xenon based lamp with a monochromator by LOT-Oriel Group, which can produce a spectrum of light ranged from 250nm to 1100nm with 1nm wavelength resolution. During the experiment, the power of the lamp is fixed and the generated light beam is focused within the pumped region of the sample. Furthermore, this setup is equipped by Helium-Neon gas laser, operating at 633nm. The output beam intensity is tunable by a half-wave plate, positioned in beam path. The probe light emitted, scattered, or transmitted by samples can be collected by means of two types of detectors such as

(1) A high-resolution spectrometer, fabricated by HORIBA Jobin-Yvon MicroHR Symphony. This spectrometer features a 140 mm focal length, a 400nm to 700nm wavelength range and 0.3nm wavelength resolution, with adjustable slits, a high precision counter, and an interchangeable kinematic grating mount. (2) A broadband compact spectrometer (SPM-002-ET Hamamatsu S9840 Back-Thinned CCD), manufactured by Photon-Control. This spectrometer operates in UV-NIR light spectra, ranged from 200nm to 1090nm with wavelength resolution of 2nm, which can connect directly to a laptop or desktop PC through USB port. The position of the employed spectrometer is determined depending on the particular experiment. The fiber is positioned at the angle of 70° relative to the beam propagation direction for scattering (90°for fluorescence) experiment, within several millimeters from the sample. In the case of Rayleigh scattering measurement the pump beam is focused onto the sample by means of a spherical

lens L (f = 100nm), yielding a beam waist of about 100 μm at the focus position. Transmission signals are acquired far from the sample, on the same pump beam direction and with a high neutral filter in front of the fiber head, in order to prevent any possible signal different from the probe one (high stable power). A pin-hole and a notch filter (F in figure 5.7) provide the best conditions to avoid stray light and any other undesired contribution to the transmitted light.

5.7.2 Pump-probe Rayleigh Experiments on active monomers and multimers

In order to gain further understanding of the effects related to the interplay between excitons and plasmons in the investigated systems, pump–probe experiments have been performed as described in figure 5.7. According to the Beer–Lambert law, simultaneously measuring Rayleigh scattering and transient absorption, both in the absence and presence of gain, allow us to determine if the extinction curve of the plasmonic structure is affected by resonant energy transfer processes. Thus, modifications of the Rayleigh scattering and transmitted intensity of probe beams have been monitored as a function of the pump energy for all systems (excitation wavelength λ_{exc} = 355 nm). The pumping wavelength was selected to avoid direct excitation of the NP plasmon states and to excite only the RhB dye molecules. We also made sure that the optical pumping was not inducing significant changes in the sample by measuring transmitted and scattering intensity before and after pumping events. As first proposed by Lawandy, the localized SP resonance in metallic nanospheres is expected to show a singularity when the surrounding dielectric medium provides a critical value of optical gain [18]. This can be evidenced by an increase in the Rayleigh scattering signal because of the enhancement of the local field around the metal nano-antenna. Pump–probe Rayleigh scattering experiments have been performed by collinearly launching a probe beam in a small portion of the volume excited by a pump beam at 355 nm. The modification of the scattered probe beam is detected at an angle of 70° relative to the beam propagation direction. The scattered probe light, acquired by means of the optical fiber of a high-resolution spectrometer was observed in the spectrum as a relatively narrow line centered at 532 nm. Figure 5.8 shows the enhancement of Rayleigh scattering signal as a function of excitation energy in Mu + 10 multimers. The increase of the scattered signal above a given threshold value of the pump energy demonstrates the enhancement of the Rayleigh scattering cross section mediated by GPRET processes [90, 96]

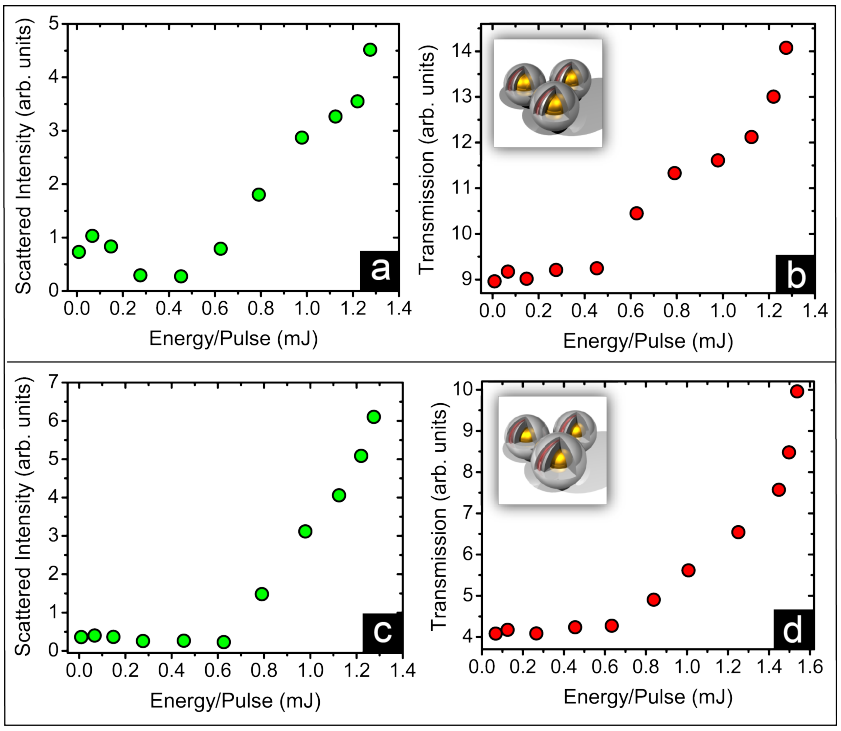

FIGURE 5.8: Normalized Rayleigh scattering (a and c) and transmission (b and d) signals of the probe beam (532 nm) as a function of the pump energy (355 nm) for multimeric systems: (a and b) Mu+10 and (c and d) Mu+30. Lower threshold values of transmittance and scattering are observed for the Mu+10 system compared to Mu+30.

Finally, the transmittance of the probe beam has been measured traversing the excited volume upon varying the pump rate and compared this with the transmittance in the absence of excitation pump. Figure 5.8 (b) shows the increase of transmission peaks of the probe signal at 532 nm as a function of excitation energy for the Mu + 10 system. Accordingly, as mentioned earlier, the simultaneous enhancement of Rayleigh scattering and optical transmittance imply the mitigation of absorptive losses, specifically in the Mu+10 hybrid system. Figure 5.8(c) and (d) show the enhancement of the Rayleigh scattering intensity and optical transmission at 532 nm, as a function of the pump rate for the Mu+30 sample. This phenomenon confirms the inter-distance dependence of the non-radiative energy transfer rate among NP–chromophore according to GPRET theory, dipolar interactions are expected to scale as r^{-4} r being the NP–chromophore separation distance [80]. Furthermore, critical behavior of the transmission was observed above a given threshold value of about 0.45 mJ per pulse for Mu+10, whereas the threshold value for Mu+30 was found to be about 0.63 mJ per pulse, showing a change in the RET efficiency as a function of the gain [18]. A comparative set of experiments, including both Rayleigh scattering and optical transmission have been performed on the Mo+10 and Mo+30 monomers. The results reported in figure 5.9 indicate a striking

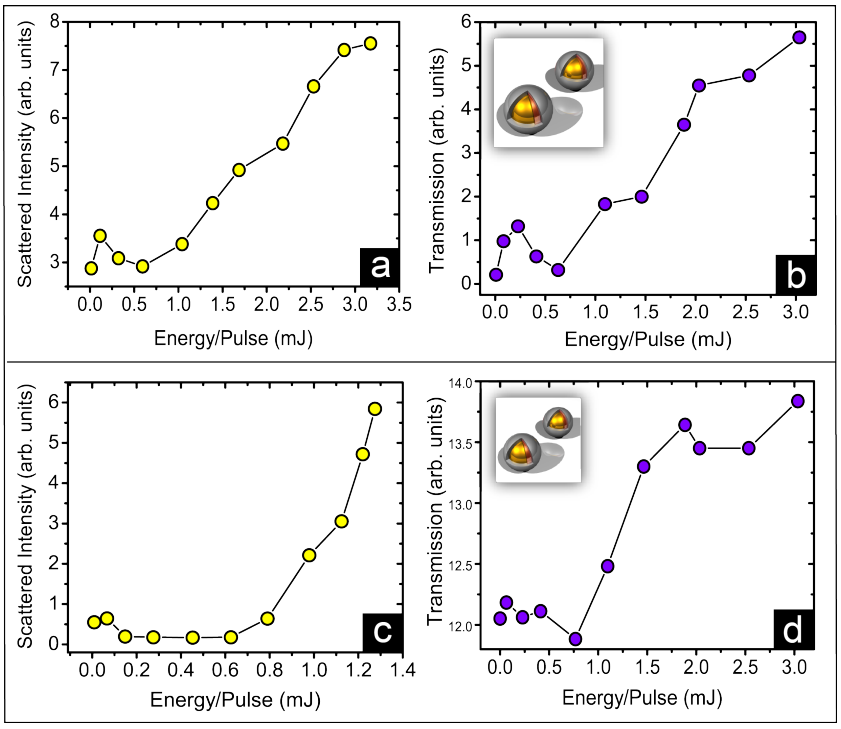

FIGURE 5.9: Normalized Rayleigh scattering (a and c) and transmission (b and d) signals of the probe beam (532 nm) as a function of the pump energy (355 nm) for monomeric systems (a and b) Mo+10 and (c and d) Mo+30. Lower threshold values of transmittance and scattering signals are observed for the Mo+10 system relative to Mo+30.

enhancement in the scattered and transmitted light above a certain gain threshold value. Evidently, the Mo+10 system demonstrates lower threshold values (0.55 mJ per pulse) with respect to the Mo+30 system (0.7 mJ per pulse). In addition, the threshold values of monomers are higher than the corresponding values for multimers. Therefore, appropriate exciton–plasmon distances in combination with stronger local fields result in a more efficient absorptive loss mitigation in hybrid plasmonic systems.

Chapter 6

Gain-Plasmon Coupling in Mesoscaled Plasmonic Systems

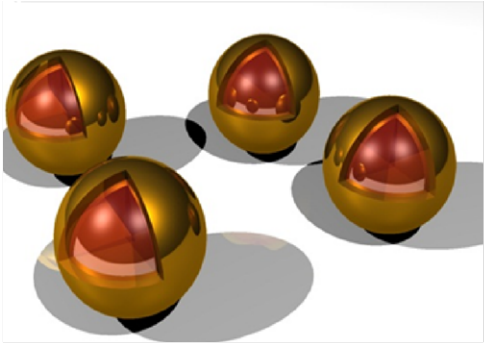

Plasmonic Nanoshells

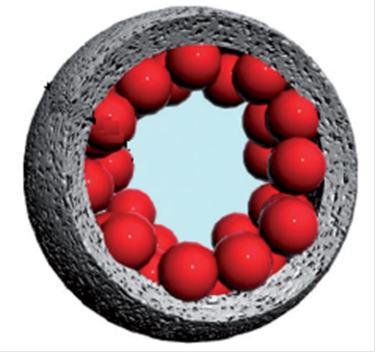

Plasmonic Mesocapsules

6.1 Gain functionalized Plasmonic nanoshells

6.1.1 Introduction

Metal based nanoshells are fabricated of a dielectric core (usually SiO_2) covered by a thin metal shell, consisting of spherical shape with diameters ranging in size from 10 to 250 nm. They possess an extensive set of optical, chemical and physical properties, which make them ideal candidates for multiple technological applications approaching from enhancing cancer detection and treatment, cellular imaging and medical biosensing to structural elements for near zero permitivity metamaterials [85, 107]. Nanoshells

function as appropriate and versatile detectable subunits because of their large extinction cross-sections, immunity to photobleaching, spectral tunability, absorption/scattering ratio tunability, electromagnetic near field enhancement and even increased luminescence. These optical properties are based on surface plasmon resonance (SPR). The optical cross-sections and luminescent properties of gold nanoshells (NSs), compared with those of conventional fluorophores and quantum dots result highly enhanced. Wu et al. found that the absorption of a single 20 nm diameter nanoshell corresponds to that of 4×10^4 molecules of a dye used in photodynamic therapy (indocyanine green, ICG) [108]. The optical extinction cross-section ($3.8\times10^{-14}m^2$) resulted more than one million times greater than the cross-section of an ICG molecule ($1.66\times10^{-20}m^2$), and almost twice the cross-section of a CdSe quantum dot ($1.5\times10^{-14}m^2$) with the same radius for nanoshells with a diameter greater than 130nm [109, 110]. The dimensionless extinction coefficient Q_{ext} of a gold nanoshell typically ranges from $\sim$3 to 7. Park et al. found that 120 nm gold NSs result 140 times brighter than 100 nm fluoresceinated polystyrene beads, which are commonly used in biological imaging applications [111]. Moreover, nanoshells offer stability towards photochemical changes such as photobleaching, whereas conventional fluorophores are highly affected to this phenomenon [112–114]. The position of the extinction (plasmon resonance) peak and the relative contributions of scattering and absorption to total extinction of NSs can be tuned by acting on two parameters, the radius of the inner core (r_1) and the outer shell (r_2) as shown in figure 6.1 [115]. For a given r_2, the position of the extinction peak is determined by the core to shell ratio (r_1/r_2) [116].

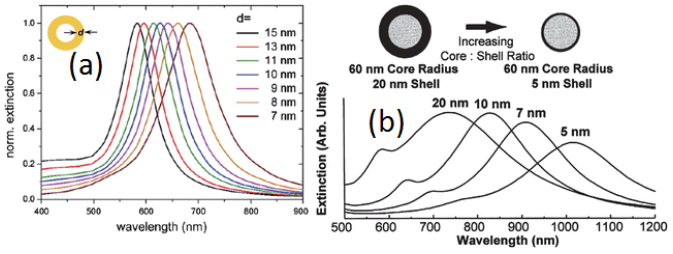

FIGURE 6.1: (a) Calculated extinction spectra of single Au/Ag nanoshells with a radius of 27.5 nm and varying shell thickness. (b) Calculated extinction spectra of silica core/gold shells NPs (core radius 60 nm) with varying shell thickness [115].

For greater core to shell ratios (thinner gold shells), the peak becomes shifted to longer wavelengths. For gold NSs, the position of the resonant extinction peak can be selectively tuned from 600 nm to greater than 1000 nm, covering the wavelength range that includes the NIR tissue window (700-900 nm), where tissue is most transparent to light . The ability of nanoshells to be tuned to the NIR is central to their functionality for

biological and medicine applications. In addition to spectral tunability, the absorption to scattering ratio of nanoshells can also be tuned by changing the nanoshell's outer radius (r_2). For smaller nanoshells, absorption dominates scattering, whereas for larger nanoshells scattering dominates absorption [107]. The contributions of absorption and scattering to total extinction can be made approximately equal among the two extremes. It is also possible to design nanoshells for dual imaging and photothermal therapy applications, where high scattering efficiencies facilitate scatter-based imaging and high absorption efficiencies facilitate photothermal therapy. Using suitable dimensions of the two parameters, the relative amounts of absorption and scattering can be selected across a wide range of wavelengths.

Gold nanoshells also exhibit another unique property, which is distinct from anything seen in conventional fluorophores. Metallic nanoparticles act as nanolenses, which efficiently focus incident electromagnetic radiation into the near field region close to their surfaces with subwavelength precision [117, 118]. Averitt et al. have predicted local field enhancements ($E_{enh} = E_{local}/E_{inc}$) of $\sim$3 for gold nanoshells with outer radii of 12-15 nm [116]. Chien et al. have calculated enhancements of $\sim$450 for assemblies of gold nanospheres, which can be thought as rows of nanolenses. Since the intensity scales as the electric field squared, these near-field enhancements produce intensity enhancements of many orders of magnitude. For the nanosphere assembly, the localized surface intensity would increase by a factor of over 2×10^6. Such enhancements have important applications in single molecule detection [119].

However, all these extraordinary properties and other possible technological applications as gain functionalized metamaterials subunits for ε near zero permitivity metamaterials are strongly limited because of the strong intrinsic optical losses suffered by these metal-based subunits, in terms of high values of imaginary part of permittivity [85, 120–122]. In fact, they are characterized by significantly low values of the figure of merit $F = Re[\varepsilon(\omega)]/Im[\varepsilon(\omega)]$, achieving to only a few decimals. To solve this drawback, and facilitate the use of their extraordinary optical properties, use of gain media to bring energy to the quasi-static electric field associated with the localized surface plasmon resonances has been proposed as discussed in the previous chapter. Theoretical studies have shown that bringing gain to metamaterials can modify the absorption cross section in terms of reduction of the imaginary part of the dielectric permittivity, by producing only slight modifications of real part $\varepsilon_1(\omega)$ [18, 87, 123]. Experimental evidences have demonstrated that exciton-plasmon coupling in gain incorporated plasmonic systems promote nonradiative energy transfer processes which is able to mitigate absorptive losses as already described in the previous chapter[87, 90, 95, 96]. In the case

of mesoscaled gain functionalized plasmonic nanoshells, strong gain-plasmon coupling not only mitigates the optical losses through nonradiative energy transfer processes, but also makes the system super absorber in selective wavelength range.

6.1.2 Synthesis of RhB dye doped plasmonic nanoshells

Synthetic process is initiated with the preparation of RITC-APS, by reacting rhodamine B isothiocyanate (RITC) with aminopropyltriethoxysilane. Later, RITC was incorporated into the silica core by following the Stöber-Fink-Bohn method [124]. The fluorescent particles were collected by centrifugation and washed three times with absolute ethanol. Their surface functionalization with (aminopropyl) triethoxysilane was carried out as described in reference [125]. Small gold seed nanoparticles were anchored onto the amine-modified surface of the SiO_2 nanoparticles using a modification of the method reported by Westscott et al [126, 127]. Known methods have been used to grow complete gold shells on the gold-seeded SiO_2 nanoparticles cores, [50, 128, 129] passing through different growth steps (see TEM images in figure. 6.2b-c). Different growths

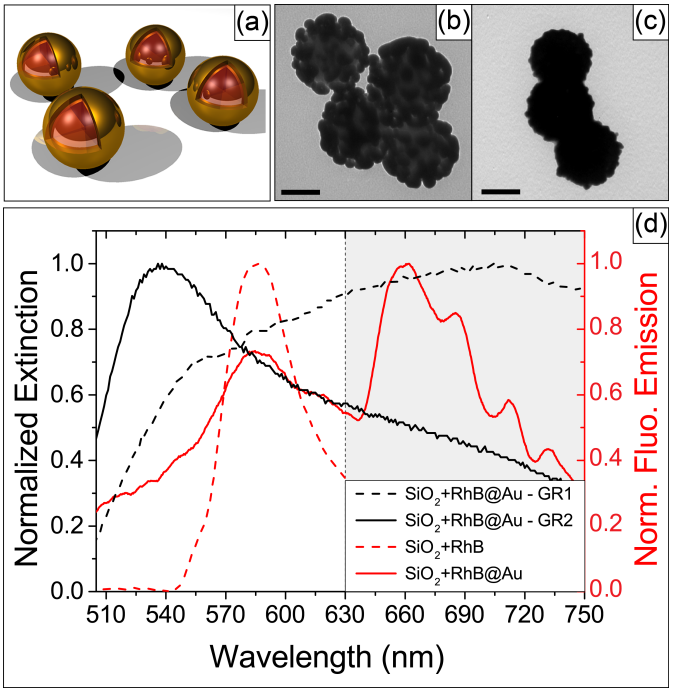

FIGURE 6.2: (a) Sketch of the dye doped silica core/gold shells. (b) TEM image of an intermediate step of the growing process of the gold shell (GR1) (bar = 100nm) (c) TEM image of the complete gold shell (GR2, 170±10nm) around the SiO_2 core (about 20nm). (d) Normalized extinction cross-section of the two gold growths (dashed and continuous black curves) and emission of $SiO_2 + RhB$ (red dashed curve) and $SiO_2 + RhB@Au$ (continuous red curve). λ_{exc} = 400nm

present different extinction curves (dashed and continuous black curves in figure 6.2(d), GR1 and GR2), showing broad plasmon resonances in both cases. In the same figure, the normalized emission of bare fluorescent silica cores dispersed in ethanol (red dashed curve) and the modified emission in presence of the gold shell (continuous red curve) have been shown. One of the possible responsible of this fluorescence behavior could be the hybridization of plasmon modes [48]. The good spectral overlapping of the two bands, obtained by means of functionalization with proper gain molecules placed right at the heart of the resonant element, has permitted to exploit resonant energy transfer (RET) processes between *RhB* molecules and plasmonic nanoshells. RET processes are at the basis of optical loss compensation mechanisms and require a series of physical and chemical conditions that have to be strictly satisfied, as spectral overlapping, dye molecules concentration, nanoparticles-dye molecules interdistance, core-shell size ratios. Material parameters have to be accounted to optimize dipolar as well as multipolar, interactions which are responsible for non-radiative resonant transfer of the excitation energy from gain units to plasmonic nano-objects.
In order to understand the impact of the interplay between gold nanoshells and dye molecules in dye doped plasmonic nanoshells, an ultrafast spectroscopic set-up has been used and to corroborate evidences of broadband mitigation of absorptive losses in gold nanoshells, time-resolved fluorescence spectroscopy have been performed on these systems, proving evidences on dye-NSs coupling and energy transfer processes.

6.1.3 Ultrafast spectroscopic set-up for pump-probe and fluorescence spectroscopy experiments

Ultrafast spectroscopic set-up has been used to perform broadband pump-probe measurements in order to investigate simultaneous scattering and transmission enhancement on a broad wavelength range and life time measurements. The used system consisting of a femtosecond Ti:Sapphire pulsed laser (red beam in figure 6.3, repetition rate = 80Mhz, pulse width = 140 fs, by Coherent Inc.), tunable in the 680-1080nm range, represents the core of a customized set-up that presents two possible investigations lines: first line includes a Pulse Picker used to decrease the repetition rate in the range between 4 and 5 MHz, in order to be synchronized with a multi pronged spectro-fluorometer able to perform both steady state measurements (by means of a Xenon lamp and multiple gratings, by Edinburgh) and time correlated single photon counting investigations. In the

same line, a Second Harmonic Generation (SHG) module is used to decrease the excitation wavelength in the range 340-540nm (blue beam in figure 6.3). All the above mentioned investigations are performed inside the spectrometer chamber (sample position H1). Second investigation line (dashed white on red beam in figure 6.3) includes all the components used to perform broadband pump-probe analysis, both in transmission and scattering configuration (D1 and D2). An infrared light beam (from 750nm to 900nm) is sent to a 30:70 beam splitter without passing through the pulse picker, 70 percentage of the beam is duplicated in frequency and used to excite sample in position H2 (outside the chamber). At the same time, the remaining 30% is used to generate super continuum light from a nonlinear photonic crystal fiber, to obtain a probe beam with a broadband distribution (500-1000nm), phase matched with the primary pulsed beam. Pump and probe beams are coupled by means of a beam coupler (BC) and co-

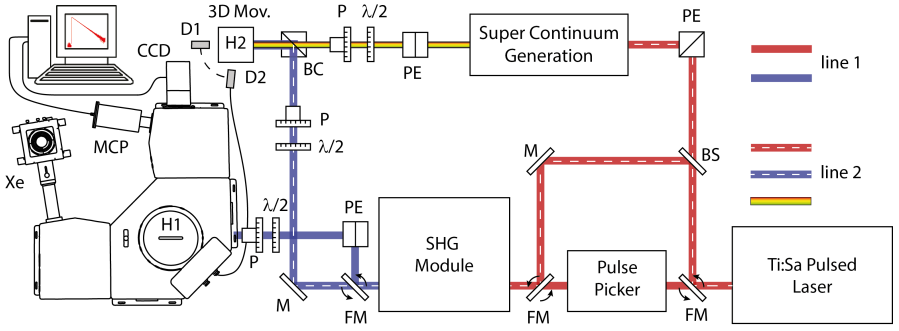

FIGURE 6.3: A schematic view of the Ultrafast spectroscopic set-up used for both pump-probe experiments and fluorescence spectroscopy measurements.

launched on the 3D holder sample (H2). A larger beam waist is chosen for pump beam with respect the probe one, in order to be sure to investigate an area really shined by pump light. Transmitted (D1) and scattered (D2) light are collected with a multimode fiber and sent inside the spectrometer chamber in order to be spectroscopically analyzed by means of a CCD camera (by Andor). A multi channel plate, synchronized with the incoming pulses, is instead used to acquire the fluorescence decay lifetime in the proper temporal range. Broadband half waveplates ($\lambda/2$) and high damage threshold polarizers (P) are used to control the pump and probe power. Three periscopes (PE) have been used to have each time an in-plane beam at different heights.

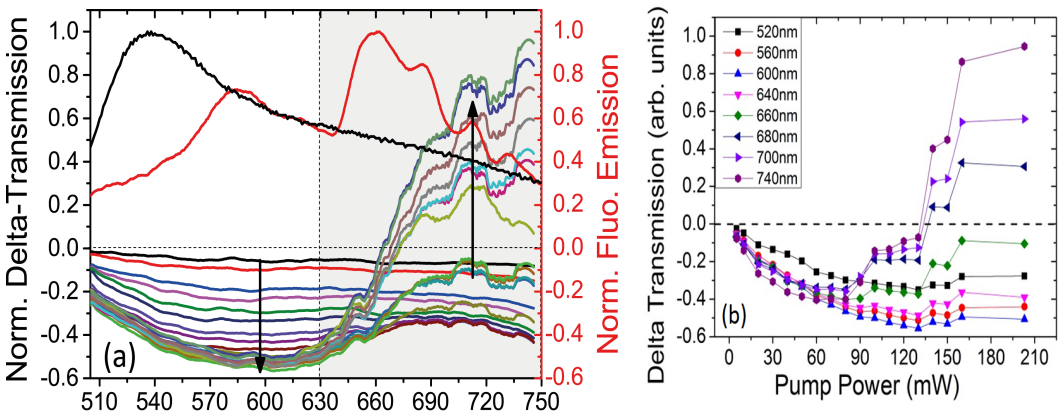

FIGURE 6.4: (a) Delta of transmission behavior as a function of excitation energy. Double behavior observed in the two spectral regions 510-630nm (super absorber) and 630-750nm (enhanced transmission as low lossy). (b) Particular wavelength cuts for transmitted probe intensity as a function of pump energy showing wavelength dependent double behavior in the system.

6.1.4 RhB doped nanoshells as simulataneous super absorber and low loss systems

Now, pump- probe experiments have been performed through a systematic approach either to evaluate known effects which arise during resonant energy transfers and by measuring key physical quantities as function of excitation energy. An ultrafast spectroscopic pump-probe set-up has been used to simultaneously excite and probe the same volume of ethanol dispersed gain functionalised plasmonic nanoshells in order to observe transmission and Rayleigh scattering of a probe beam as described in figure 6.3. A pulsed Ti:S laser has been used at particular wavelength ($\lambda = 800nm$), as excitation source to pump after passing through SHG and as a probe beam after passing through photonic crystal fiber (PCF) in order to generate supercontinuum light in the range 500-1000nm. Transmitted probe beam experiences two distinct effects due to the reciprocal overlapping of the wide plasmon resonance and the modified RhB emission. The presence of a double peak in the RhB emission allows the appearance of two different phenomena in the plasmon-exciton interplay and coupling. Delta of transmission of broadband probe beam was measured as a function of the excitation energy ($\lambda_{exc} = 400nm$), in the entire overlapping spectral region. Delta transmission is defined as

$$\Delta_T = \frac{I_T(wp) - I_T(wop)}{I_T(wop)} \tag{6.1}$$

Where $I_T(wp)$ represents the transmitted intensity when excitation is ON, $I_T(wop)$ when excitation is OFF, taking into account the fluorescence of the sample and the background signal. As shown in figure 6.4 (a), in the range 510-630 nm the system experiences an overall decreasing of delta of transmission (below zero) showing significant absorbing behavior, whereas in the spectral range between 630-750nm, Δ_T become positive, showing the enhanced transparent nature of system. Thus, The same system behaves as super-absorber in the 510-630nm range, and as a plasmonic low loss metastructure in the 630-750nm band. Furthermore, In order to demonstrate this special behavior of the system in more clear way, Δ_T has been extracted for particular wavelengths lying in absorbing band and transmission band as a function of pump power. Figure 6.4 (b) reiterates the super absorbing nature, reporting negative Δ_T values for five wavelength cuts ranging 520 to 640 nm and positive ones for 680-740 nm wavelength cuts, followed by 40 nm wavelength interval.

Figure 6.5 shows the normalized scattering intensity as a function of excitation energy,

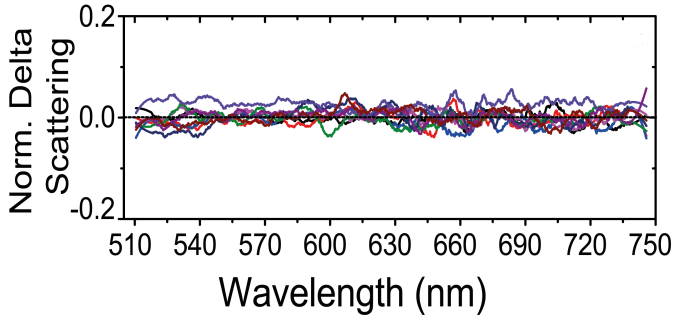

FIGURE 6.5: Normalized scattering intensity behavior of broadband probe beam as a function of excitation energy.

which remains almost constant for broadband spectral range . Such constant behavior can be ascribed due to big size of meso-scaled particles where the scattered probe light cannot be considered as Rayleigh scattering. The whole system can be explained on the basis of diminished and enhanced transmission as an overall modification of the absorption cross-section , but in an opposite way in the two spectral regions. which occurs due to strong plasmon-exciton coupling in the system.

6.1.5 Time resolved fluorescence spectroscopy

To better investigate the interplay between gold nanoshells and dye molecules and to corroborate evidences of broadband mitigation of absorptive losses in gold nanoshells,

time-resolved fluorescence spectroscopy have been carried out on RhB dye doped plasmonic nanoshells in order to prove dye-NSs coupling and energy transfer processes, using line 1 of ultrafast spectroscopic set-up as shown in figure 6.3. Fluorescence lifetime measurements demonstrate a significant quenching behavior, consistent with the right separation distance from dyes to the thin gold shell, because of their strong resonant coupling. As it is already described in previous chapter in the case gain functionalized NPs that optical emission of fluorescent guest molecules is followed either by radiative and nonradiative decays. In case of a strong plasmon-exciton coupling the probability of nonradiative decay can assume a very high rate (K_{nrad}), so that it may become the main decay channel of excited dye molecules. Then, radiative decay rate (K_{rad}) can be reduced to a little fraction of the total decay rate, producing a considerable effect of fluorescence quenching. It can be understood by this simple relation $K_{fluo}(r) = K_{rad}(r) + K_{nrad}(r)$ [75]. Same ultrafast setup has been used to measure de-

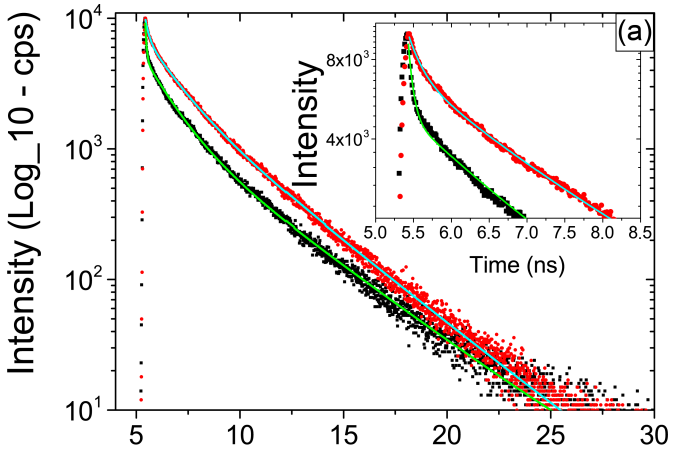

(b)

Sample \ Decay Time (ns)	τ_1	τ_2	τ_3
SiO_2 + RhB	0.18 ± 0.01	1.35 ± 0.01	3.76 ± 0.01
SiO_2 + RhB@Au	0.06 ± 0.01	1.25 ± 0.01	3.46 ± 0.01

FIGURE 6.6: (a) Time-resolved fluorescence intensity decays for $SiO_2 + RhB$ (red dots) and $SiO_2 + RhB@Au$ (black squares), together with the tri-exponential fits. While, Inset shows the first fast and intermediate decay time behavior. (b) Table reporting the three decay times obtained from the fitting process on the two samples.

cay times. To enable the spectro-fluorometer to be synchronized with the Ti:S pulses, a pulse picker is used to decrease the repetition rate from 80MHz to 4MHz (see line 1 in figure 6.3, in which H1 is the sample position). Figure 6.6 (a) reports the decay time of $SiO_2 + RhB$ (red curve) and $SiO_2 + RhB@Au$ (black curve) with their fitting curves. The fitting procedure of the emission intensity decays $I(t)$ uses a tri-exponential model

according to the following expression,

$$I(t) = \sum_{i=1}^{3} (\alpha_i exp(-t/\tau_i) \tag{6.2}$$

Where τ_i are the decay times and α_i represent the amplitudes of components at t=0. Figure 6.6 (b) shows a table, comparing the all three life time observed in both $SiO_2 + RhB$ and $SiO_2 + RhB@Au$ samples. The presence of a very fast decay time (τ_1) is attributed to a significant decrease of radiative rate due to embedded dye molecules into the silica core coupled to the plasmonic gold shells, which experience a strong dipole-metal RET process. The extracted fit reports a three-fold reduction on this fast decay time, droping from 180ps to 60ps. The intermediate decay time (τ_2) is correlated to dipole-dipole FRET interactions, which can happen as direct coupling between excimers of embedded dye molecules, and indirect coupling of dye excimers via gold shells, observing a small reduction of only 7.5%. The long-living emission decay kinetics (τ_3) are due to those dye molecules that do not overcome coupling effects because far from the metal shell. In this case the two times resulted equals.

6.2 Gain Assisted Plasmonic Mesocapsules

Nanoplasmonics has received a drastically strong boost by the recent development of sophisticated characterization techniques and the great advancement of fabrication methods based on nanochemistry routes and assemblies [130]. Plasmonic mesocapsules represent a perfect example of chemistry, material science, and optics collaborations and demonstrate the ability to concentrate light at the nanometer scale for the simultaneous performance and optical monitoring of thermally activated chemical processes. Such complex metallo-dielectric systems can also be named as plasmonic nanoreactors, consisting of encapsulation of plasmonic nanoparticles on the inner walls of mesoporous silica capsules. A Diels alder cycloaddition reaction was carried out in the inner cavities of these nanoreactors to evidence their efficacy. It has been successfully demonstrated that reactions can be accomplished in a confined volume without alteration of the temperature of the bulk solvent, while allowing real time monitoring of the reaction progress [131].

Moreover, gain assisted plasmonic mesocapsules can also play an important role in order to realize plasmonic devices, owing to its broader plasmon band in the visible range

and its larger size. However, the crucial point of the metal based plasmonic materials remains the intrinsic optical losses located at the resonance frequencies. In fact, the strong radiation damping at visible wavelengths leads to the shadowing of their extraordinary electromagnetic properties. Gain-enhanced materials are a potential solution to this problem [85–87, 132, 133], but the conception of realistic three dimensional designs is still a challenging task. The idea is to optimize plasmon-gain dynamics so that coherent and non-radiative energy transfer processes between excitonic states (chromophores-donor) and plasmon states (metal-acceptor) can effectively occur as described in the previous chapter. Upon programming this interplay by controlling the dominant parameters of plasmon-gain interaction provides a powerful tool to trigger relevant physical effects such as optical loss compensation, super-absorption, enhanced photoluminescence, surface enhanced Raman scattering and laser action.

This section of the chapter reports on the loss mitigation observed in a dispersion of porous silica mesocapsules embedding plasmonic nanoparticles in a gain-doped solution. These plasmonic mesocapsules, obtained via colloid chemistry routes, show a broad plasmon resonance band covering a large portion of the visible spectrum (500-700 nm). The gain assisted plasmonic capsules, a hierarchical organization of metal nanostructures, allow to exploit key physical parameters to promote effective gain-plasmon interplay. Sophisticated experiments such as ultrafast time resolved spectroscopy and broadband femtosecond pump-probe laser spectroscopy reveal striking opto-plasmonic features, demonstrating a substantial gain-induced broad-band loss mitigation. Previous reported systems, based on the study of gold nanospheres functionalized with gain refers to selective optical loss mitigation has been observed [90, 95, 96]. In that case, although optical losses were efficiently attenuated which was restricted to a narrow spectral range. Here, the present work shows the first experimental evidence of optical loss mitigation in such plasmonic system, exhibiting broad plasmon band in visible range. It represents therefore a step forward in the direction of bulk plasmonic materials.

6.2.1 Synthesis of plasmonic mesocapsules

Plasmonic mesocapsules have been synthesized by our chemistry collaborators. Polystyrene (PS) beads of 530 nm were functionalized by using the layer by layer assembly technique(LbL) resulting in an ordered multilayer composed of 4 monolayers of polyelectrolyte (PS/PSS/PAH/PSS/PAH) where PAH stands for poly(allylamine hydrochloride) (Mw 56000) and PSS for poly(sodium styrene sulfonate) (Mw 70000) [134–136]. This

polyelectrolyte film provides the PS particles with the necessary electrostatic functionality for the adsorption of gold seeds. The gold seeds (1-3 nm; [Au] = 10^{-3}M) were synthesized as described elsewhere [126]. In this case, 10 ml of functionalized PS beads (2.5 mg ml^{-1}) were added dropwise to 50 ml of Au seeds solution under sonication. The resultant solution was standing for 2h. The excess of gold seeds non deposited on the PS surface was removed by three centrifugation-redispersion cycles with pure water (5000 rpm, 20 min). The final redispersion was in 5 ml of an 1:1 ethanol/water mixture.
In order to carry out the mesoporous silica coating, the method described by Yonghui Deng et al. [137] was partially followed. Briefly, the previous PS@Au-seeds suspension, 5 mg ml^{-1}, was added drop by drop under sonication to a mixed solution of CTAB (200 mg), deionized water (80 ml), ammonia aqueous solution (28 wt%, 0.730 ml) and ethanol (60 ml). The resultant solution was homogenized by sonication for 20 minutes. Then, 2 ml of a 5% (v/v) solution of tetraethoxysilane (TEOS) in ethanol was added dropwise to the previous suspension under sonication. This mixture was stirring for 2 days in order to have a homogeneous silica growth. Then it was centrifuged three times and washed with water. Polystyrene and CTAB templates were removed by calcination at 550 °C for 20h. A solution of gold pre-reduced Au^{+} was prepared and first growth of gold seeds inside the mesoporous capsules was achieved by adding 57 ml of Au^{+} solution and 170 μl of formaldehyde solution (37 wt%) to 10 ml, 2.5mg ml^{-1} of Au-seeds@SiO_2 mesoporous-h under vigorous stirring. After 5 minutes of reaction, the color of the solution changed from red to purple-blue and 15 minutes later, from purple-blue to grey-blue. The sample was centrifuged three times and washed with water. A second growth was carried out just by adding 40 ml of Au^{+} solution and 90 μl of formaldehyde to a volume of 5 ml, 2.5 mg ml^{-1} of the previous solution. After 30 minutes of vigorous stirring, the sample was cleaned by three centrifugation-redispersion cycles with pure water. The final redispersion of the capsules after the first and second growth was in ethanol.

TEM image have been shown for the synthesized mesocapsules in figure 6.7. It features different mesocapsules and evidences the uniformity of the sample in term of size, morphology and Au NPs distribution. Moreover, In figure 6.8 ,TEM images for two mesocapsules have been shown at different Au NPs growth level. In particular, the mesocapsule type in figure 6.8(b) is obtained starting from the one shown in figure 6.8(a) and by using the NPs already present as catalyst seed to grow bigger NPs. If any trace of gold was present on the outer surface of silica before the catalysis reaction it would have grown as well. Figure 6.8(b) confirms that gold grows only inside the cavity.

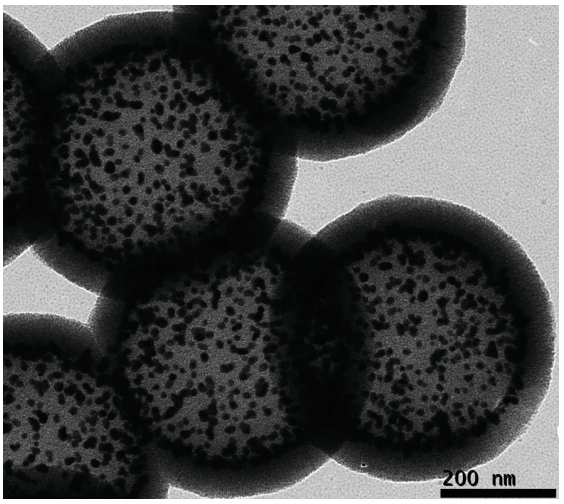

FIGURE 6.7: TEM image for several plasmonic mesocapsules

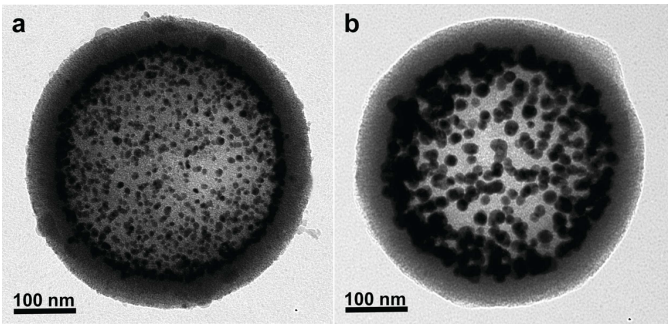

FIGURE 6.8: TEM pictures for mesocapsules showing different Au NPs sizes

6.2.2 Incorporation of gain to plasmonic mesocapsules

Figure 6.9 shows designed and fabricated plasmonic structures, with a diameter of 530 nm, resembling a reverse bumpy ball configuration in which multiple Au NPs are engrafted on the inner walls of porous silica capsules, as described in above synthesis section. Plasmonic mesocapsules fabrication procedure and interaction of gain media to Au NPs have been shown schematically in figure 6.9 (a). Figure 6.9(b) shows the typical Transmission Electron Microscope (TEM) image of a plasmonic mesocapsule in which Au NPs supported on the inner wall of the porous silica shell are clearly visible as dark spots. Figure 6.9(c) shows the statistical distribution of their diameters, its average is 11.5 ± 1.7 nm. The spatial distribution of the Au NPs growth at the inner wall of the silica shell is clearly evidenced by the Focused Ion Beam (FIB) cross-section analysis of a typical plasmonic capsule as shown in figure 6.9(f). Scanning Transmission Electron Microscopy (STEM) in figure 6.9(d) and X-ray Energy Dispersive Spectroscopy (XEDS) in figure 6.9(e) provide further evidences about the homogeneous nature of the silica shell, moreover no trace of gold is detected on its outer surface.

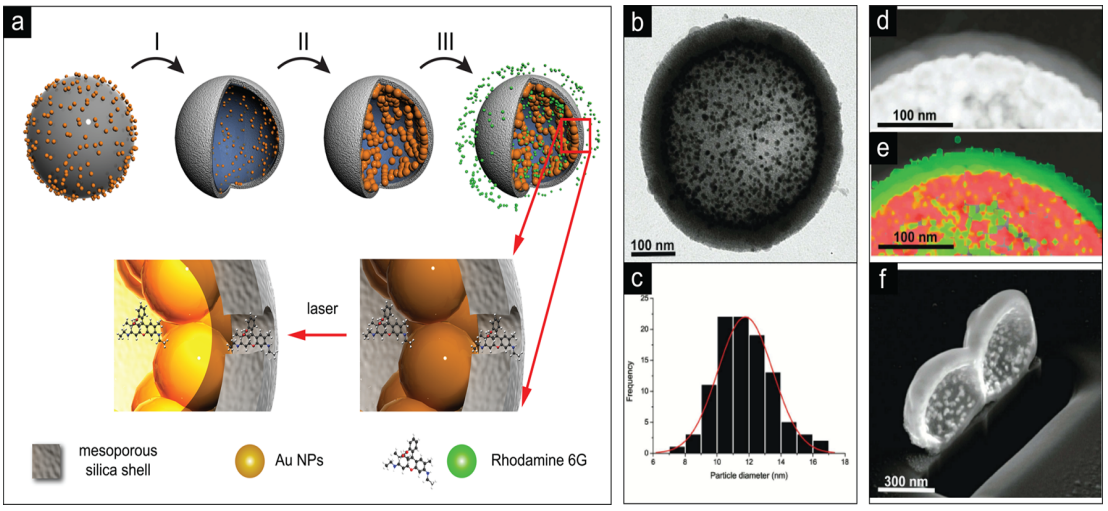

FIGURE 6.9: (a) Schematic of the synthesis of plasmonic mesocapsules and incorporation of R6G as gain media to structures. (b) TEM image of a typical plasmonic mesocapsule (c) Statistical distribution of Au NPs diameters, with an average of 11.5±1.7 nm. (d) STEM and (e) combined XEDS elemental mapping images from the same mesocapsule, Au = red and SiO_2 = green; (f) FIB cross-section image.

6.2.3 Spectral overlapping of plasmonic mesocapsules with gain medium

It must be noticed that plasmonic band resulting from the nanoparticles arrangement, produces a spectrally wider and red-shifted resonance compared to the one of the single metal nanoparticle, which is observed at 520 nm with a narrow peak. In fact, it is known that nanoresonators alone would produce a specific plasmon resonance, but, when in close proximity mix and hybridize creating a completely different response. Nano-porous silica was chosen for the dielectric shell because is a largely used host material for encapsulating dyes or drugs by means of a simple impregnation approach [138]. The pores (2-5 nm in diameter) of the silica shell have been loaded with Rhodamine 6G (R6G) as the gain material by soaking the plasmonic mesostructures in an ethanolic R6G solution. R6G has been chosen because its emission spectrum overlaps mesocapsule plasmonic band in order to fulfill the resonant energy transfer condition, as shown in figure 6.10. As it is described in the previous chapter, dealing with the effect of isolated metallic nanoparticles on the fluorophores spontaneous emission rate, has been demonstrated that the non-radiative energy transfer processes are largely dependent on distance, with a maximum located where the plasmonic field is more intense, namely at few nanometers from the nanoparticle surface [47, 83, 88, 99]. In the case of plasmonic mesoporous capsules, impregnation of the hollow cores with the gain molecules

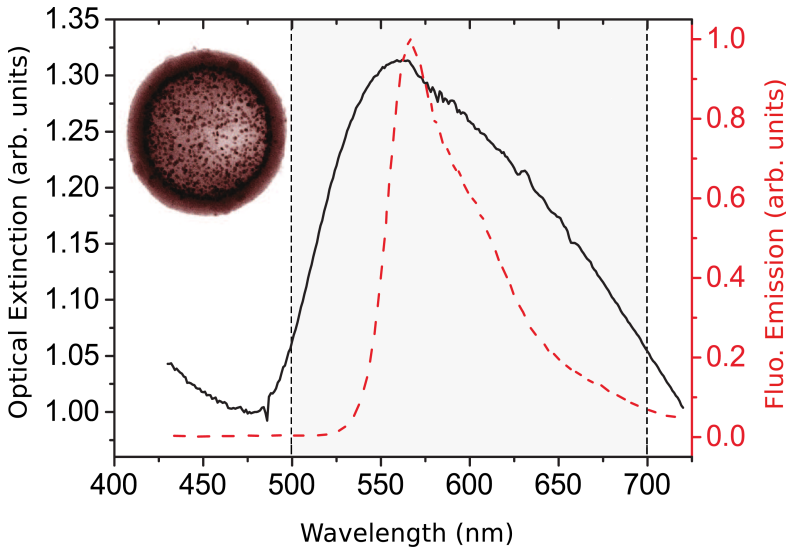

FIGURE 6.10: Mesocapsules broad plasmonic resonance (black continuous line) and R6G fluorescence emission spectrum (red dashed line), showing the significant spectral overlapping.

enables strong gain-plasmon coupling and results to be very effective for the promotion of non-radiative energy transfer processes.

6.2.4 Fluorescence quenching in gain assisted plasmonic mesocapsules

Now, it is well-known that close proximity of gain molecules to plasmonic NPs as a result of remarkable enhancement of non-radiative decay rate with respect to radiative decay rate. Such phenomenon leads to a drastic fluorescence quenching of fluorophores. In order to understand triggered non radiative energy transfer processes in the system, gain assisted plasmonic mesocapsules has been prepared by mixing R6G at a concentration Cr =1.2 mg ml^{-1} dispersed in ethanol and mesocapsules at Cr = 7.5 mg ml^{-1} and is labeled as C2-S3 , while the similar solution of R6G is used as reference sample, naming R6G in the figure 6.11. Fluorescence emission of R6G dye molecules in both samples, pure ethanol-based R6G solution and R6G assisted plasmonic mesocapsule have been acquired by optically pumping with large spotted pulse trains of a tripled Nd:YAG laser (λ_{exc} = 355 nm) as a function of pump power. Fluorescence quenching efficiency has been calculated using the values in the inset of figure 6.11 as

$$Q = 1 - \left(\frac{F}{F_0}\right) \tag{6.3}$$

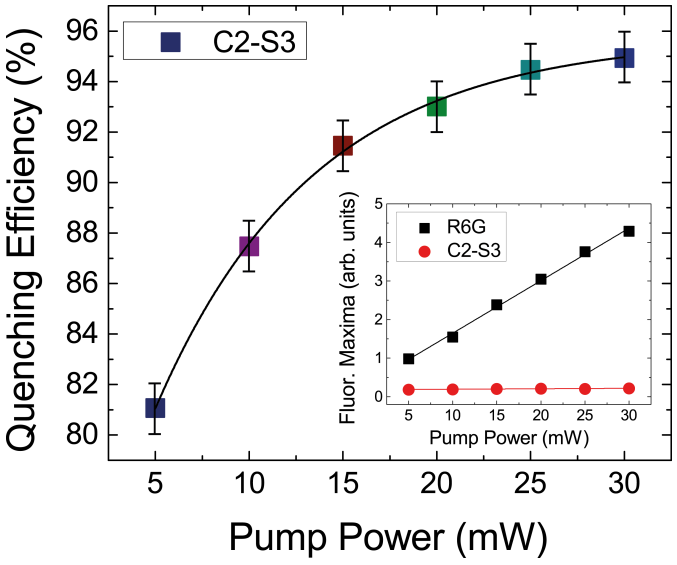

FIGURE 6.11: Fluorescence quenching efficiency as a function of the pump energy. Inset of the figure shows the fluorescence maxima of R6G at a concentration Cr =1.2 mg ml^{-1} in ethanol (black squares) and the fluorescence maxima for a isoconcentrated solution of R6G in which mesocapsules (Cr = 7.5 mg ml^{-1}) (red dots) are dispersed. The fluorescence quenching efficiency has been calculated by using the data in the inset.

Where F and F_0 are the fluorescence signal intensity in presence and in absence of mesocapsules, as a function of the pump power. The non-linear increasing of Q as a function of the pump power can be ascribed to the resonant energy transfer processes occurring between plasmonic mesocapsules and dye molecules. Inset of figure 6.11 shows the fluorescence quenching observed in the gain assisted plasmonic mesocapsules (C2-S3) with respect to isoconcentrated ethanol-based R6G solution. If the two media were uncoupled, the mesocapsules would have act like static quenchers and the quenching rate would have been constant.

6.2.5 Time resolved spectroscopy on gain assisted mesocapsules

As it has also been explained in the previous chapter in detail, life time of a fluorescent system depends on radiative as well as nonradiative decay rates. Shortening of the lifetime of a dye molecule in close proximity of a plasmonic quencher can be due to the enhancement of the nonradiative decay rates. Time resolved spectroscopy has been performed on the two gain assisted different concentrated plasmonic mesocapsules (C1=1.25 mg ml^{-1} and C2=7.5 mg ml^{-1}), using line 1 of ultrafast spectroscopic set-up as shown in figure 6.3. All the sample have been excited at excitation wavelength (λ_{exc} = 350 nm) , using femtosecond Ti: S pulsed laser via SHG. A series of

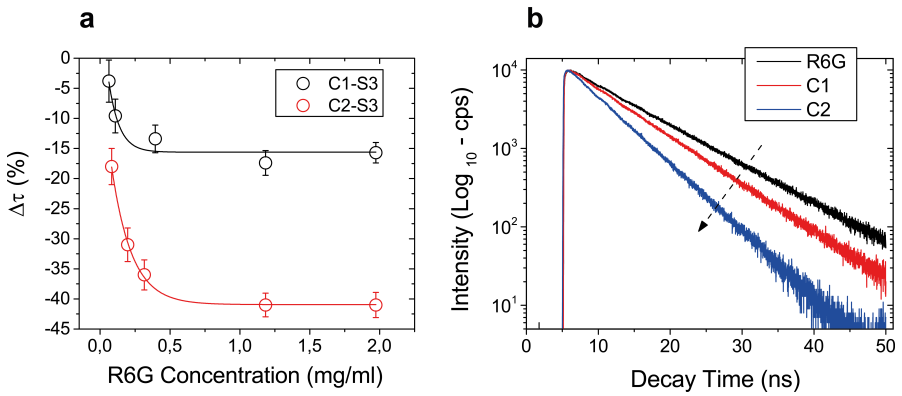

FIGURE 6.12: Percentage decreasing of the fluorescence life time vs dye concentration for two different concentration of mesocapsules (C1=1.25 mg ml^{-1}and C2=7.5 mg ml^{-1}). (b) life time for pure ethanol based R6G solution at concentration Cr=1.2 mg ml^{-1} (black line) and for two mesocapsule dispersions at concentration C1 (red line) and C2 (blue line) in an R6G solution (Cr = 1.2 mg ml^{-1}).

fluorescence life time measurements has been carried out in order to identify the optimal ratio between fluorophore and mesocapsule concentrations. Figure 6.12 (a-b) show a maximum reduction of the life time of the 41% in the case sample C2 at particular R6G concentration. Therefore the corresponding concentrations (C2 = 7.5 mg ml^{-1} for mesocapsules and Cr=1.2 mg ml^{-1} for R6G) have been used in all the subsequent experiments. Eventually fluorescence spectroscopy gives us the clear proof of a resonant energy transfer between gain and plasmonic medium.

6.2.6 Gain assisted mesocapsules as loss mitigated system

An ultra-fast pump-probe experiment for the simultaneous measure of Rayleigh scattering and transmission has been set up in order to demonstrate that gain-plasmon coupling in such system actually works as a loss-compensating mechanism. As it is already explained in the previous chapter, according to Beer-Lambert-Bouguer law, by measuring simultaneously Rayleigh scattering and transmission either in absence or in presence of pump, we are able to understand if the absorptive power of the material is affected by the gain presence. The experimental details are already described in figure 6.3 showing a sketch of the experimental set-up for pump-probe experiments. Femtosecond pulsed Ti:S laser has been used at particular wavelength ($\lambda = 700nm$), as an excitation source to pump after passing through SHG and excites R6G molecules at $\lambda_{exc} = 350nm$ and as a probe beam after passing through photonic crystal fiber (PCF) in order to generate supercontinuum light in the range 500-750nm. Broad-band enhancement of the

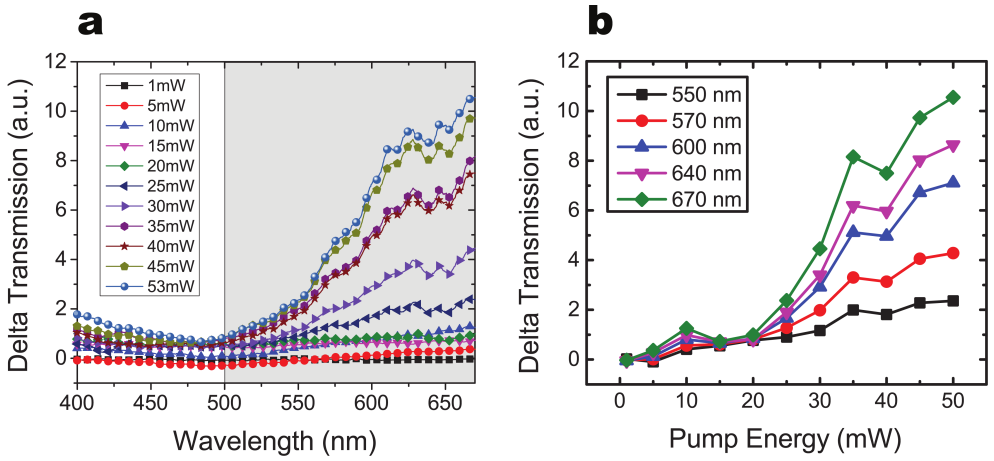

FIGURE 6.13: Measured percentage change of the transmitted broadband probe beam (a) by the mesocapsule gain assisted system as a function of pump energy. (b) Particular cuts of the previous curves for five different wavelengths of transmitted intensity as a function of pump power.

transmitted probe beam through the sample has been measured, while the scattering intensity of the probe beam seems to be unaffected by excitation energy. It shows a typical threshold value for the average pump power (about 20mW) above which a super-linear increase of the transmission was observed. In fact, the transmitted probe light rise up of an order of magnitude with respect the absence of the exciting field (pump pulses).

Moreover, the enhancement in transmitted probe beam as loss mitigated system has also been supported by simulation work which was done by *our theoretician colleague*. To support the experimental results, an analytical model based on Mie theory was realised [139]

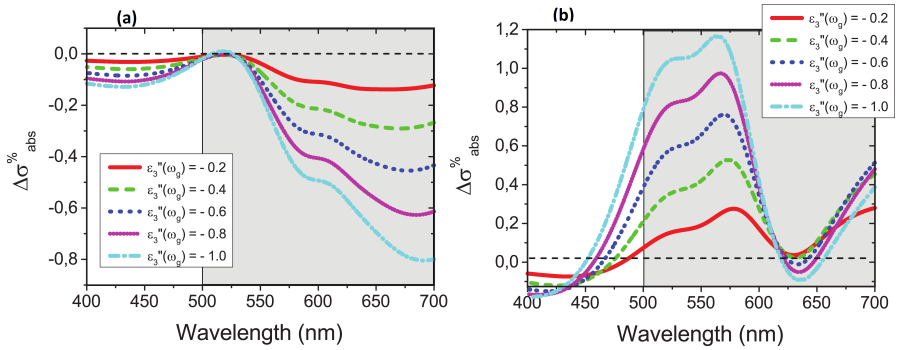

FIGURE 6.14: Calculated behavior for $\Delta\sigma^{\%}_{abs}$ for different values levels of gain ($\varepsilon_3''(\omega_g)$ from -0.2 to -1.0). (c) They are assumed to be both outside and in the core of mesocapsules; (d) Gain elements are assumed to be only outside the core of mesocapsules.

.

The results show that, if the presence of gain elements is supposed to be only outside the gold rich inner shell (namely diluted in ethanol or impregnated in the outer porous shell) no loss mitigation effects occurs (see figure 6.14b). In particular, the model predicts an increasing of the absorption cross-section in a spectral range below 550nm, and a reduction (even negative values) between 550 and 600 nm. On the other hand, if the gain is infiltrated in the hollow core, the absorption cross-section is broadband reduced (negative values), corresponding to a loss mitigation on a large spectral region (see figure 6.14a). This result is not surprising because, in the hollow core of the mesocapsule, the electric field is spatially uniform and consequently, the coupling is highly efficient for all the gain molecules present in this region, thus allowing for an effective loss mitigation. From these results, one can infer that, in the experiments, sufficient amount of gain molecules are infiltrated the hollow core of mesocapsules, emphasizing how important is to strategically position the gain in dependence of the geometry of the plasmonic structure.

Furthermore, it is known that the orientation of the dipole momentum of the gain elements plays a fundamental role in the optimization of the energy exchange [68]. As a consequence, being the gain elements present in our system dispersed in a solution, their dipoles momenta are free to reorient according with the electric field even inside the mesostructures. This makes these system much more efficient for loss mitigation purposes, than functionalized nanostructures in which the gain elements are embedded with random orientation within a solid dielectric host.

Chapter 7

Exciton-Plasmon Coupling in Macroscaled Systems

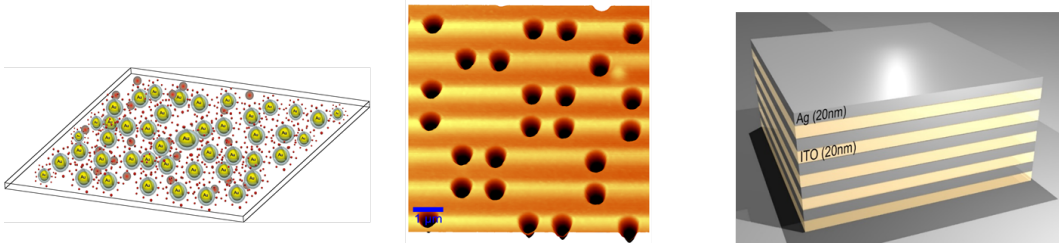

7.1 Dual Effect of Exciton-Plasmon Coupling in Hybrid Nanocomposite Films

7.1.1 Introduction

Exciton-plasmon hybrid systems demonstrate promising applications in light harvesting, sensing, plasmon mediated superluminescence, surface enhanced Raman scattering and sub-wavelength imaging beating the diffraction limit [4, 33, 140]. They are also expected to promote quantum effects such as electromagnetically induced transparency, cavity quantum electrodynamics, and photon blockade at normal experimental conditions such as room temperature and atmospheric pressure [141–143]. Several approaches have been implemented in order to study exciton-plasmon interaction, such as using DNA as spacer and placing QDs in close proximity of NPs by using

an atomic force microscope (AFM) tip [144–146]. To exploit exciton-plasmon interaction towards real applications, lot of efforts have been made to disperse QDs and plasmonic NPs in polymer matrices[147, 148]. However, metal losses affect the performance of all plasmonic devices and metamaterials in the optical range, making impossible to harness most of their fascinating properties for real life applications. Battling these absorptive losses will trace the future of plasmonic devices towards technological applications. Theoretical and experimental studies suggest that bringing gain close to plasmonic nanostructures can be a potential solution to solve optical losses issue [86, 89, 132, 133]. Gain-plasmon interaction also triggers other physical phenomena, such as super-absorption and enhanced photoluminescence (PL), along with mitigation of optical losses depending on inter-particle distance between gain media and metal nanoparticles (NPs) [47, 88, 149]. We already discussed gain assisted plasmonic systems at nano- and meso-scale in the previous chapters, where both gain encapsulated and gain assisted plasmonic structures have been dispersed in usual solvents [90, 94–96, 139]. This chapter explores the effects of gain-plasmon interaction, when QDs and Au-NPs are dispersed in a thick and flexible plastic matrix. Experimental evidences, such as fluorescence quenching, decrease of the overall quantum yield and modifications of fluorescence lifetimes confirm the presence of this strong coupling between plexcitonic elements. Measurements performed by means of an ultra-fast broadband pump-probe setup demonstrate a broadband mitigation of plasmonic optical losses of gold NPs dispersed in a plastic network in presence of gain. At the same time, a feedback mechanism induces a superabsorbing effect in QDs embedded in the same flexible matrices in presence of gold NPs. The close proximity of the two entities enables strong gain-plasmon coupling, stimulating non-radiative resonance energy transfer (RET) processes from excitons to plasmons and viceversa, in a sort of feedback mechanism. These RET processes from QDs to plasmonic nanoparticles are responsible for mitigating the metal optical losses, leading to a gain induced transparent system [90, 94, 96, 139, 150]. Moreover, the feedback effect, by acting in a reverse way, enhances QDs absorption cross section due to the presence of the strong plasmonic field generated in close proximity of metal NPs, [105] originating a super absorber behavior.

7.1.2 Synthesis and Fabrication of PDMS Nanocomposite Films Based on Au-NPs and QDs

The synthesis of donor core-shell CdSe@ZnS QDs and acceptor gold NPs is based on the fulfilling of some parameters, such as the overlapping between donor emission and acceptor absorption bands, and the homogeneous distribution of nano-objects in the host polymer. To satisfy the overlapping condition, sizes and functionalization of Au-NPs and QDs were properly performed. Spherical Au-NPs were synthesized by the addition of a solution of $HAuCl_4 \cdot 3H_2O$ dissolved in OA into a refluxing solution of OA and toluene . The particle growth was carried out at 110 °C for 120 minutes [151]. The Au-NPs, collected and purified with methanol from unreacted precursors, were finally dispersed in hexane. The average size of 11 nm for Au-NPs was confirmed by TEM characterization [152]. CdSe QDs cores were produced by disintegration of

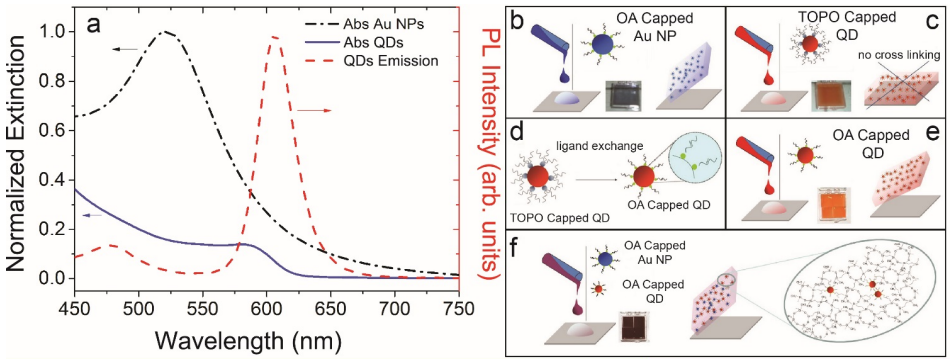

FIGURE 7.1: (a) The plasmon band of gold NPs (black dashed line), absorption of CdSe@ZnS QDs (blue solid line) and fluorescence emission spectrum (red dashed line) of CdSe@ZnS QDs, both in hexane solution. (b) Sketches of fabrication of nanocomposite films based on PDMS and Au-NPs, (c) as prepared (d and e) ligand exchanged CdSe@ZnS QDs, (f) the mixtures of Au-NPs and QDs [152].

organometallic precursors in hot coordinating solvents and then ZnS shell was grown over the cores [153]. In the next step of synthesis, an organic capping layer made of trioctylphosphine oxide (TOPO) and trioctylphosphine (TOP) was used to coat the QDs. As this organic layer contains the major fraction of TOPO, QDs will be entitled as "TOPO-coated QDs". The synthesized CdSe@ZnS QDs have their maximum absorption in solution around 561 nm (as shown in figure 7.1a). TEM analysis confirms the 3 nm size of QDs. Now, hybrid nanocomposite polymer films are fabricated by starting from the synthesis of Oleylamine (OA-) coated Au-NPs and CdSe@ZnS QDs of 11 nm and 3 nm in diameter, respectively, following the methods reported in these references [151, 153]. The elastomer was mixed thoroughly with the curing agent in the weight ratio of 10 : 1 and then degassed under vacuum to remove entrapped air bubbles. OA

capped Au-NPs (100μL, 3×10^{-6} M solution in hexane) and/or TOPO-capped and OA capped QDs (100μL, 6×10^{-5} M solution in hexane) were added to the pre-polymer mixture (2 g) and vigorously stirred for 1 hour to obtain a homogeneous mixture. The resulting mixtures were cast into a support template (2.5 cm x 2.5 cm) and the films were cured at 70 °C for 24 hour to obtain about 3 mm thick homogeneous, transparent and freestanding films. On the contrary, when colloidal emitting CdSe@ZnS QDs were

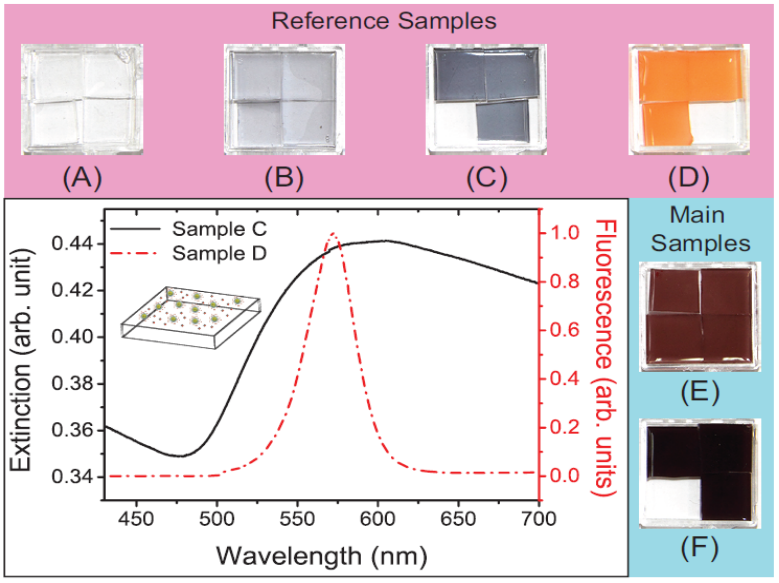

FIGURE 7.2: Images of the reference and main samples. Reference samples refer to pure (A) PDMS film, (B) low concentrated Au-NPs PDMS film (1×10^{-6} M), (C) higher concentrated Au-NPs PDMS film (3×10^{-6} M) and (D) QDs-PDMS film (QDs concentration = 6×10^{-5} M). Main samples E and F refer to the dispersion of same concentration of QDs with lower and higher concentration of Au-NPs in PDMS matrix, respectively. The plasmon band of sample C (black solid line) and fluorescence emission spectrum of sample D (red dashed line) are reported in the graph.

added into PDMS pre-polymer mixture, crosslinking of elastomer was not observed in the final films. Absence of crosslinking did not allow PDMS films to be free standing, homogeneous and transparent, even after a long thermal treatment. To overcome this hurdle, change in the QDs surface chemistry presented a promising solution to obtain the desired crosslinking mechanism [154, 155]. OA-capped QDs were successfully incorporated into the PDMS host by playing with nanocrystal surface chemistry, without changing the pre-polymer mixture composition or processing temperature, resulting in effective cross-linked and stable PDMS orange films [152, 154–156].

7.1.3 Experimental Evidences of Exciton-Plasmon Coupling

In order to confirm the gain plasmon coupling, several sets of experiments such as fluorescence quenching, time resolved spectroscopy and study of quantum yield in both hybrid nanocomposite films have been discussed here extensively.

7.1.3.1 Fluorescence quenching in hybrid films

Fluorescence quenching studies of QDs in presence of Au-NPs has been performed in order to confirm the presence of this strong coupling between excitons and plasmonic NPs in hybrid nanocomposite films. Samples D, E and F were excited at the same intensity by a pulsed laser at λ = 355 nm (Nd: YAG with 3ns pulse duration and 20 Hz of rep. rate). Inset of figure 7.3 shows the fluorescence emission quenching of both sample E and F with respect to sample D. We can notice that the emission quenching in

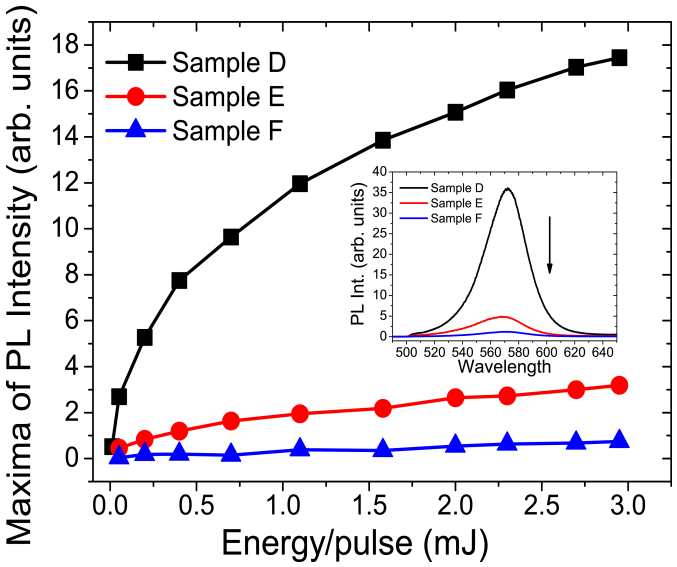

FIGURE 7.3: PL maxima of sample E (circular red dots) and sample F (triangular blue dots) with respect to sample D (square black dots) as a function of the incident pump energy. Inset shows the quenching of emission spectra of QDs in the presence of Au-NPs in sample E (red line) and F (blue line) with respect to sample D (black line).

sample F resulted more significant with respect to sample E, due to higher concentration of plasmonic nano-resonators. Moreover, observed emission quenching has also been reported as a signature of non-radiative energy transfer processes occurring from QDs to Au-NPs [90]. In order to elucidate this point, the maxima of PL intensity spectra of samples E and F are compared to that of reference sample (D) as a function of excitation energy. If QDs and Au-NPs are uncoupled, Au-NPs would act as a static quencher and

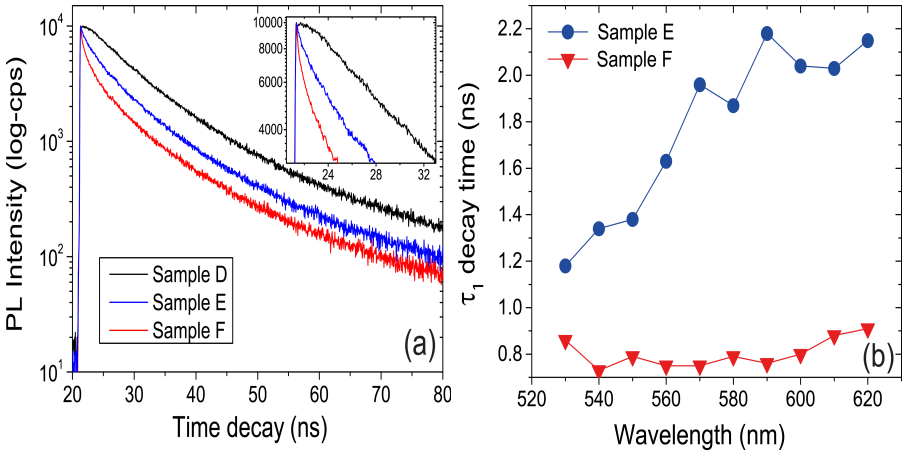

FIGURE 7.4: (a) Time-resolved fluorescence intensity decays for sample D (black solid curve), sample E (blue solid curve) and F (red solid curve). Inset shows the appearance of very fast time decay τ_1 in sample E and F with respect to sample D. (b) Shortened fast time decay τ_1 in sample F with respect to sample E at different emission wavelengths.

quenching rate must be constant as a function of energy [139]. Different rates have been instead observed for the two samples as shown in figure 7.3, confirming that a non-radiative RET process is at the basis of the observed quenching mechanism [90, 139].

7.1.3.2 Time resolved spectroscopy and Quantum yield measurements

Time-resolved fluorescence spectroscopy was carried out on both main samples (E and F), as well as on reference sample D, in order to study the time dependent behavior behind the exciton-plasmon coupling and RET processes. Figure 7.4(a) shows that all samples were excited at 370 nm by a femtosecond Ti:Sapphire pulsed laser (repetition rate = 4 MHz, pulse width = 140 fs, by Coherent Inc.), coupled to a second harmonic generator (SHG) module as shown in section 5.6.1. The emission wavelength was fixed at 570 nm in the spectrofluorometer (by Edinburgh Inc.). A bi-exponential fitting function is necessary to study the decay rate of QDs dispersed in PDMS due to the formation of QDs micro-aggregates into the plastic matrix [154]. In the presence of Au-NPs, three decay time components were observed in recorded time resolved data, introducing a shortest decay time (τ_1). This very short living state is attributed to the fraction of QDs which is located in close proximity with Au-NPs and take part in the non-radiative RET process via strong gain-plasmon coupling. Appearance of τ_1 clearly shows that fluorescence emission quenching of QDs in the presence of Au-NPs is related to a faster relaxation dynamics, due to the presence of a non-radiative channel, confirming a RET mechanism (see table 7.1) for details at emission wavelength of 570

nm). The intermediate lifetime (τ_2) is due to Forster resonance energy transfer (FRET) mechanism between the different sizes of QDs micro-aggregates. Life time τ_3 is originated from those agglomerates of QDs which did not participate in any kind of energy transfer processes. Moreover, shortest life time components (τ_1) related to sample E

Decay Time (ns)	Sample D	Sample E	Sample F
τ_1	–	1.96	0.75
τ_2	10.7	8.8	6.6
τ_3	45.6	38.5	28.5

TABLE 7.1: Decay lifetime for sample D, E and F in ns at emission wavelength 570nm.

and F as a function of emission wavelength were reported as shown in figure 7.4(b). A large variation in τ_1 is observed in sample E with respect to an almost constant behavior of sample F as a function of emission wavelength. This different behavior is attributed to the presence of a stronger exciton-plasmon coupling that generates a more efficient non radiative channel in sample F with respect to sample E [157, 158]. Moreover, In order to separate the radiative and non radiative contribution during the de-excitation process of QDs in the PDMS matrix, quantum yield measurements have also been used as an additional support to confirm stong coupling. The fluorescence quantum yield (ϕ_F) is defined as the ratio of the number of photons emitted through fluorescence and the number of photons absorbed. In order to measure QD quantum efficiency, sample A (PDMS matrix) was used as reference for sample D, whereas sample B and C were used as reference samples for sample E and F, respectively emission quantum yields of the PDMS films were obtained by means of a 102 mm diameter integrating sphere coated with Spectralon and mounted in the optical path of the spectrofluorometer. Significant decrease in QDs quantum efficiency was observed in both main samples. In particular, sample E presented a decreasing of quantum efficiency of 20 times, from 16.5% to 0.8%, whereas for sample F a reduction of about 40 times, from 16.5% to 0.4%, was measured [152, 159]. Quenching in quantum yield confirms non radiative energy transfer from QDs to Au-NPs via the strong resonant coupling between excitons and plasmons.

7.1.4 Significance of Strong Coupling in Hybrid Nanocomposite Films

The above experimental evidences confirm the presence of a strong coupling between ODs and Au NPs in hybrid nanocomposite films. Noteworthy, this strong coupling

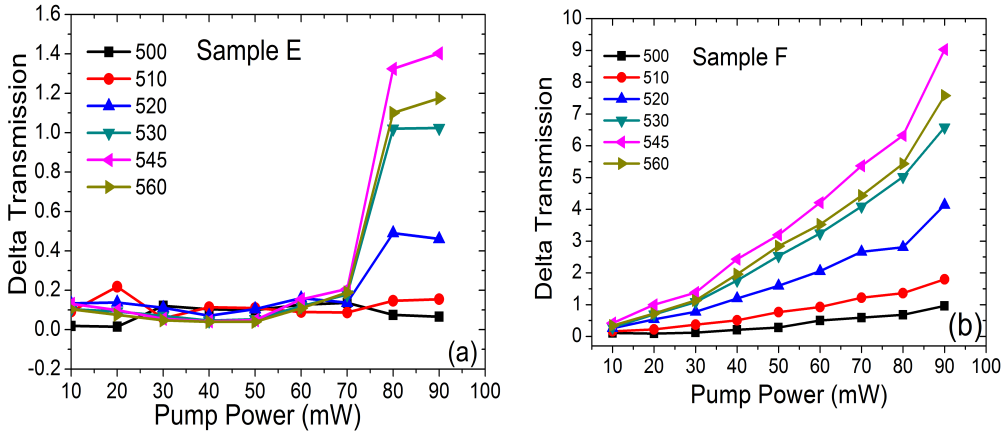

FIGURE 7.5: (a) Particular wavelength cuts extracted from broadband Δ_T of sample E in the spectral overlapping region of plasmon resonances and QDs emission as a function of pump power, when excitation wavelength $\lambda_{exc} = 400nm$. (b) Particular wavelength cuts extracted from broadband Δ_T of sample F for the same probe wavelengths.

completely modifies the optical behavior of the system. As discussed above and in previous chapters, non-radiative energy transfer process from QDs to Au NPs mitigates the optical losses of the plasmonic system. Furthermore, the enhancement in the absorption cross section of QDs was observed due to enhanced plasmonic field around NPs as a feedback effect via plasmonic NPs to QDs. This subsection of the chapter describes the both observed effects in the hybrid nanocomposite films.

7.1.4.1 Optical loss mitigation in plexitonic hybrid systems

Ultrafast broadband pump probe experiment has been performed to measure simultaneously transmission and Rayleigh scattering of hybrid films as described in section 6.1.3. This will be the proof that RET processes are also responsible of optical loss compensation mechanisms. Setup consists of a Ti: Sapphire pulsed laser (same characteristics of above), tunable in the $680 - 1080$ nm range, that allows an infrared light beam to pass through a $30 : 70$ beam splitter. 70 % of the beam is sent to the SHG module, used to duplicate the excitation wavelengths in the range of $340 - 540$nm. Remaining fraction of the beam is used to generate super continuum light from a nonlinear photonic crystal fiber, to obtain a probe beam with a broadband distribution ($500 - 1000$nm). Pump and probe beams are coupled by means of a beam coupler (BC) and incident on the 3D sample holder.

Beer-Lambert-Bouguer law states that simultaneous measurements of Rayleigh scattering and transmission, either in the absence or in the presence of an excitation, allows to understand if the absorptive power of the system is affected by the gain presence. Delta transmission Δ_T is defined as $(I_p - I_o)/I_o$, where I_p and I_o are the transmitted probe light in the presence and in the absence of gain. It is clearly evident from figure 7.5(a), sample E only shows transmission enhancement for the higher pump power exhibiting thersold value at higher pump power (70 mW) due to weaker exciton plasmon coupling. On the other hand, strong exciton-plasmon coupling takes place in the case of sample F with respect to Sample E. Sample F shows the linear enhancement in transmission after attaining thersold at (10 mW). Δ_T remains almost constant as a function of pump power for 500nm probe wavelength which is out of spectral overlapping of plasmon band of Au-NPs and QDs fluorescence emission for the both samples. ($\lambda_{exc} = 400nm$). But, Δ_T increases gradually as the wavelengths inside the spectral overlapping region are probed in sample F, as shown in figure 7.5(b). Such behavior remains absent in sample E. An enhancement of almost an order of magnitude in transmitted probe light through sample F has been observed for 545 nm probe beam. Rayleigh scattering remains constant for the both sample E and F at all excitation powers. Delta transmission enhancement clearly explains how non-radiative RET processes from excitons to plasmons induce a transparency in the film [95, 139].

7.1.4.2 QDs absorption cross-section enhancement in plexitonic hybrid systems

In order to demonstrate that the feedback mechanism causes the appearance of the dual effect behind the strong exciton-plasmon coupling between QDs and Au-NPs, the super-absorber nature of excitons in sample F has been investigated. Lawandy reported the enhancement in the near field of plasmonic NPs, when surrounded by an optimal amount of gain media [18]. QDs strongly coupled to Au-NPs increase their absorption cross section in the vicinity of enhanced plasmonic local field as a feedback mechanism [103, 160].

The extinction cross section enhancement is dominated in the overlapping region of QDs emission and NPs plasmon band as shown in figure 7.6. Presence of Au-NPs in the vicinity of QDs in sample F enhances the absorption cross section of excitons in an unusual way. In fact, this effective overlapping leads to an effective coupling between QDs and Au-NPs, creating a strong resonance that causes the occurrence of a modified plasmonic local field which interacts with QDs and modifies their absorption

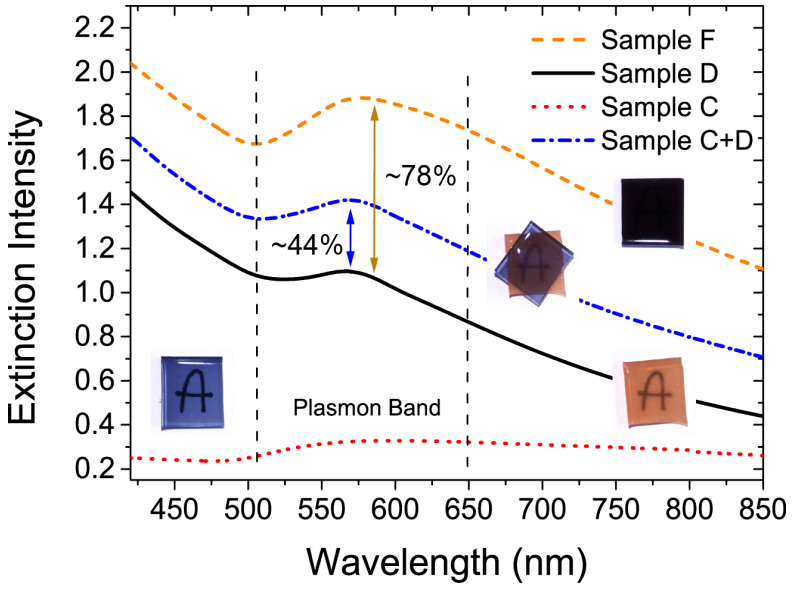

FIGURE 7.6: Extinction curves for sample D (black solid line), sample C (red dotted line) and sample F (dark golden dashed line). The mathematical sum of extinction curves of sample C + sample D (blue dashed line). The images correspond to the real fabricated PDMS films over a letter "A" written on a white paper.

and emission properties [103]. The extinction cross section enhancement resulted more pronounced in the overlapping region of QDs emission and NPs plasmon band. Quantitatively, the mathematical sum of extinction curves of sample C and D corresponds to an increase of only 44% inside the plasmon band, while in the case of the hybrid nanocomposite plastic film containing both subunits (F), the enhancement is about 78%. Super absorbing nature of sample F is clearly observed by naked eyes, when it becomes almost impossible to distinguish the letter "A" through it.

7.2 Enhanced Transmission and Cavity Modes in Thue Morse Patterned Plasmonic Nanocavities

7.2.1 Introduction

Controlling photons in the same way as electrons in materials envisages about unique and novel technology, which can realize the thousand times faster devices than ones exist in present. Noteworthy, integration of modern electronic devices for information processing and sensing is rapidly approaching its fundamental speed and bandwidth

limitation [161]. In such scenario, surface plasmons (SPs) are the hope as the light signal can be concentrated and channeled using subwavelength structures. Such circuits would convert light into SPs, then can propagate and will be processed by logical elements, before being converted again into light [26]. As it is already described in chapter 2.6, propagating surface plasmons are known as surface plasmon polaritons (SPPs), which may lead to the localization of guided light signals beyond the diffraction limit along metal–dielectric interfaces. This strategy is quite efficient to concentrate light at nanoscale level.

It is also well known that SPPs require an additional momentum in order to couple with metal-dielectric interface, which can be provided using techniques such as prism coupling, gratings and periodic array of holes [27]. Moreover non-periodic and quasi periodic structures are also capable to offer missing momentum by exciting the localized surface plasmon modes, when the sub-wavelength structural elements are illuminated [28]. Nano-holes arrays patterned in metallic thin films have become center of attraction and core elements of optical devices, when Ebbesen et al. successfully challenged the Bethe's calculated transmitted efficiency through sub-wavelength nanoholes and demonstrated that orders of magnitude of more light as compared to Bethe classical approach could be transmitted through holes [162]. This phenomenon changed the direction of fundamental research and can be considered the rebirth of surface plasmons, opening up numerous novel applications in various inter-disciplinary fields such as nano-photonics, chemical sensing, waveguiding, wavelength filters, light concentrator in sub-wavelength region and biosensing [26, 28, 163]. Furthermore, plasmonic quasi-periodic structures demonstrate several advantages over periodic structures. Due to periodicity and short range order in plasmonic crystals, the excitation of SPPs depends on specific polarization and launch angle. Coupling of light at different excitation wavelengths requires number of Fourier components, which are not present in periodic structures [164]. On the other hand, quasi-periodic structures offer large number of Fourier components and are efficient to excite polaritons at different angles [165].

Here, long-range ordered thue morse patterned plasmonic nanocavities have been fabricated by patterning naho-holes in polymer films using Electron Beam Lithography (EBL) and depositing gold above the obtained structures. Different diameters (D) of quasi-crystals have been chosen in such a way that nanocavities appear sub-wavelength (D = 400 nm), wavelength comparable (D= 500 nm) and Mie approximated type structures (D = 750 nm) in the context of excitation wavelength (λ_{exc} = 532 nm). We demonstrate the enhanced transmission in sub-wavelength nanocavities and even image it by

using Scanning Near-field Optical Microscopy in transmission mode. SPPs propagating on the both sides of gold film, couple with localized surface plasmon modes of individual nanocavities and transmit through nanocavities [166, 167]. Furthermore, we observe the different localization of light in terms of cavity modes when nanocavities of different diameters are illuminated with particular polarization and analyzed at different angles. Noteworthy, plasmonic nanocavities also exhibit dissipative losses due to metallic nature which dissipate plasmon propagation length. Incorporation of gain to nanocavities has been intended in order to enhance this propagation length in future, but clear understanding of the propagating modes in such structures is mandatory before gain inclusion.

7.2.2 Fabrication of thue morse patterned plasmonic nanocavities

Quasi-periodic plasmonic nanocavities with different radii, have been fabricated by our Naples collaborators. Electron Beam Lithography (EBL) on a 15nm ITO coated glass, thermal evaporation of 60 nm thick Au layer, and a lift-off process yielded a nanopatterned substrate. 200 nm thick ZEP (Marubeni) positive resist was structured by using a

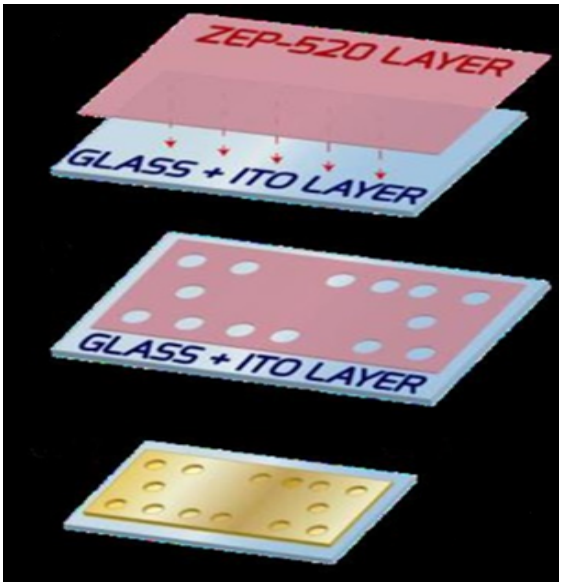

FIGURE 7.7: Sketch for the realization of plasmonic nanocavities, initiating the process with deposition of 200nm thick polymer film on ITO coated glass substrate, pattering of holes in polymer and 60 nm Au evaporation

10 keV electron beam (Raith 150) and subsequently developed. Au was then thermally evaporated on the nanostructured substrate with a RAVA system. No adhesion layer was used between Au and glass.

7.2.3 Enhanced transmission through plasmonic nanocavities

Zero order transmission spectra were recorded for all the plasmonic structures with an incoherent light source with collinear incident and transmitted light. Figure 7.8 (a) shows the observed transmission spectra for 400 nm, 500 nm and 750 nm diameter sized nanocavities. All the curves show a common peak around 500 nm wavelength which is attributed to intraband transition and is an inherent property of gold [168]. The second transmission peak observed in subwavelength nanocavities (D = 400 nm) can be explained clearly as the enhanced transmission which occurs due to the coupling of SPPs with localized surface plasmon modes [166, 169]. One can argue on the observation of only one additional peak with respect to numbers of peaks observed as the signature of extra ordinary or enhanced transmission in literature [162]. Here is noteworthy that transmission peaks strictly depend on periodicity, hole diameter, thickness and metallic nature of film. Wang et al. showed how intensity of transmission peaks decreases and shift towards infrared wavelengths, when holes arrays in the film are changed from periodic to quasi-periodic ones [170].

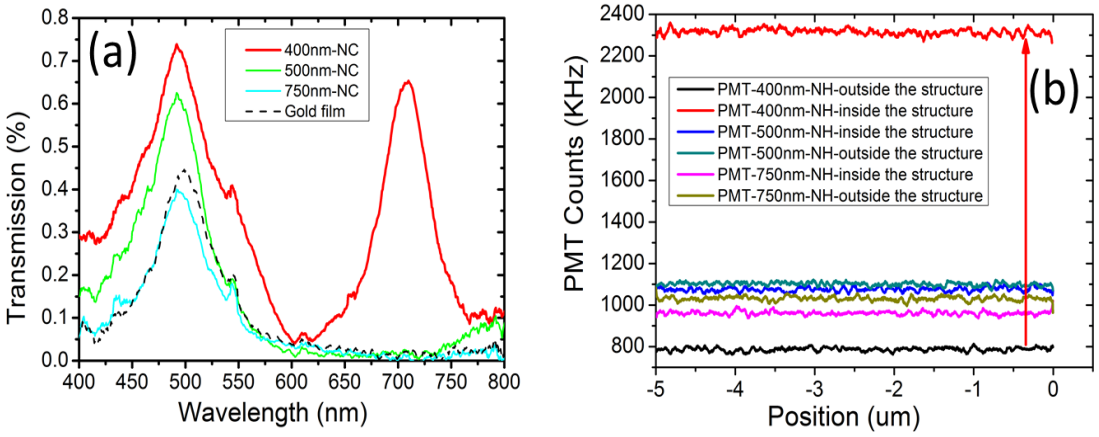

FIGURE 7.8: (a) Zero order transmission through different sized nano-cavities (inside the structure) and gold film (outside the structure). (b) Transmission through the same nanocavities in terms of PMT counts by means of confocal analysis in transmission mode

Furthermore, in order to support these results, confocal analysis has been performed on the structures. WITec Alpha 300S Scanning Near Field Optical Microscope (SNOM) has been used in confocal transmission mode to focus same energy and polarization of excitation laser light ($\lambda_{exc} = 532nm$) inside and outside (plain gold film) the nanocavities by means of continuous laser. Excitation laser beam is incident on the samples through top 100x objective (0.75 numerical aperture (NA)), and is collected by bottom 50x objective (0.5 NA) and sent to a photomultiplier tube (PMT). Figure 7.8(b) shows 3

times enhancement in PMT counts, when sub-wavelength structures (D = 400 nm) are illuminated with respect to plain gold film, using the same laser energy. As PMT is very sensitive detector of light, transmitted signal can be considered almost in terms of PMT counts for other structures, when illuminating inside and outside the structures.

7.2.4 Scanning Near Field Microscopy (SNOM)

WITec Alpha 300 microscope is a powerful instrument which can be used as confocal, Atomic Force Microscopy (AFM) and scanning near field optical microscope (SNOM) in different operational modes. SNOM enables to image beyond the far-field visible diffraction limit with the capability of performing high spatial resolution. Optical microscopy has been used in various interdisciplinary fields such as cell biology, microelectronics, watch making and many more. The resolution of optical microscopy is limited to approximately half the wavelength of light, which prohibits the investigation at nano and molecular scale. In 1873, Ernst Abbe reveled that the maximum resolution for an optical microscope depends on focusing of light beam . At the focal point, the focused light forms a diffraction pattern consisting of concentric circles. This diffraction pattern is the smallest unit in image formation. Abbe used the spacing between the concentric rings to calculate Rayleigh diffraction limit [171].

$$d = \frac{0.61\lambda}{NA} \tag{7.1}$$

where λ is the wavelength of light and NA stands for numerical aperture of the focusing objective. E. H. Synge proposed the idea of using a small aperture to image a surface with sub-wavelength resolution using optical light. For the small opening, he suggested using either a pinhole in a metal plate or a quartz cone that is coated with a metal except for at the tip [171]. Meanwhile, J.A. O'Keefe, a mathematician also proposed the concept of Near-Field Microscopy without knowing about Synge's earlier work. However, he addressed the practical difficulties of near field microscopy.
But, in 1980, Binnig and Rohrer invented scanning tunneling microscope (STM) which was able to control a metallic tip within Angstroms from a conducting surface and scan the tip across the sample generating atomic-scale topographic images. STM was able to overcome the optical diffraction limit by using electrons and the principle of quantum tunneling. Due to nanometer precise control and vibration isolation methods catalyzed

by STM, Synge's proposal became a reality when Ash and Nicholls demonstrated feasibility of NSOM using microwaves. The first demonstration of sub-diffraction limit resolution was shown by Aaron Lewis and co-workers at Cornell and Dieter Pohl's lab at IBM Zurich in the mid 1980s, when methods were developed for fabricating sub-wavelength probes [172].The acronym NSOM was proposed by Lewis but the technique is also called scanning near-field optical microscopy (SNOM). Thus, the samples are ex-

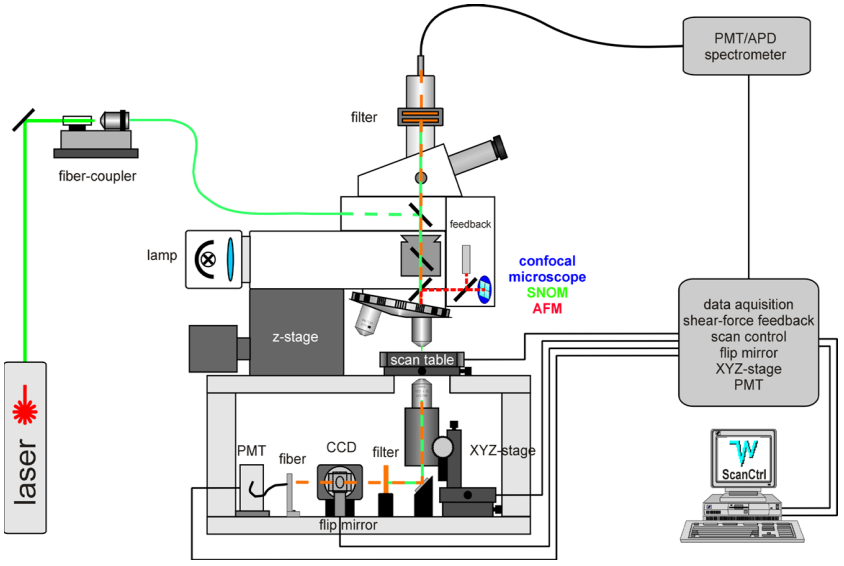

FIGURE 7.9: Schematic and beam path of the WITec Alpha 300 SNOM instrument for confocal, AFM and SNOM configurations.

cited through nanometer sized point sources so called tips, which are able to sense near field radiation and to collect the high frequency radiation from the sample encoded in the evanescent waves. Then, such near field waves are sent to far-field detector. Figure 7.9 shows the beams paths for confocal, AFM and SNOM configurations in transmission mode. SNOM can be performed on both conducting and insulating surfaces unlike STM, which can also only be used on metallic films. Along with high resolution spatial, SNOM can be used to perform local spectroscopy including surface enhanced raman scattering (SERS) and life time fluorescence imaging.

7.2.5 Imaging enhanced transmission and polarization dependent cavity modes in nanocavities

In order to investigate enhanced transmission and cavity confined modes, WITec Alpha 300 SNOM uses top objective 20x 0.75 NA, which focuses the excitation laser beam ($\lambda_{exc} = 532nm$) on the plasmonic structures through a metallic nano sized (less than 90 nn) tip. The produced signal is collected by bottom objective 50x 0.75 and referred to PMT. Figure 7.10(a) and (b) show the topographic and optical near field images of

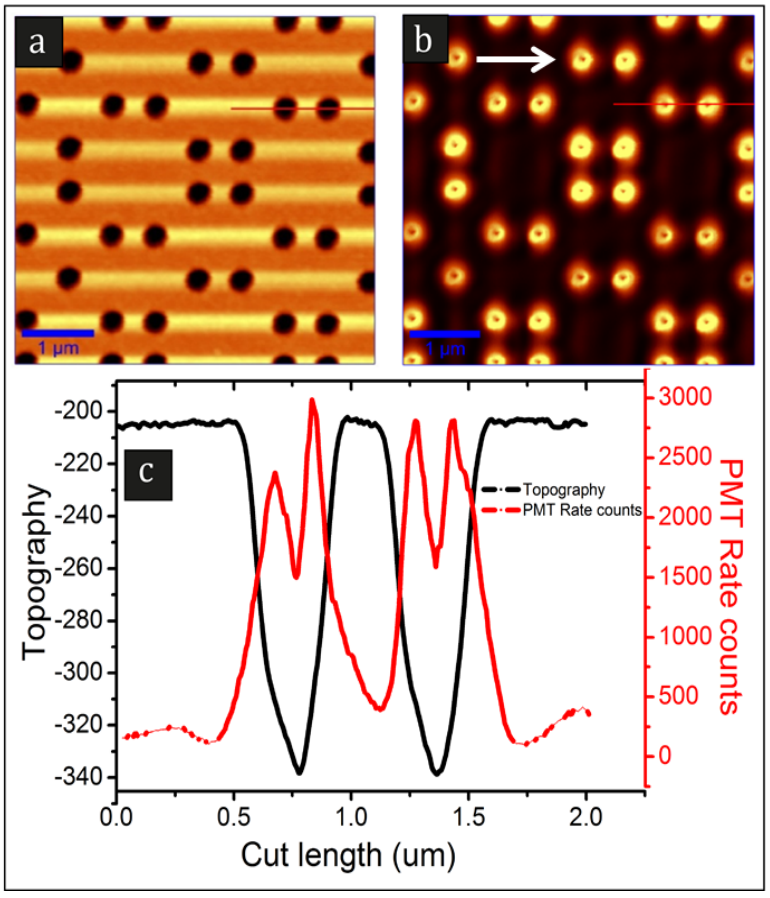

FIGURE 7.10: (a) Topography of subwavelength (radius R = 200 nm) thue morse patterned nanocavities. (b) Corresponding SNOM image to topographic one of quasi periodic nanocavities as shown in (a) White arrow in the SNOM images shows the polarization of excitation laser beam. (c) Topography and SNOM line profiles of 200 nm radii nanocavities along horizontal red lines drawn on topographic and SNOM images.

sub-wavelength plasmonic nanocavitiesin transmission mode. White arrow refers the direction of polarization which is X-polarized as shown in figure 7.10(b). It is clearly evident that SPPs propagate on the metal dielectric interface and couple to localized surface plasmon modes and transmit through corners of nanocavites, enhancing the PMT

counts in terms of enhanced transmission [166, 168]. The sharp drop in PMT counts inside such nanocavities as shown in figure 7.10 (c) has been justified because excitation laser beam ($\lambda_{exc} = 532nm$) can not interact and excites SPPs on inner metal-air interface due to sub-wavelength sizes of plasmonic nanocavities. Noted we observed the same near field image, when the nanocavities are excited with Y-Pol, but not shown here.

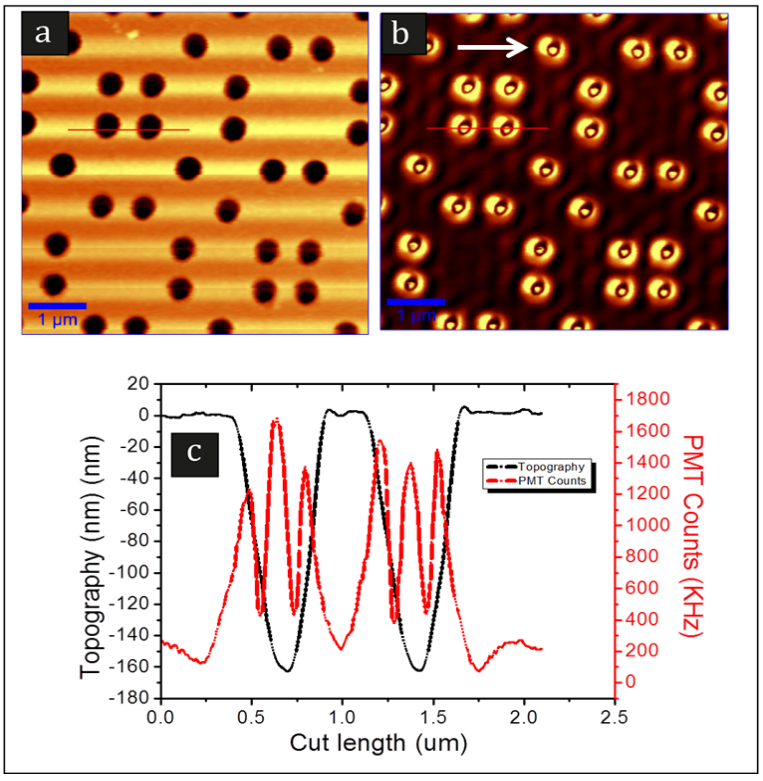

FIGURE 7.11: (a) Topography of thue morse patterned nanocavities with diameter D = 500 nm . (b) Corresponding near-field image to topographic one of quasi periodic nanocavities as shown in (a). (c) Topography and SNOM line profiles of 500 nm diameter nanocavities along horizontal red lines drawn on topographic and SNOM images.

Following the same experimental procedure, 500 nm diameter sized nanocavities are illuminated by X- polarized light. This time, SNOM tip is able to interact with metal-air interface and allows the excitation of SPPs without any possibility of propagation due to cavity. Park et al. theoretically studied the case of nano-holes in thin film and showed excitation of SPPs at various metal dielectric interfaces and localized surface plasmons lead to plasmon hybridization in the nano-holes, which strictly depends on diameter of holes and thickness of film [173]. Same phenomenon takes place in our samples, when the localization of light in terms of cavity modes is attributed to hybridization of localized surface plasmon modes and excited SPPs at various metal dielectric interfaces such as metal-dielectric interfaces inside and outside the nanocavities on the upper side

as well as underlying side.

Thus, plasmon hybridization depends on diameter of nanocavities and the thickness of metal film. Figure 7.11 shows particular cavity modes in 500 nm diameter thue-morse patterned plasmonic cavities. The mapping of SPPs can be seen in figure 7.11(b) and can be understood how hybridization takes place.The nanocavities are illuminated with three intense modes as shown in 7.11 (c).

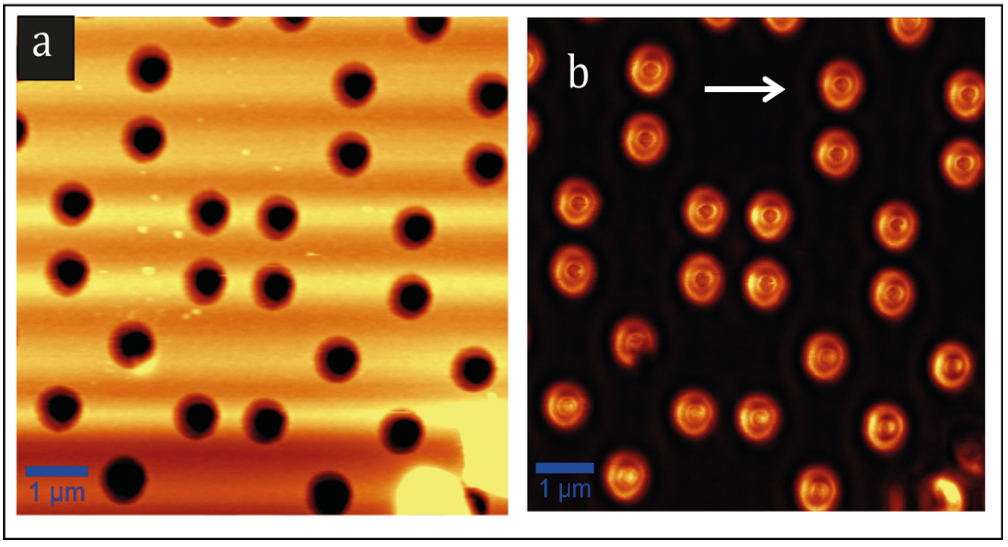

FIGURE 7.12: (a) Topography of thue morse patterned nanocavities with diameter D = 750 nm . (b) Corresponding near-field image to topographic one of quasi periodic nanocavities as shown in (a), when excited by polarization-X.

Figure 7.12 shows the present cavity modes and topographic images in 750 nm diameter nanocavities. Such cavity modes are referred to Mie approximated type modes as the radius of cavities are lesser than excitation wavelength ($R < \lambda$). Lacharmoise et al. reported the observation of single ring type modes in periodic Mie approximated sized nanovoids (R= 300 nm) under excitation of green laser beam [174]. Here, we observed the two ring type modes as an outcome of redistribution of electromagnetic modes due to cavities diameter dependent plasmon hybridization as shown in figure 7.12.

Moreover, when an analyser (a polarizer placed in the beam path of detected signal before PMT) is added in the optical path, it is possible to perform measurements by acting on excitation and output polarization. In case of an excitation polarizer in X (Pol-X) and crossed analyzer, Mie approximated sized structures are able to produce quadrupole modes as shown in figure 7.13. Day et al. showed the rise of quadrupole modes due to hybridization-based coupling of nanowire plasmon modes with nano-antenna structure, mediating an interaction between the nanowire plasmon modes themselves [175].

In the end of the section, we would mention again that all the results have been shown

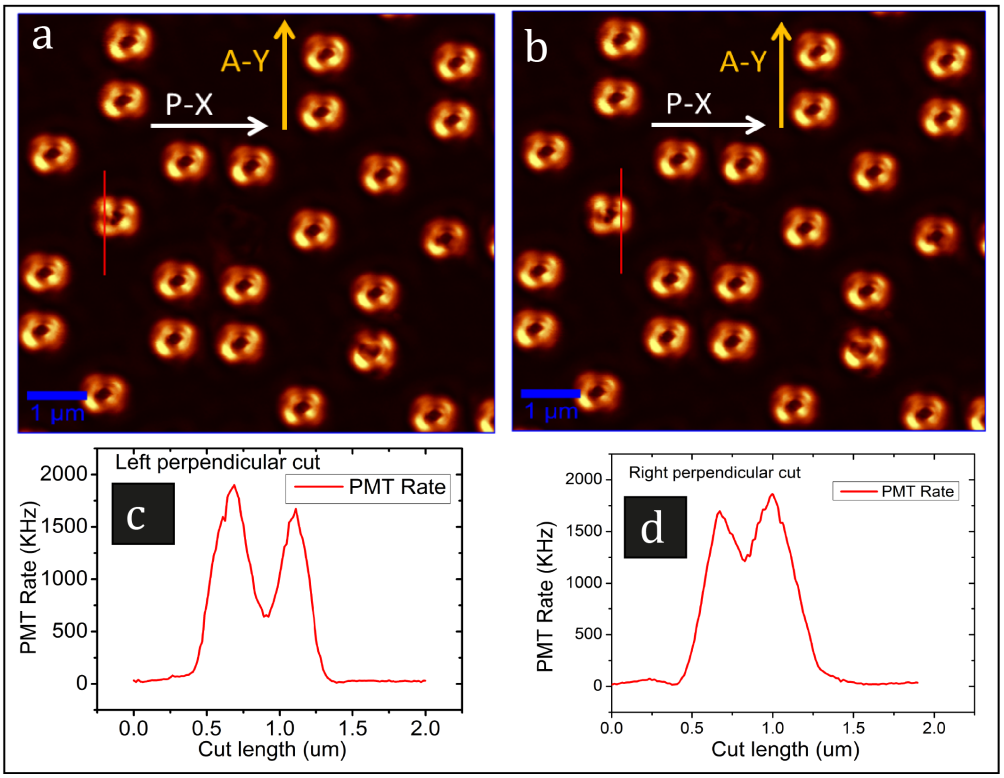

FIGURE 7.13: (a) and (b) SNOM images of 750 nm diameter nanocavities referring left and right perpendicular cut with red line, respectively. (c) and (d) SNOM line profiles of left and right perpendicular showing the observation of quadrupole modes, respectively.

here in order to understand the intrinsic behavior of quasi periodic nanocavities. Incorporation of gain in the structures is expected to enhance SPPs propagation length, which will affect plasmon hybridization in the systems and eventually distribution of electromagnetic modes. This project will be completed in next year.

7.3 Experimental Realization of Simultaneous Type I/Type II Hyperbolic Metamaterials

In the last period of my PhD program, I also participated in the experimental realization and characterization of very particular anisotropic structures called *Hyperbolic Metamaterials*.

7.3.1 Variable angle spectroscopic ellipsometer (VASE)

VASE is based on ellipsometry principle and has been used to extract optical parameters and determine the thickness of silver and ITO layers. Ellipsometry is a non-destructive optical technique to investigate the dielectric properties (complex refractive index or dielectric function) of thin films. Ellipsometry uses the fact that linearly polarized light at an oblique incidence to a surface changes polarization state, is reflected, it becomes elliptically polarized.It is very sensitive to the change in the optical response of incident radiation that interacts with the material being investigated. An ellipsometer measures

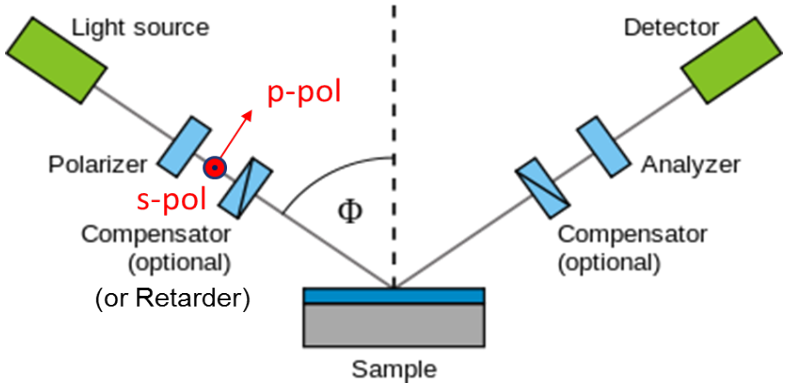

FIGURE 7.14: General working principle of ellipsometry

the changes in the polarization state of light when it is reflected from a sample. If the sample undergoes a change, for example a thin film on the surface changes its thickness, then its reflection properties will also change. Measuring these changes in the reflection properties can allow us to deduce the actual change in the film's thickness. Since the general polarization state of polarized light reflected from a surface is elliptical, the term ellipsometer was chosen. Ellipsometer measures the complex reflectance ratio ρ of a system, which may be parametrized by the amplitude component ψ and the phase

difference Δ, relating in such a way

$$\rho = tan(\psi)e^{i\Delta} = \frac{R_p}{R_s} \tag{7.2}$$

here, R_p and R_s are Fresenel reflection coefficients for p- and s-polarized light. Ellipsometer can be used to characterize composition, roughness, thickness (depth), crystalline nature, doping concentration, electrical conductivity and other material properties.

The thickness of the silver and ITO layers have been confirmed by performing a spectroscopic scan. Ellipsometric parameters such as Ψ and Δ have been measured and fitted by using an appropriate optical model, to retrieve the values for n and k for each Ag and ITO thin films

7.3.2 Inversion point of coexisting anisotropies in Ag/ITO HMM

In chapter 2, it was discussed that the two different types of geometries, which act as an extreme anisotropic metamaterial, showing completely opposite behavior such as metal nanowire arrays embedded in a dielectric matrix as Type I HMM and metal-dielectric periodic stacks as type II HMM. Shekhar et al. theoretically reported a multilayer system presenting both the anisotropies, either separated by a dielectric gap or adjacent each other, showing that an experimental result with a simultaneous type I/type II behavior at the same frequency in the visible range would be not easy to achieve [56].

According to extended effective medium theory for low losses

$$Re(\tilde{\varepsilon}_{\parallel}) \cong \frac{\varepsilon_1^d L_d + \varepsilon_1^m L_m}{L_d + L_m} \tag{7.3}$$

$$Re(\tilde{\varepsilon}_{\perp}) \cong \frac{\varepsilon_1^d \varepsilon_1^m (L_d + L_m)}{L_d \varepsilon_1^m + L_m \varepsilon_1^d} \tag{7.4}$$

where subscript 1 refers to real parts of ε^m and ε^d, that are the permittivities of metal and dielectric, as L_d and L_m are their thicknesses, respectively. An epsilon near zero and pole (ε_{NZP}) HMM, which simultaneously shows $\varepsilon_{\parallel} \approx 0$ and $\varepsilon_{\perp} \approx \infty$ can be designed by choosing particular conditions such as $L_m = L_d$ and $\varepsilon_m = -\varepsilon_d$ in the above equations. Due to its low losses at visible frequencies, silver has been used as metal, while ITO (Indium Tin Oxide) constitutes an interesting alternative to a common dielectric, due to its wide utilization in everyday technology, fabrication processes and transparency in most of the visible range and suitably high refractive index. For all these reasons we

focused our attention on a ITO/Ag pair. As a first step, 20 nm thick layers of ITO and Ag have been alternatively deposited on a glass substrate up to 5 bilayers, by means of a sputtering technique. Figure 7.15(a) demonstrates a sketch of HMM made of 5 bilayers

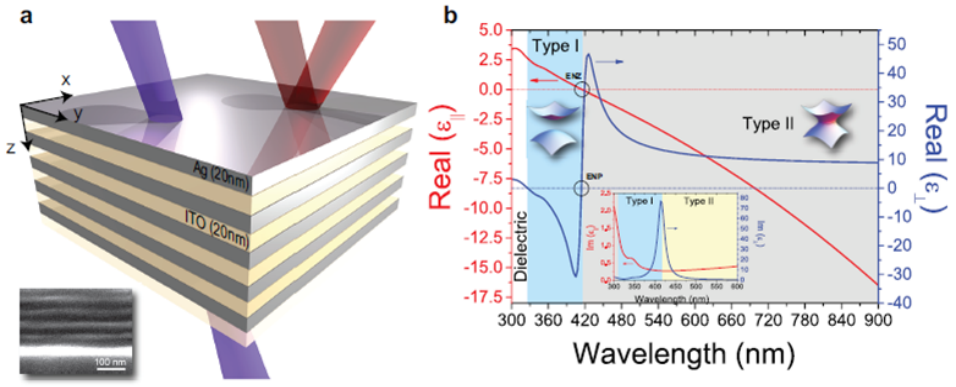

FIGURE 7.15: (a) Sketch of the obtained HMM structure made of 5 bilayers of Ag (20nm) and ITO (20nm). The two laser beams in the sketch represent the different behavior of the obtained material, that is almost transparent in the UV range, whereas is reflective above 450nm. Inset shows SEM image of the transversal section of the obtained sample. (b) Effective Medium Theory (EMT) of an ITO/Ag multilayer. Real part of epsilon parallel (red curve) and epsilon perpendicular (blue) of the entire structure. In the inset we present the imaginary parts of parallel and perpendicular permittivities. It is evident that the type I/type II transition wavelength occurs at 414nm.

of Ag (20nm) and ITO (20nm). Inset of figure 7.15(a) shows a Scanning Electron Microscopy (SEM) image confirming the obtained layer by layer disposition with a fill fraction of almost 50%. Figure 7.15(b) shows that medium behaves as a dielectric up to 327 nm because both $\varepsilon_{\|}$ and $\varepsilon_{\perp}$ are positive. While The structure opens a *type I* - HMM window in the wavelength range between 327 nm and 414 nm, exhibiting $\varepsilon_{\|} > 0$ while $\varepsilon_{\perp} < 0$. At $\lambda = 414$nm the ε_{NZP} behavior clearly shows a strong discontinuity in $\varepsilon_{\perp}$, passing from a very high negative value (virtually $-\infty$) to a very high positive one (virtually $+\infty$) while, simultaneously, $\varepsilon_{\|} = 0$. Inset of figure 7.15(b) shows the imaginary parts of $\varepsilon_{\|}$ and $\varepsilon_{\perp}$ which are plotted in orde to show a very sharp Lorentzian shape for $\varepsilon_{\perp}$, peaked exactly at the transition wavelength. HMM exhibits a *type II* behavior at $\lambda > 414$nm.

Chapter 8

Conclusions

In conclusion, we successfully demonstrated a multiscale strategy to tackle absorptive losses in the different metasubunits. Incorporation of gain in the close proximity of plasmonic structures leads to strong excition-plasmon coupling and enables non-radiative energy transfer process from gain media to metallic NPs, which mitigates the absorptive losses in the gain functionalized plasmonic systems. We followed across scales approach from dispersed nanoscale level to bulk macroscale towards the realization of gain incorporated bulk plasmonic devices and studied the following plexitonic systems.

Nanoscaled gain functionalized monomers and multimeric structures

The exciton–plasmon interplay in monomers and multimers of gain functionalized multishell nanostructures with different silica shell thickness (10 and 30 nm) has been investigated. These nano-composite systems permitted a systematic investigation of the RET process between excitonic molecules and localized plasmons as a function of NP configurations and spacer thicknesses. Time resolved fluorescence spectroscopy allowed us to investigate a remarkable resonant coupling difference between monomers and multimers. The obtained results, in combination with steady-state measurements, demonstrate that multimers experience a more effective exciton–plasmon RET because of the enhancement of the local field related to plasmon hybridization effects. Moreover, our results show that reducing the silica shell thickness results in a better coupling strength not only between exciton and plasmon, but also between NPs in a multimeric configuration, as evidenced by significant changes of fluorescence decay times. In fact, the observed enhancement of Rayleigh scattering and transmission above a critical value of gain, in correlation with inter-particle distance, have demonstrated the magnification of the local plasmon field of the gain functionalized nanostructures and the increasing of their optical transparency in the presence of fluorescent molecules.

Mesoscaled plasmonic nanoshells

Gain functionalized plasmonic nanoshells demonstrate existance of different coupling configurations between plasmons and excitons, depending on the relative positions of their bands. In fact, in the case that the emission band of fluorophores is properly overlapped to localized surface plasmon band of adequate plasmonic units (i.e. gold nanoshells), non radiative resonant energy processes occur within the dye functionalized nanoshell. This photo-physical process clearly induces a relevant reduction of the effective absorption cross-section of the plasmonic system as function of the provided gain, but it occurs selectively within the optical loss compensated band (630-750nm). Because of the modified emission band in presence of thin gold shell, a second plasmon-exciton interplay effect has been observed, namely an increasing of the absorption cross section in the nearby spectral region (510-630nm). This double strong coupling resulted in a frequency dependent behavior of the dielectric functions of the gain-plasmon system. Thus, it implies that fascinating optical properties and potential applications are expected since optical loss can be reduced and controlled, whereas super-absorber behavior can be achieved in close spectral regions.

Mesoporous silica capsules

A broadband plasmonic response strongly coupled with a gain medium located right at the heart of hierarchically complex plasmonic mesocapsules has been described. Colloid chemistry proved to be an unparalleled method to devise a perfect morphological definition of the capsules having gold nanoparticles engrafted on the inner walls, leading to a remarkable plasmons hybridization effect. This artificial supra-metamolecular organization showed striking opto-plasmonic features. In particular, gold nanoparticles surface plasmon states overcame a hybridization process resulting in a broad plasmon band acting as a whole acceptor for the non-radiative excitation energy channel of the chromophores. Not unexpectedly, both measurements and theory confirm a remarkable process of optical loss mitigation. This work shows the first experimental evidence of optical loss mitigation in a template embedding plasmonic nanoparticles, involving a large portion of the visible spectrum materials.

Macroscaled nanocomposite polymeric films

Nanocomposite polymer films were fabricated by simultaneous dispersion of QDs and Au-NPs by properly acting on the QDs surface chemistry. The presence of strong coupling mechanism between excitons and plasmonic NPs, dispersed in PDMS template were confirmed and it was demonstrated how this coupling mechanism strongly modifies the optical response of both the subunits in the system. QDs enhance their abosrption cross section, experiencing strong near plasmonic field, while non radiative energy

transfer processes from QDs to plasmonic NPs mitagates the absoptive losses and enables the entire system to be more transparent. In addition, the necessity of suitable amount of gain in close proximity of gold NPs was experimentally proved in order to achieve the desired coupling and RET processes between excitons and plasmons in bulk matrix. Absorption enhancement of QDs embedded in low loss plasmonic materials can find applications in many emerging fields, as biosensing and plasmonic solar cells. Furthermore, gain induced transparency in bulk systems show promising paths towards the realization of loss compensated plasmonic devices

Thue morse patterned plasmonic nanocavitie and Multilayered Ag/ITO HMM

Thue morse patterned plasmonic nanocavities and multilayered Ag/ITO HMM have been investigated in order to understand the intrinsic behavior before incorporation of gain. Thus, thue morse patterned plasmonic nanocavities with different diameters have been investigated. Subwavelength nanocavities show enhanced transmission, which was confirmed by confocal analysis and near-field images. Plasmon hybridization in surface plasmons, propagating at various metal-dielectric interfaces allows the different localization of light, enabling cavity modes which are polarization dependent and can be modified using an anlayser in the path of detected signal before PMT.

Furthermore, Ag/ITO multilayered structure as simultaneous type I/type HMM has been experimentally realized showing an incredibly high anisotropy, which leads towards an inversion point of coexisting anisotropies at a specified wavelength in the visible range. We will continue to functionalize gain in such particular structures to fabricate low loss plasmonic devices and to realize several unprecedented applications at optical wavelengths as future work.

Bibliography

[1] Audrey Moores and Frederic Goettmann. The plasmon band in noble metal nanoparticles: an introduction to theory and applications. *New J. Chem.*, 30: 1121–1132, 2006.

[2] Ian Freestone, Nigel Meeks, Margaret Sax, and Catherine Higgitt. The lycurgus cup a roman nanotechnology. *Gold Bulletin*, 40(4):270–277, 2007. ISSN 0017-1557.

[3] Nikolaos Vasilantonakis, Mazhar E. Nasir, Wayne Dickson, Gregory A. Wurtz, and Anatoly V. Zayats. Bulk plasmon-polaritons in hyperbolic nanorod metamaterial waveguides. *Laser & Photonics Reviews*, 9(3):345–353, 2015. ISSN 1863-8899.

[4] Jeffrey N. Anker, W. Paige Hall, Olga Lyandres, Nilam C. Shah, Jing Zhao, and Richard P. Van Duyne. Biosensing with plasmonic nanosensors. *Nat Mater*, 7 (6):442–453, June 2008. ISSN 1476-1122.

[5] W. Cai, U. K. Chettiar, A. V. Kildishev, and V. M. Shalaev. Optical Cloaking with Metamaterials. *Nature Photon.*, 1:224–227, 2008.

[6] Harry A Atwater. The promise of plasmonics. *Scientific American*, 296(4):56–62, 2007.

[7] W. Cai and V. Shalaev. *Optical Metamaterials: Fundamentals and Applications*. Springer, 2009. ISBN 9781441911513.

[8] P. Drude. Zur elektronentheorie der metalle. *Annalen der Physik*, 306(3):566–613, 1900. ISSN 1521-3889.

[9] N.W. Ashcroft and N.D. Mermin. *Solid State Physics*. Saunders College, Philadelphia, 1976.

[10] P.B. Johnson and R.W. Christy. Optical Constants of the Noble Metals. *Phys. Rev. B*, 6:4370–4379, 1972.

[11] C. Kittel. *Introduction to solid state physics*. Wiley, 1976. ISBN 9780471490241.

[12] Q. Zhang, J. J. Xu, Y. Liu, and H. Y. Chen. In-situ synthesis of poly(dimethylsiloxane)-gold nanoparticles composite films and its application in microfluidic systems. *Lab. on a Chip.*, 8:352, 2008.

[13] Prashant K Jain, Kyeong Seok Lee, Ivan H El-Sayed, and Mostafa A El-Sayed. Calculated absorption and scattering properties of gold nanoparticles of different size, shape, and composition: applications in biological imaging and biomedicine. *The Journal of Physical Chemistry B*, 110(14):7238–7248, 2006.

[14] Craig F. Bohren and D.R. Huffman. *Absorption and scattering of light by small particles*. Wiley science paperback series. Wiley, 1983. ISBN 9780471293408.

[15] Gustav Mie. Beiträge zur optik trüber medien, speziell kolloidaler metallósungen. *Annalen der Physik*, 330(3):377–445, 1908. ISSN 1521-3889.

[16] Max Born and Emil Wolf. *Principles of optics: electromagnetic theory of propagation, interference and diffraction of light*. Cambridge university press, 1999.

[17] J. D. Jackson and Ronald F. Fox. Classical electrodynamics, 3rd ed. *American Journal of Physics*, 67(9):841–842, 1999.

[18] N. M. Lawandy. Localized Surface Plasmon Singularities in Amplifying Media. *Appl. Phys. Lett.*, 85:5040–5042, 2004.

[19] M A Garcia. Surface plasmons in metallic nanoparticles: fundamentals and applications. *Journal of Physics D: Applied Physics*, 44(28):283001, 2011.

[20] U. Kreibig, B. Schmitz, and H. D. Breuer. Separation of plasmon-polariton modes of small metal particles. *Phys. Rev. B*, 36:5027–5030, Sep 1987.

[21] Min Hu, Jingyi Chen, Zhi-Yuan Li, Leslie Au, Gregory V. Hartland, Xingde Li, Manuel Marquez, and Younan Xia. Gold nanostructures: engineering their plasmonic properties for biomedical applications. *Chem. Soc. Rev.*, 35:1084–1094, 2006.

[22] Cecilia Noguez*. Surface plasmons on metal nanoparticles:the influence of shape and physical environment. *The Journal of Physical Chemistry C*, 111(10):3806–3819, 2007.

[23] Sylvia Underwood and Paul Mulvaney. Effect of the solution refractive index on the color of gold colloids. *Langmuir*, 10(10):3427–3430, 1994.

[24] R.W. Wood. On a remarkable case of uneven distribution of light in a diffraction grating spectrum. *Philosophical Magazine Series 6*, 4(21):396–402, 1902.

[25] Junxi Zhang, Lide Zhang, and Wei Xu. Surface plasmon polaritons: physics and applications. *Journal of Physics D: Applied Physics*, 45(11):113001, 2012.

[26] W. L. Barnes, A. Dereux, and T. W. Ebbesen. Surface Plasmon Subwavelength Optics. *Nature*, 424:824–830, 2003.

[27] S.A. Maier. *Plasmonics: Fundamentals and Applications: Fundamentals and Applications*. Springer, 2007. ISBN 9780387378251.

[28] C. Genet and T. W. Ebbesen. Light in tiny holes. *Nature*, 445(7123):39–46, January 2007. ISSN 0028-0836.

[29] K. F. Riley, M. P. Hobson, and S. J. Bence. *Mathematical Methods for Physics and Engineering*. Cambridge University Press, second edition, 2002. ISBN 9781139164979. Cambridge Books Online.

[30] Vladimir M. Shalaev. Optical negative-index metamaterials. *Nat Photon*, 1(1): 41–48, January 2007. ISSN 1749-4885.

[31] Huikan Liu and Kevin J. Webb. Resonance cones in cylindrically anisotropic metamaterials: a green's function analysis. *Opt. Lett.*, 36(3):379–381, Feb 2011.

[32] V. G. Veselago. THE ELECTRODYNAMICS OF SUBSTANCES WITH SIMULTANEOUSLY NEGATIVE VALUES OF Eps AND Mu. *Sov. Phys. Usp.*, 10:509, 1968.

[33] J. B. Pendry. Negative Refraction Makes a Perfect Lens. *Phys. Rev. Lett.*, 85: 3966–3969, 2000.

[34] J. B. Pendry, A. J. Holden, W. J. Stewart, and I. Youngs. Extremely low frequency plasmons in metallic mesostructures. *Phys. Rev. Lett.*, 76:4773–4776, Jun 1996. doi: 10.1103/PhysRevLett.76.4773.

[35] D. R. Smith, Willie J. Padilla, D. C. Vier, S. C. Nemat-Nasser, and S. Schultz. Composite medium with simultaneously negative permeability and permittivity. *Phys. Rev. Lett.*, 84:4184–4187, May 2000.

[36] R. A. Shelby, D. R. Smith, and S. Schultz. Experimental verification of a negative index of refraction. *Science*, 292(5514):77–79, 2001.

[37] Shuang Zhang, Wenjun Fan, N. C. Panoiu, K. J. Malloy, R. M. Osgood, and S. R. J. Brueck. Experimental demonstration of near-infrared negative-index metamaterials. *Phys. Rev. Lett.*, 95:137404, Sep 2005.

[38] MCK Wiltshire, JB Pendry, IR Young, DJ Larkman, DJ Gilderdale, and JV Hajnal. Microstructured magnetic materials for rf flux guides in magnetic resonance imaging. *SCIENCE*, 291:849–851, 2001.

[39] Vladimir M. Shalaev, Wenshan Cai, Uday K. Chettiar, Hsiao-Kuan Yuan, Andrey K. Sarychev, Vladimir P. Drachev, and Alexander V. Kildishev. Negative index of refraction in optical metamaterials. *Opt. Lett.*, 30(24):3356–3358, Dec 2005.

[40] Gunnar Dolling, Christian Enkrich, Martin Wegener, Costas M. Soukoulis, and Stefan Linden. Low-loss negative-index metamaterial at telecommunication wavelengths. *Opt. Lett.*, 31(12):1800–1802, Jun 2006.

[41] Viktor A. Podolskiy and Evgenii E. Narimanov. Near-sighted superlens. *Opt. Lett.*, 30(1):75–77, Jan 2005.

[42] Vladimir P. Drachev, Uday K. Chettiar, Alexander V. Kildishev, Hsiao-Kuan Yuan, Wenshan Cai, and Vladimir M. Shalaev. The ag dielectric function in plasmonic metamaterials. *Opt. Express*, 16(2):1186–1195, Jan 2008.

[43] Shumin Xiao, Vladimir P. Drachev, Alexander V. Kildishev, Xingjie Ni, Uday K. Chettiar, Hsiao-Kuan Yuan, and Vladimir M. Shalaev. Loss-free and active optical negative-index metamaterials. *Nature*, 466(7307):735–738, August 2010. ISSN 0028-0836.

[44] A.D. Boardman, V.V. Grimalsky, Y.S. Kivshar, S.V. Koshevaya, M. Lapine, N.M. Litchinitser, V.N. Malnev, M. Noginov, Y.G. Rapoport, and V.M. Shalaev. Active and tunable metamaterials. *Laser & Photonics Reviews*, 5(2):287–307, 2011. ISSN 1863-8899.

[45] S. Anantha Ramakrishna and J. B. Pendry. Removal of absorption and increase in resolution in a near-field lens via optical gain. *Phys. Rev. B*, 67:201101, May 2003.

[46] Alexandra Boltasseva and Vladimir M. Shalaev. Fabrication of optical negative-index metamaterials: Recent advances and outlook. *Metamaterials*, 2(1):1 – 17, 2008. ISSN 1873-1988.

[47] Oleg G. Tovmachenko, Christina Graf, Dave J. van den Heuvel, Alfons van Blaaderen, and Hans C. Gerritsen. Fluorescence enhancement by metal-core/silica-shell nanoparticles. *Adv. Mat.*, 18:91–95, 2006.

[48] H. Wang, D. W. Brandl, P. Nordlander, and N. J. Halas. Plasmonic nanostructures: Artificial molecules. *Acc. Chem. Res.*, 40:53–62, 2007.

[49] Fania C. Geiger, Fabian J. Eber, Sabine Eiben, Anna Mueller, Holger Jeske, Joachim P. Spatz, and Christina Wege. Tmv nanorods with programmed longitudinal domains of differently addressable coat proteins. *Nanoscale*, 5:3808–3816, 2013.

[50] K. Yong, Y. Sahoo, M. T. Swihart, and P. N. Prasad. Synthesis and plasmonic properties of silver and gold nanoshells on polystyrene cores of different size and of gold-silver core-shell nanostructures. *Colloids and Surfaces A: Physicochemical and Engineering Aspects*, 290:89–105, 2006.

[51] Xiaopeng Zhao. Bottom-up fabrication methods of optical metamaterials. *J. Mater. Chem.*, 22:9439–9449, 2012.

[52] C. R. Simovski and S. A. Tretyakov. Model of isotropic resonant magnetism in the visible range based on core-shell clusters. *Phys. Rev. B*, 79:045111, Jan 2009. doi: 10.1103/PhysRevB.79.045111.

[53] A. Alù, A. Salandrino, and N. Engheta. Negative effective permeability and left-handed materials at optical frequencies. *Opt. Express*, 14(4):1557–1567, Feb 2006.

[54] L.D. LANDAU and E.M. LIFSHITZ. {CHAPTER} v - {FERROMAGNETISM} {AND} {ANTIFERROMAGNETISM}. In L.D. LANDAU and E.M. LIFSHITZ, editors, *Electrodynamics of Continuous Media (Second Edition Revised and Enlarged)*, volume 8 of *Course of Theoretical Physics*, pages 130 – 179. Pergamon, Amsterdam, second edition revised and enlarged edition, 1984. ISBN 978-0-08-030275-1.

[55] V. M. Agranovich, Y. R. Shen, R. H. Baughman, and A. A. Zakhidov. Linear and nonlinear wave propagation in negative refraction metamaterials. *Phys. Rev. B*, 69:165112, Apr 2004.

[56] Prashant Shekhar, Jonathan Atkinson, and Zubin Jacob. Hyperbolic metamaterials: fundamentals and applications. *Nano Convergence*, 1(1):14, 2014. doi: 10.1186/s40580-014-0014-6.

[57] Alexander Poddubny, Ivan Iorsh, Pavel Belov, and Yuri Kivshar. Hyperbolic metamaterials. *Nat Photon*, 7(12):948–957, December 2013. ISSN 1749-4885.

[58] Dylan Lu and Zhaowei Liu. Hyperlenses and metalenses for far-field superresolution imaging. *Nat Commun*, 3:1205–, November 2012.

[59] Yu Guo and Zubin Jacob. Thermal hyperbolic metamaterials. *Opt. Express*, 21 (12):15014–15019, Jun 2013.

[60] Thomas Taubner, Dmitriy Korobkin, Yaroslav Urzhumov, Gennady Shvets, and Rainer Hillenbrand. Near-field microscopy through a sic superlens. *Science*, 313 (5793):1595–1595, September 2006.

[61] Anthony J. Hoffman, Leonid Alekseyev, Scott S. Howard, Kale J. Franz, Dan Wasserman, Viktor A. Podolskiy, Evgenii E. Narimanov, Deborah L. Sivco, and Claire Gmachl. Negative refraction in semiconductor metamaterials. *Nat Mater*, 6(12):946–950, December 2007. ISSN 1476-1122.

[62] Justin Elser, Viktor A Podolskiy, Ildar Salakhutdinov, and Ivan Avrutsky. Nonlocal effects in effective-medium response of nanolayered metamaterials. *Applied physics letters*, 90(19):191109, 2007.

[63] Joseph R. Lakowicz. *Principles of Fluorescence Spectroscopy*. Kluwer Academic/Plenum Publishers, second edition, 1999.

[64] Danuta Frackowiak. The jablonski diagram. *Journal of Photochemistry and Photobiology B: Biology*, 2(3):399 –, 1988. ISSN 1011-1344.

[65] G. F. Lothian. Beers law and its use in analysis. a review. *Analyst*, 88:678–685, 1963.

[66] SeungJae Yi and KyungChun Kim. Phosphorescence-based multiphysics visualization: a review. *Journal of Visualization*, 17(4):253–273, 2014. ISSN 1343-8875.

[67] Markus Sauer, Johan Hofkens, and Jörg Enderlein. *Basic Principles of Fluorescence Spectroscopy*, pages 1–30. Wiley-VCH Verlag GmbH & Co. KGaA, 2011. ISBN 9783527633500.

[68] J. R. Lakowicz. *Principles of Fluorescence Spectroscopy, 3rd Ed.* Springer, New York, p. 444, 2006.

[69] Ute Resch-Genger, Markus Grabolle, Sara Cavaliere-Jaricot, Roland Nitschke, and Thomas Nann. Quantum dots versus organic dyes as fluorescent labels. *Nat Meth*, 5(9):763–775, September 2008. ISSN 1548-7091.

[70] Mine G. Ucak-Astarlioglu Benjamin M. Hutchins, Thomas T. Morgan and Mary Elizabeth Williams. Optical properties of fluorescent mixtures: Comparing quantum dots to organic dyes. *Journal of Chemical Education*, 84(8):1301, 2007.

[71] T. Förster. Intermolecular Energy Migration and Fluorescence. *Ann. Phys.*, 2: 55–75, 1948.

[72] L Stryer. Fluorescence energy transfer as a spectroscopic ruler. *Annual Review of Biochemistry*, 47(1):819–846, 1978. PMID: 354506.

[73] Lin Qiu L FAU Qiu, Yanhua Bi Y FAU Bi, Cheli Wang C FAU Wang, Jingyan Li J FAU Li, Peilin Guo P FAU Guo, Jinchen Li J FAU Li, Weijiang He W FAU He, Jianhao Wang J FAU Wang, and Pengju Jiang P FAU Jiang. Protein a detection based on quantum dots-antibody bioprobe using fluorescence coupled capillary electrophoresis.

[74] J. R. Lakowicz. Radiative Decay Engineering: Biophysical and Biomedical Applications. *Anal. Biochem.*, 298:1–24, 2001.

[75] J. Gersten and A. Nitzan. Spectroscopic Properties of Molecules Interacting with Small Dielectric Particles. *J. Chem. Phys.*, 75:1139–1152, 1981.

[76] P. C. Das and A. Puri. Energy Flow and Fluorescence near a Small Metal Particle. *Phys. Rev. B*, 65(65):155416, 2002.

[77] E. Dulkeith, A. C. Morteani, T. Niedereichholz, T. A. Klar, J. Feldmann, S. A. Levi, F. C. J. M. van Veggel, D. N. Reinhoudt, M. Moller, and D. I. Gittins. Fluorescence Quenching of Dye Molecules near Gold Nanoparticles: Radiative and Nonradiative Effects. *Phys. Rev. Lett.*, 89:203002, 2002.

[78] D. A. Weitz, S. Garoff, J. I. Gersten, and A. Nitzan. The Enhancement of Raman Scattering, Resonance Raman Scattering and Fluorescence from Molecules Adsorbed on a Rough Silver Surface. *J. Chem. Phys.*, 78:5324–5338, 1983.

[79] J. Seelig, K. Leslie, A. Renn, S. Kahn, V. Jacobsen, M. van de Corputand C. Wyman A, , and V. Sandoghdar. Nanoparticle-induced fluorescence lifetime modification as nanoscopic ruler: Demonstration at the single molecule level. *Nano Letters*, 7(3):685–689, 2007.

[80] S. Bhowmick, S. Saini, V. B. Shenoy, and B. Bagchi. Resonance Energy Transfer from a Fluorescent Dye to a Metal Nanoparticle. *J. Chem. Phys.*, 125:181102/1–6, 2006.

[81] T. Soller, M. Ringler, M. Wunderlich, * T. A. Klar, , J. Feldmann, H.-P. Josel, Y. Markert, A. Nichtl, , and K. Kürzinger. Radiative and nonradiative rates of phosphors attached to gold nanoparticles. *Nano Letters*, 7(7):1941–1946, 2007.

[82] Sangeeta Saini, Goundla Srinivas, and Biman Bagchi. Distance and orientation dependence of excitation energy transfer: From molecular systems to metal nanoparticles. *The Journal of Physical Chemistry B*, 113(7):1817–1832, 2009.

[83] P. Anger, P. Bharadwaj, and L. Novotny. Enhancement and Quenching of Single-Molecule Fluorescence. *Phys. Rev. Lett.*, 96:113002, 2006.

[84] S. Kuhn, U. Hakanson, L. Rogobete, and V. Sandoghdar. Enhancement of Single-Molecule Fluorescence Using a Gold Nanoparticle as an Optical Nanoantenna. *Phys. Rev. Lett.*, 97:017402, 2006.

[85] Salvatore Campione and Filippo Capolino. Composite material made of plasmonic nanoshells with quantum dot cores: loss-compensation and ε-near-zero physical properties. *Nanotechnology*, 23(23):235703, 2012.

[86] Costas M. Soukoulis and Martin Wegener. Optical metamaterials more bulky and less lossy. *Science*, 330(6011):1633–1634, December 2010.

[87] M. A. Noginov, G. Zhu, M. Bahoura, J. Adegoke, C. E. Small, B. A. Ritzo, V. P. Drachev, and V. M. Shalaev. Enhancement of Surface Plasmons in an Ag Aggregate by Optical Gain in a Dielectric Medium. *Opt. Lett.*, 31:3022–3024, 2006.

[88] B. Peng, Q. Zhang, X. Liu, Y. Ji, H.V. Demir, C. H. A. Huan, T. C. Sum, and Q. Xiong. Fluorophore-Doped Core-Multishell Spherical Plasmonic Nanocavities: Resonant Energy Transfer toward a Loss Compensation. *ACS Nano*, 6 (7): 6250–6259, 2012.

[89] M. A. Noginov, G. Zhu, A. M. Belgrave, R. Bakker, V. M. Shalaev, E. E. Narimanov, S. Stout, E. Herz, T. Suteewong, and U. Wiesner. Demonstration of a Spaser-Based Nanolaser. *Nature*, 460:1110–1113, 2009.

[90] A. De Luca, M. P. Grzelczak, I. Pastoriza-Santos, L. M. Liz-Marzán, M. La Deda, M. Striccoli, and G. Strangi. Dispersed and Encapsulated Gain Medium in Plasmonic Nanoparticles: a Multipronged Approach to Mitigate Optical Losses. *ACSNano*, 5:5823–5829, 2011.

[91] JinZ. Zhang and Cecilia Noguez. Plasmonic optical properties and applications of metal nanostructures. *Plasmonics*, 3(4):127–150, 2008. ISSN 1557-1955. doi: 10.1007/s11468-008-9066-y.

[92] Xiang Zhang and Zhaowei Liu. Superlenses to overcome the diffraction limit. *Nat Mater*, 7(6):435–441, June 2008. ISSN 1476-1122.

[93] M. A. Noginov, V. A. Podolskiy, G. Zhu, M. Mayy, M. Bahoura, J. A. Adegoke, B. A. Ritzo, and K. Reynolds. Compensation of loss in propagating surface plasmon polariton by gain in adjacent dielectric medium. *Opt. Express*, 16(2): 1385–1392, Jan 2008.

[94] A. De Luca, R. Dhama, A. R. Rashed, C. Coutant, S. Ravaine, P. Barois, M. Infusino, and G. Strangi. Double strong exciton-plasmon coupling in gold nanoshells infiltrated with fluorophores. *Applied Physics Letters*, 104(10): 103103, 2014.

[95] G. Strangi, A. De Luca, S. Ravaine, M. Ferrie, and R. Bartolino. Gain induced optical transparency in metamaterials. *Appl. Phys. Lett.*, 98:251912, 2011.

[96] A. De Luca, M. Ferrie, S. Ravaine, M. La Deda, M. Infusino, A. Rahimi Rashed, A. Veltri, A. Aradian, N. Scaramuzza, and G. Strangi. Gain functionalized core???shell nanoparticles: the way to selectively compensate absorptive losses. *J. Mater. Chem.*, 22:8846–8852, 2012.

[97] P. Nordlander*, , C. Oubre, E. Prodan, K. Li, , and M. I. Stockman. Plasmon hybridization in nanoparticle dimers. *Nano Letters*, 4(5):899–903, 2004.

[98] Daniel W. Brandl, and Nikolay A. Mirin, and Peter Nordlander. Plasmon modes of nanosphere trimers and quadrumers. *The Journal of Physical Chemistry B*, 110(25):12302–12310, 2006. PMID: 16800552.

[99] C. S. Yun, A. Javier, T. Jennings, M. Fisher, S. Hira, S. Peterson, B. Hopkins, N. O. Reich, and G. F. Strouse. Nanometal Surface Energy Transfer in Optical Rulers, Breaking the FRET Barrier. *J. Am. Chem. Soc.*, 127:3115–3119, 2005.

[100] Kenneth R. Brown, Daniel G. Walter, , and Michael J. Natan*. Seeding of colloidal au nanoparticle solutions. 2. improved control of particle size and shape. *Chemistry of Materials*, 12(2):306–313, 2000.

[101] C. Graf and A. van Blaaderen. Metallodielectric Colloidal Core-Shell Particles for Photonic Applications. *Langmuir*, 18:524–534, 2002.

[102] Michael Giersig Luis M. Liz-Marzán, , and Paul Mulvaney. Synthesis of nanosized gold-silica core-shell particles. *Langmuir*, 12(18):4329–4335, 1996.

[103] N. M. Lawandy. Nano-particle Plasmonics in Active Media. *Proceedings of the SPIE*, 59240:59240G–1–13, 2005.

[104] Vitaliy N. Pustovit and Tigran V. Shahbazyan. Cooperative emission of light by an ensemble of dipoles near a metal nanoparticle: The plasmonic dicke effect. *Phys. Rev. Lett.*, 102:077401, Feb 2009.

[105] V.N. Pustovit and T.V. Shahbazyan. Resonance energy transfer near metal nanostructures mediated by surface plasmons. *Phys. Rev. B*, 83:085427 1–4, 2011.

[106] Renaud A. L. Vallée, Mélanie Ferrié, Hassan Saadaoui, and Serge Ravaine. Broadband spontaneous emission rate enhancement through the design of plasmonic nanoantennas. *Opt. Mater. Express*, 2(5):566–577, May 2012.

[107] Tim A. Erickson and James W. Tunnell. *Nanomaterials for the Life Sciences Vol. 3: Mixed Metal Nanomaterials. Chapter 1: "Gold Nanoshells in Biomedical Applications"*. WILEY-VCH Verlag GmbH & Co. KGaA, Weinheim, 2009.

[108] C. Wu, X. Liang, and H. Jiang. Metal nanoshells as a contrast agent in near - infrared diffuse optical tomography. *Optics Communications*, 253:214–21, 2005.

[109] C.A. Leatherdale, W.K. Woo, F.V. Mikulec, and M.G. Bawendi. On the absorption cross section of cdse nanocrystal quantum dots. *The Journal of Physical Chemistry B*, 106:7619–22, 2002.

[110] L.R. Hirsch, R.J. Stafford, J.A. Bankson, S.R. Sershen, B. Rivera, R.E. Price, J.D. Hazle, N.J. Halas, and J.L. West. Nanoshell - mediated near-infrared thermal therapy of tumors under magnetic resonance guidance. *Proceedings of the National Academy of Sciences of the United States of America*, 100:13549–54, 2003.

[111] J. Park, A. Estrada, K. Sharp, K. Sang, J.A. Schwartz, D.K. Smith, C. Coleman, J.D. Payne, B.A. Korgel, A.K. Dunn, and J.W. Tunnell. Two-photon-induced photoluminescence imaging of tumors using near - infrared excited gold nanoshells. *Optics Express*, 16:1590–9, 2008.

[112] J. Yguerabide and E.E. Yguerabide. Resonance light scattering particles as ultrasensitive labels for detection of analytes in a wide range of applications. *Journal of Cellular Biochemistry*, 84:71–81, 2001.

[113] C. Eggeling, J. Widengren, R. Rigler, and C.A.M. Seidel. Photobleaching of fl uorescent dyes under conditions used for single-molecule detection: evidence of two -step photolysis. *Analytical Chemistry*, 70:2651–9, 1998.

[114] J. Widengren and R. Rigler. Mechanisms of photobleaching investigated by fl uorescence correlation spectroscopy. *Bioimaging*, 4:149–157, 1996.

[115] Marie-Christine Daniel, , and Didier Astruc*. Gold nanoparticles: Assembly, supramolecular chemistry, quantum-size-related properties, and applications toward biology, catalysis, and nanotechnology. *Chemical Reviews*, 104(1):293–346, 2004. PMID: 14719978.

[116] R. D. Averitt, S. L. Westcott, and N. J. Halas. Linear Optical Properties of Gold Nanoshells. *J. Opt. Soc. Am. B*, 16:1824–1832, 1999.

[117] W.Y. Chien and T. Szkopek. Multiple- multipole simulation of optical nearfi elds in discrete metal nanosphere assemblies. *Optics Express*, 16:1820–35, 2008.

[118] S.J. Oldenburg, G.D. Hale, J.B. Jackson, and N.J. Halas. Light scattering from dipole and quadrupole nanoshell antennas. *Applied Physics Letters*, 75:1063, 1999.

[119] J.B. Jackson, S.L. Westcott, L.R. Hirsch, J.L. West, and N.J. Halas. Controlling the surface enhanced raman effect via the nanoshell geometry. *Applied Physics Letters*, 82:257, 2003.

[120] I. Avrutsky. Surface Plasmons at Nanoscale Relief Gratings between a Metal and a Dielectric Medium with Optical Gain. *Phys. Rev. B*, 70:155416, 2004.

[121] J. Seidel, S. Grafstrom, and L. Eng. Stimulated Emission of Surface Plasmons at the Interface between a Silver Film and an Optically Pumped Dye Solution. *Phys. Rev. Lett.*, 94:177401, 2005.

[122] Joshua A. Gordon and Richard W. Ziolkowski. CNP Optical Metamaterials. *Opt. Express*, 16:6692–6716, 2008.

[123] A. Fang, Th. Koschny, M. Wegener, and C. M. Soukoulis. Self-Consistent Calculation of Metamaterials with Gain. *Phys. Rev. B*, 79:241104, 2009.

[124] W. Stöber, A. Fink, and E. Bohn. Controlled growth of monodisperse silica spheres in the micron size range. *Journal of colloid and interface science*, 26: 62–69, 1968.

[125] S. Reculusa and S. Ravaine. Synthesis of colloidal crystals of controllable thickness through the langmuir-blodgett technique. *Chem. Mater.*, 15, 2003.

[126] D. G. Duff, A. Baiker, and P. P. Edwards. A new hydrosol of gold clusters. 1. formation and particle size variation. *Langmuir*, 9:2301–2309, 1993.

[127] S. L. Westscott, S. J. Oldenburg, T. R. Lee, and N. J Halas. Formation and adsorption of clusters of gold nanoparticles onto functionalized silica nanoparticle surfaces. *Langmuir*, 14:5396–5401, 1998.

[128] B.E. Brinson, J. B. Lassiter, C. S. Levin, R. Bardhan, and N. Mirin N. J. Halas. Nanoshells made easy: Improving au layer growth on nanoparticle surfaces. *Langmuir*, 24:14166–14171, 2008.

[129] N. Phonthammachai, J. C. Y. Kah, G. Jun, C. J. R. Sheppard, M. C. Olivo, S.G. Mhaisalkar, and T. J. White. Synthesis of contiguous silica-gold core-shell structures: Critical parameters and processes. *Langmuir*, 24:5109–5112, 2008.

[130] Ludivine Malassis, Pascal Massé, Mona Tréguer-Delapierre, Stephane Mornet, Patrick Weisbecker, Philippe Barois, Constantin R. Simovski, Vasyl G. Kravets, and Alexander N. Grigorenko. Topological darkness in self-assembled plasmonic metamaterials. *Advanced Materials*, 26(2):324–330, 2014. ISSN 1521-4095.

[131] Carmen Vázquez-Vázquez, Belén Vaz, Vincenzo Giannini, Moisés Pérez-Lorenzo, Ramon A. Alvarez-Puebla, and Miguel A. Correa-Duarte. Nanoreactors

for simultaneous remote thermal activation and optical monitoring of chemical reactions. *Journal of the American Chemical Society*, 135(37):13616–13619, 2013.

[132] M. I. Stockman. Spaser Action Loss Compensation and Stability in Plasmonic Systems with Gain. *Phys. Rev. Lett.*, 106:156802–1–4, 2011.

[133] O. Hess, J. B. Pendry, S. A. Maier, R. F. Oulton, J. M. Hamm, and K. L. Tsakmakidis. Active nanoplasmonic metamaterials. *Nat Mater*, 11(7):573–584, July 2012. ISSN 1476-1122.

[134] D. G. Shchukin, I. L. Radtchenko, and G. B. Sukhorukov. Micron-scale hollow polyelectrolyte capsules with nanosized magnetic fe3o4 inside. *Mater. Lett.*, 57: 1743–1747, 2003.

[135] M. Sanlés-Sobrido, W. Exner, L. Rodríguez - Lorenzo, B. Rodríguez - González, M. A. Correa - Du arte, R. A. Alvarez - Puebla, and L. Liz - Marzán. Design of SERS-Encoded, Submicron, Hollow Particles Through Confined Growth of Encapsulated Metal Nanoparticles . *J. Am. Chem. Soc.*, 131:2699–2705, 2009.

[136] C. Vázquez-Vázquez, V. Salgueiriño, M.A. Correa-Duarte, and M. Pérez-Lorenzo. *An. Quím.*, 108:1–6, 2012.

[137] Y. Deng, D. Qi, C. Deng, X. Zhang, and D. Zhao. Superparamagnetic High-Magnetization Microspheres with an Fe3O4@SiO2 Core and Perpendicularly Aligned Mesoporous SiO2 Shell for Removal of Microcystins. *J. Am. Chem. Soc.*, 130:28–29, 2008.

[138] Hui Wang, and Peter Nordlander Daniel W. Brandl, , and Naomi J. Halas. Plasmonic nanostructures:artificial molecules. *Accounts of Chemical Research*, 40 (1):53–62, 2007.

[139] Melissa Infusino, Antonio De Luca, Alessandro Veltri, Carmen Vázquez-Vázquez, Miguel A. Correa-Duarte, Rakesh Dhama, and Giuseppe Strangi. Loss-mitigated collective resonances in gain-assisted plasmonic mesocapsules. *ACS Photonics*, 1(4):371–376, 2014.

[140] S. A. Maier. Plasmonic field enhancement and SERS in the effective mode volume picture. *Optics Express*, 14:1957–1964, 2006.

[141] R. J. Thompson, G. Rempe, and H. J. Kimble. Observation of normal-mode splitting for an atom in an optical cavity. *Phys. Rev. Lett.*, 68:1132–1135, Feb 1992.

[142] T. Yoshie, A. Scherer, J. Hendrickson, G. Khitrova, H. M. Gibbs, G. Rupper, C. Ell, O. B. Shchekin, and D. G. Deppe. Vacuum rabi splitting with a single quantum dot in a photonic crystal nanocavity. *Nature*, 432(7014):200–203, November 2004. ISSN 0028-0836.

[143] Takao Aoki, Barak Dayan, E. Wilcut, W. P. Bowen, A. S. Parkins, T. J. Kippenberg, K. J. Vahala, and H. J. Kimble. Observation of strong coupling between one atom and a monolithic microresonator. *Nature*, 443(7112):671–674, October 2006. ISSN 0028-0836.

[144] Eyal Cohen-Hoshen, Garnett W. Bryant, Iddo Pinkas, Joseph Sperling, and Israel Bar-Joseph. Exciton???plasmon interactions in quantum dot???gold nanoparticle structures. *Nano Letters*, 12(8):4260–4264, 2012.

[145] Daniel Ratchford, Farbod Shafiei, Suenne Kim, Stephen K. Gray, and Xiaoqin Li. Manipulating coupling between a single semiconductor quantum dot and single gold nanoparticle. *Nano Letters*, 11(3):1049–1054, 2011.

[146] J. N. Farahani, D. W. Pohl, H.-J. Eisler, and B. Hecht. Single quantum dot coupled to a scanning optical antenna: A tunable superemitter. *Phys. Rev. Lett.*, 95: 017402, Jun 2005.

[147] A.C. Balazs, T. Emrick, and T.P. Russell. Nanoparticle polymer composites: where two small worlds meet. *Science*, 314:1107, 2006.

[148] Q. Wang and D. Seo. Preparation of photostable quantum dot-polystyrene microbeads through covalent organosilane coupling of CdSe@Zns quantum dots. *J. Mater. Sci.*, 44:816–820, 2009.

[149] P. Andrew, S. C. Kitson, and W. L. Barnes. Surface-plasmon energy gaps and photoabsorption. *Journal of Modern Optics*, 44(2):395–406, 1997. doi: 10.1080/09500349708241879.

[150] Alireza Rahimi Rashed, Antonio De Luca, Rakesh Dhama, Arash Hosseinzadeh, Melissa Infusino, Mohamed El Kabbash, Serge Ravaine, Roberto Bartolino, and Giuseppe Strangi. Battling absorptive losses by plasmon-exciton coupling in multimeric nanostructures. *RSC Adv.*, 5:53245–53254, 2015.

[151] H. Hiramatsu and F. E. Osterloh. A Simple Large-Scale Synthesis of Nearly Monodisperse Gold and Silver Nanoparticles with Adjustable Sizes and with Exchangeable Surfactants. *Chem. Mater.*, 16:2509–2511, 2004.

[152] A. De Luca, N. Depalo, E. Fanizza, M. Striccoli, M. L. Curri, M. Infusino, A. R. Rashed, M. La Deda, and G. Strangi. Plasmon mediated super-absorber flexible nanocomposite for metamaterials. *Nanoscale*, 5:6097, 2013.

[153] L. Qu and X. Peng. Control of Photoluminescence Properties of CdSe Nanocrystals in Growth. *J. Am. Chem. Soc.*, 124:2049, 2002.

[154] S. Shojaei-Zadeh, J. F. Morris, A. Couzis, and C. Maldarelli. Highly Crosslinked Poly(Dimethylsiloxane) Microbeads with Uniformly Dispersed Quantum Dot Nanocrystals. *J. Colloid Interface Sci.*, 363:25, 2011.

[155] J. Weaver, R. Zakeri, S. Aouadi, and P. Kohli. Synthesis and characterization of quantum dot-polymer composites. *J. Mater. Chem.*, 19:3198–3206, 2009.

[156] D. I. Uhlenhaut, P. Smith, and W. Caseri. Color Switching in Gold-Polysiloxane Elastomeric Nanocomposites. *Adv. Mater.*, 18:1653, 2006.

[157] H. N. S. Krishnamoorthy, Z. Jacob, E. Narimanov, I. Kretzschmar, and V. M. Menon. Topological transitions in metamaterials. *Science*, 336:205–209, 2012.

[158] K. V. Sreekanth, A. De Luca, and G. Strangi. Experimental demonstration of surface and bulk plasmon polaritons in hypergratings. *Scientific Reports*, 3:3291, 2013.

[159] L.O. Palsson and A. P. Monkman. Measurements of Solid-State Photoluminescence Quantum Yields of Films Using a Fluorimeter. *Adv. Mater.*, 14:757, 2002.

[160] Tomasz J. Antosiewicz, S. Peter Apell, and Timur Shegai. Plasmon-exciton interactions in a core-shell geometry: From enhanced absorption to strong coupling. *ACS Photonics*, 1(5):454–463, 2014.

[161] Dmitri K. Gramotnev and Sergey I. Bozhevolnyi. Plasmonics beyond the diffraction limit. *Nat Photon*, 4(2):83–91, February 2010. ISSN 1749-4885.

[162] T. W. Ebbesen, H. J. Lezec, H. F. Ghaemi, T. Thio, and P. A. Wolff. Extraordinary optical transmission through sub-wavelength hole arrays. *Nature*, 391(6668): 667–669, February 1998. ISSN 0028-0836.

[163] Takumi Sannomiya, Olivier Scholder, Konstantins Jefimovs, Christian Hafner, and Andreas B. Dahlin. Investigation of plasmon resonances in metal films with nanohole arrays for biosensing applications. *Small*, 7(12):1653–1663, 2011. ISSN 1613-6829.

[164] Venu Gopal Achanta. Plasmonic quasicrystals. *Progress in Quantum Electronics*, 39:1 – 23, 2015. ISSN 0079-6727.

[165] Ido Dolev, Michael Volodarsky, Gil Porat, and Ady Arie. Multiple coupling of surface plasmons in quasiperiodic gratings. *Opt. Lett.*, 36(9):1584–1586, May 2011.

[166] Markus Schwind, Bengt Kasemo, and Igor Zorić. Localized and propagating plasmons in metal films with nanoholes. *Nano Letters*, 13(4):1743–1750, 2013. PMID: 23484456.

[167] H. F. Ghaemi, Tineke Thio, D. E. Grupp, T. W. Ebbesen, and H. J. Lezec. Surface plasmons enhance optical transmission through subwavelength holes. *Phys. Rev. B*, 58:6779–6782, Sep 1998.

[168] Hanwei Gao, Joel Henzie, , and Teri W. Odom*. Direct evidence for surface plasmon-mediated enhanced light transmission through metallic nanohole arrays. *Nano Letters*, 6(9):2104–2108, 2006. PMID: 16968034.

[169] L. Martín-Moreno, F. J. García-Vidal, H. J. Lezec, K. M. Pellerin, T. Thio, J. B. Pendry, and T. W. Ebbesen. Theory of extraordinary optical transmission through subwavelength hole arrays. *Phys. Rev. Lett.*, 86:1114–1117, Feb 2001.

[170] Qian-jin Wang, Jia-qi Li, Cheng-ping Huang, Chao Zhang, and Yong-yuan Zhu. Enhanced optical transmission through metal films with rotation-symmetrical hole arrays. *Applied Physics Letters*, 87(9):091105, 2005.

[171] Robert C. Dunn. Near-field scanning optical microscopy. *Chemical Reviews*, 99 (10):2891–2928, 1999. PMID: 11749505.

[172] D. W. Pohl, W. Denk, and M. Lanz. Optical stethoscopy: Image recording with resolution. *Applied Physics Letters*, 44(7):651–653, 1984.

[173] Tae-Ho Park, Nikolay Mirin, J. Britt Lassiter, Colleen L. Nehl, Naomi J. Halas, and Peter Nordlander. Optical properties of a nanosized hole in a thin metallic film. *ACS Nano*, 2(1):25–32, 2008.

[174] P. D. Lacharmoise, N. G. Tognalli, A. R. Goñi, M. I. Alonso, A. Fainstein, R. M. Cole, J. J. Baumberg, J. Garcia de Abajo, and P. N. Bartlett. Imaging optical near fields at metallic nanoscale voids. *Phys. Rev. B*, 78:125410, Sep 2008.

[175] Jared K. Day, Nicolas Large, Peter Nordlander, and Naomi J. Halas. Standing wave plasmon modes interact in an antenna-coupled nanowire. *Nano Letters*, 15 (2):1324–1330, 2015.